UNIVERSITÉ DE STRASBOURG

N° ordre UDS 727

N° ordre IPHC 2010-016

Thèse

Thèse .

Présentée par

Jean Claude THIRY

Pour obtenir le grade de

Docteur de l'Université de Strasbourg

Spécialité

Physique Nucléaire

Mesure de sections efficaces des réactions (n,xnγ) d'intérêt pour les réacteurs de IV^{e} génération

Institut Pluridisciplinaire
Hubert Curien
Département de Recherches Subatomiques

UMR 7178

IPHC
Institut Pluridisciplinaire Hubert CURIEN
STRASBOURG

UNIVERSITÉ DE STRASBOURG

UNIVERSITE DE STRASBOURG

THESE DE DOCTORAT

Présentée par :

Jean Claude Thiry

Titre :

Mesure de sections efficaces des réactions (n,xnγ) d'intérêt pour les réacteurs de IVe génération

Discipline :

Physique nucléaire

Directeur de Thèse :	Philippe Dessagne - DR
Unité de Recherche :	Institut Pluridisciplinaire Hubert Curien (IPHC) - UMR 7178

Soutenue publiquement le 30 septembre 2010 devant la Commission d'examen :

Ph. DESSAGNE	Directeur de thèse
B. HAAS	Rapporteur externe
F. GUNSING	Rapporteur externe
A. NOURREDDINE	Examinateur interne
A. PLOMPEN	Examinateur externe
J.C. STECKMEYER	Examinateur externe

Résumé

Le développement de la IV^e génération de réacteurs nucléaires demande une bonne connaissance de certaines réactions nucléaires. En effet, ces installations fonctionneront dans le domaine des neutrons de haute énergie pour lequel de nombreuses interactions non ou mal quantifiées à ce jour ont lieu. L'étude de ces nouveaux types de réacteurs requiert, entre autres, la connaissance précise des réactions (n,xn). En effet, elles participent au ralentissement et à la multiplication de neutrons, mais elles contribuent également à la production d'isotopes radioactifs au sein du réacteur.

Dans cette thèse un dispositif expérimental a été mis au point afin d'obtenir une précision maximale sur les sections efficaces de réactions (n,xnγ) en utilisant la technique de détection de rayonnements γ prompts. Des mesures ont ainsi pu être réalisées sur les isotopes ^{232}Th et ^{235}U.

Contexte général

L'augmentation de la population mondiale d'un côté et le développement des pays du tiers-monde d'un autre côté se traduisent par une demande croissante d'énergie. Or, dans la production primaire au niveau mondial, 80% de l'énergie provient de la combustion de ressources fossiles. L'épuisement de ces ressources ainsi que la volonté de diminuer leurs usages afin de réduire l'émission de gaz à effet de serre impliquent le développement d'autres sources d'énergie, comme le nucléaire et les énergies renouvelables. Afin de faire face à cet énorme défi d'approvisionnement en énergie de notre planète pour les générations futures, ces deux moyens de production doivent évoluer.

Cependant l'énergie nucléaire, de son côté aussi, doit faire face à certains défis. Le cycle électronucléaire actuel repose sur la combustion de ^{235}U, qui ne constitue que 0,7% de l'Uranium naturel. En admettant une consommation constante voire croissante, on prévoit un épuisement de ^{235}U d'ici une centaine d'années. La constante amélioration de la sûreté de la production d'énergie nucléaire et la gestion de ses déchets sont indispensables afin d'en garantir l'acceptation par le public.

À cet effet, le forum international Génération IV vise à développer des nouvelles techniques capables de regénerer du combustible fissile à partir de la matière fertile. Certains de ces projets actuellement étudiés considèrent également l'introduction de déchets radioactifs dans les coeurs des réacteurs afin de les incinérer. Cette incinération et la régénération étant optimales dans le domaine des neutrons rapides, une recherche conséquente devra accompagner le développement de ces nouvelles filières de réacteurs et notamment l'étude

des réactions induites par des neutrons de haute énergie (jusqu'à 20 MeV, voire au delà pour les réacteurs souscritiques pilotés par accélérateur).

Un intérêt particulier est prêté aux réactions (n,xn) puisqu'elles participent au ralentissement et à la multiplication de neutrons, et qu'elles contribuent également à la production d'isotopes radioactifs. Afin d'optimiser le fonctionnement de ces nouveaux réacteurs, les sections efficaces de ces réactions, utilisées dans les bases de données nucléaires, doivent être connues de façon précise. Dans ce contexte, le but de ce travail était de mettre au point un dispositif de mesure capable d'atteindre une précision de l'ordre de 5%.

Dispositif expérimental

Les mesures sont effectuées à l'IRMM[1] à Geel près d'un faisceau de neutrons généré par GELINA[2], un accélérateur linéaire d'électrons. Les électrons d'une énergie de 70 à 140 MeV bombardent une cible rotative d'Uranium. A l'intérieur de cette cible les électrons produisent du rayonnement γ par *Bremsstrahlung* qui, à son tour, interagit avec l'Uranium pour produire des neutrons par réaction (γ,n) et (γ,f). Le faisceau de neutrons ainsi généré est un faisceau blanc (neutrons d'une énergie de quelques meV allant jusqu'à 20 MeV) qui peut être pulsé entre 40 et 800 Hz.

Les neutrons sortant de la partie accélérateur entrent sur les pistes de vol où ils sont différemment collimatés suivant la nature des mesures. Les dispositifs expérimentaux se trouvent sur des bases de vol se situant à des distances bien connues de l'endroit de la création des neutrons, ce qui permet la détermination de leurs énergies grâce à la technique de mesure du temps de vol (TOF).

La mesure des sections efficaces se fait selon la méthode de la spectroscopie γ prompte. Dans notre cas, un échantillon fortement enrichi en isotope d'intérêt est bombardé par des neutrons qui donnent lieu, entre autres, aux réactions (n,n'), (n,2n) et (n,3n). Ces dernières conduisent à la formation d'un noyau excité dont la désexcitation se fait instantanément par émission d'un rayonnement γ. Son énergie, caractéristique d'une transition entre deux états bien définis du noyau créé, permet d'identifier le type de réaction.

Afin d'observer les rayonnements γ provenant de l'échantillon, quatre détecteurs HPGe semi-planaires sont placés à des angles de 110° et 149° autour de la cible (cf. Fig. 1). L'amplitude des signaux, traduisant l'énergie du photon γ, ainsi que le temps de détection sont enregistrés par des cartes numériques TNT[3].

Une chambre à fission, placée avant la cible, permet la détermination du flux de neutrons incidents.

La forte radioactivité des échantillons et la volonté d'observer des rayonnements γ de faible énergie imposent des limites sur la taille de la cible. En effet, les rayonnements γ, caractéristiques des réactions (n,n') et (n,2n) sur ^{232}Th et ^{235}U de faible énergie (majoritairement inférieure à 250 keV), sont plus absorbés à l'intérieur de la cible que ceux

[1] Institute for Reference Materials and Measurements

[2] GEel LINear Accelerator

[3] Treatment for Numerical Tracking ou Treatment for NTof. Cartes d'acquisition développées par l'équipe de Patrice MEDINA à l'IPHC. Les cartes ont un taux d'échantillonage de 100 MHz, et une résolution de 14 bits.

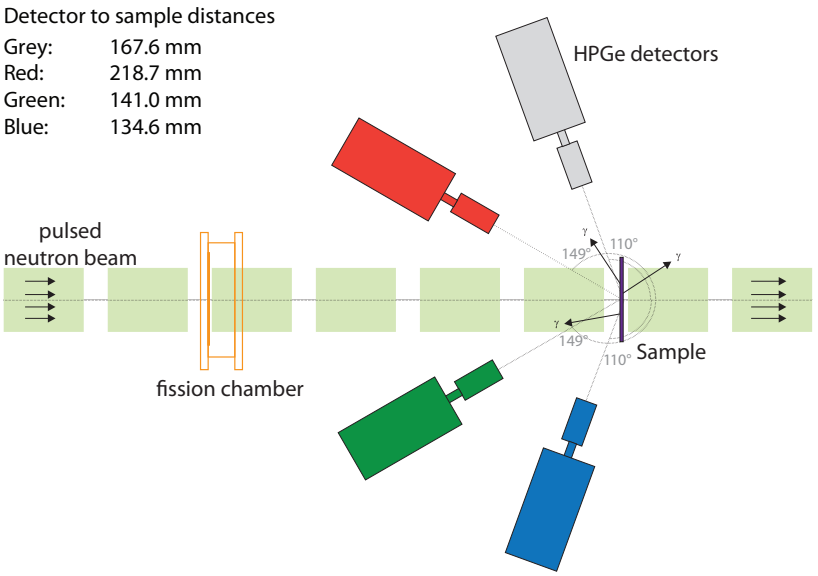

Figure 1: Schéma du dispositif expérimental.

d'une énergie plus élevée, on parle d'*autoabsorption*. Pour limiter ces effets, on est contraint d'utiliser une cible relativement mince. Une cible mince, donnant lieu à un taux de réaction plus faible, impose de son côté de se rapprocher de la source de neutrons afin de profiter d'un flux incident plus élevé. Le dispositif expérimental est ainsi placé dans une base de vol située à une distance de 30 m de la source de production des neutrons et le faisceau est pulsé à une fréquence de 800 Hz.

Les principales sources d'erreurs sur les mesures effectuées par ce dispositif proviennent de l'estimation des efficacités des détecteurs utilisés. Ces paramètres ont donc été analysés soigneusement afin de diminuer les incertitudes au maximum.

Efficacité de la chambre à fission

Un paramètre ayant un grand impact sur la précision des sections efficaces est la détermination du flux en neutrons incidents. Par conséquent, l'efficacité de l'instrument de mesure utilisé doit être très bien connue. Dans ce travail, ces mesures sont réalisées grâce à une chambre à fission composée de deux dépôts de ^{235}U. Des distributions en énergie typiques délivrées par une telle chambre sont montrées sur la figure Fig. 2. Sur ces spectres on distingue deux composantes principales: à gauche un pic étroit qui est dû au signal produit par les particules α provenant de la décroissance radioactive du dépôt d'Uranium, et à droite une distribution plus large qui est due à l'interaction des produits de fission dans le gaz de la chambre et qui témoigne donc de l'interaction des neutrons avec l'échantillon d'Uranium.

Afin de déterminer correctement le nombre de neutrons incidents, il faut séparer les

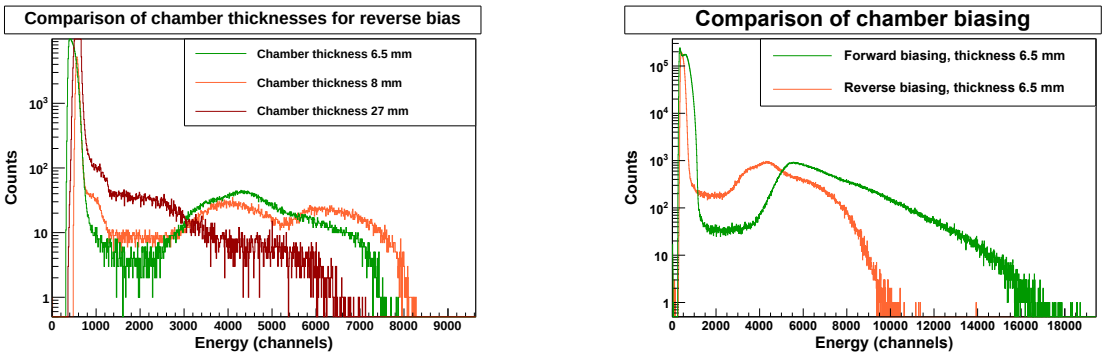

(a) (b)

Figure 2: Comparaison de différentes configurations de la chambre à fission: impact de l'épaisseur (a), effet de la polarisation (b).

deux composantes décrites ci-dessus. La meilleure façon pour s'affranchir de la composante due aux particules α consiste à appliquer une coupure franche dans la distribution en énergie. Mais ceci implique une perte d'événements qui doit être corrigée par un paramètre d'efficacité de coupure. Nous avons observé que la configuration de la chambre à fission joue un rôle important pour ce paramètre d'efficacité. En effet, selon la façon de générer le champ électrique et l'épaisseur de gaz de la chambre, les particules α et les produits de fission sont plus ou moins bien séparés (cf. Fig. 2).

Une étude détaillée (cf. Fig. 2) montre que la meilleure séparation est obtenue pour une profondeur minimale de la chambre de 6,5 mm et pour une polarisation directe (c.-à-d. une polarisation positive appliquée à l'électrode en face du dépôt), et conduit donc à une perte minimale lors de l'application d'une coupure franche.

L'optimisation du fonctionnement du détecteur étant réalisé, il reste à déterminer exactement l'efficacité de coupure. De plus, un deuxième paramètre d'efficacité se rajoute afin de tenir compte de la perte due aux événements ne génèrant aucun signal détectable. Ceci est le cas si les produits de fissions sont complètement absorbés dans la feuille d'Uranium. Ces deux paramètres ont été estimé avec des calculs classiques et des simulations. Afin de vérifier ces considérations, des mesures de calibration ont été menées à la *Physikalisch-Technische Bundesanstalt* (PTB) à Braunschweig où un flux monoénergetique de neutrons a été créé par des réactions d(D,^{3}He)n. L'efficacité a ainsi été évaluée à 94,4% avec une précision de 2,1%.

Efficacité des détecteurs HPGe

L'efficacité de détection des compteurs HPGe joue également un rôle important dans la précision globale des sections efficaces à mesurer. Dans notre cas, ce paramètre ne peut pas être déterminé par une simple mesure d'une source calibrée, puisque les échantillons utilisés sous faisceau ne sont pas ponctuels. De plus leur forte densité conduit à des effets d'auto-absorption à l'intérieur de la cible qui doivent être pris en compte. Pour cela, des simulations du dispositif expérimental, contraintes par des mesures en source calibrée, ont

été réalisées afin d'estimer précisement l'efficacité des détecteurs. Dans cette technique, des sources calibrées, ponctuelles et étendues, sont utilisées et constituent des mesures de référence. Les dimensions du cristal sont prises en compte et ajustées dans le code de simulation Geant4 de façon à obtenir le meilleur accord entre simulation et mesures. Cette étape achevée, les programmes sont capables de simuler les efficacités de détection pour des rayonnements γ d'intérêt.

Un grand désaccord entre les spécifications du cristal fournies par le constructeur et celles trouvées par simulation nous a mené à des investigations profondes sur les géométries internes des détecteurs. Après une radiographie par rayonnement X des détecteurs réalisée grâce au *Microfocus Computer Tomography* auprès du *Department of Metallurgy and Materials Engineering* (MTM) de la *Katholieke Universiteit Leuven* (KUL), les dimensions internes des compteurs ont pu être fixées. De plus des investigations auprès du constructeur des semi-conducteurs ont permis d'identifier l'origine des écarts observées entre les simulations et les mesures.

Avec ces nouvelles informations, nous avons obtenu des incertitudes variant de 2 à 3% pour les efficacités simulées.

Résultats des mesures des réactions (n,xnγ) sur ^{235}U et ^{232}Th

Les résultats présentés sont les sections efficaces de production γ et ont été obtenus en mesurant le nombre $n_\gamma(\theta_i)$ de rayonnements γ caractéristiques des réactions en question à des angles bien définis de 110° et 149°. La section efficace différentielle s'exprime alors comme:

$$\frac{\mathrm{d}\,\sigma}{\mathrm{d}\,\Omega}(\theta_i) = \frac{1}{4\pi}\frac{n_\gamma(\theta_i)}{N_{cibles}\cdot\Phi} \tag{1}$$

où N_{cibles} représente le nombre de noyaux dans la cible et Φ le flux en neutrons incidents, qui est monitoré pendant toute la mesure. Les sections efficaces totales sont obtenues par intégration, en appliquant la méthode de la quadrature de Gauss:

$$\sigma_{tot} \approx 4\pi\left[w_1^*\frac{\mathrm{d}\,\sigma}{\mathrm{d}\,\Omega}(\theta_1^*) + w_2^*\frac{\mathrm{d}\,\sigma}{\mathrm{d}\,\Omega}(\theta_2^*)\right] \tag{2}$$

avec θ_1^* = (30,6° ou 149,4°), θ_2^* = (70,1° ou 109,9°), w_1^* = 0,3479 et w_2^* = 0,6521.

Dans ce travail de thèse, deux campagnes de mesures de sections efficaces (n,xnγ) ont été réalisées sur des isotopes de ^{235}U et ^{232}Th respectivement. La première série de mesures, d'une durée de 1248 heures, a été effectuée sur une cible de ^{235}U et les rayonnements γ de 129,296 keV provenant de la diffusion inélastique et de 152,72, 200,97 et 244,2 keV issus de la réaction (n,2n) ont été observés. Dans les figures Fig. 3 nos résultats sont présentés en comparaison à des mesures antérieures et à des prédictions théoriques obtenues grâce au code TALYS, calculées par Pascal Romain du *Commissariat à l'énergie atomique (CEA), Bruyères-le-Châtel, France.*

Les différences entre les résultats de ce travail et celui de H. Karam et al. peuvent être expliquées par le fait que les valeurs des efficacités utilisées précédemment étaient affectées d'une forte incertitude systématique. Pour la transition de 129,296 keV nous pouvons observer des différences jusqu'à 25% entre les valeurs mesurées et celles prédites

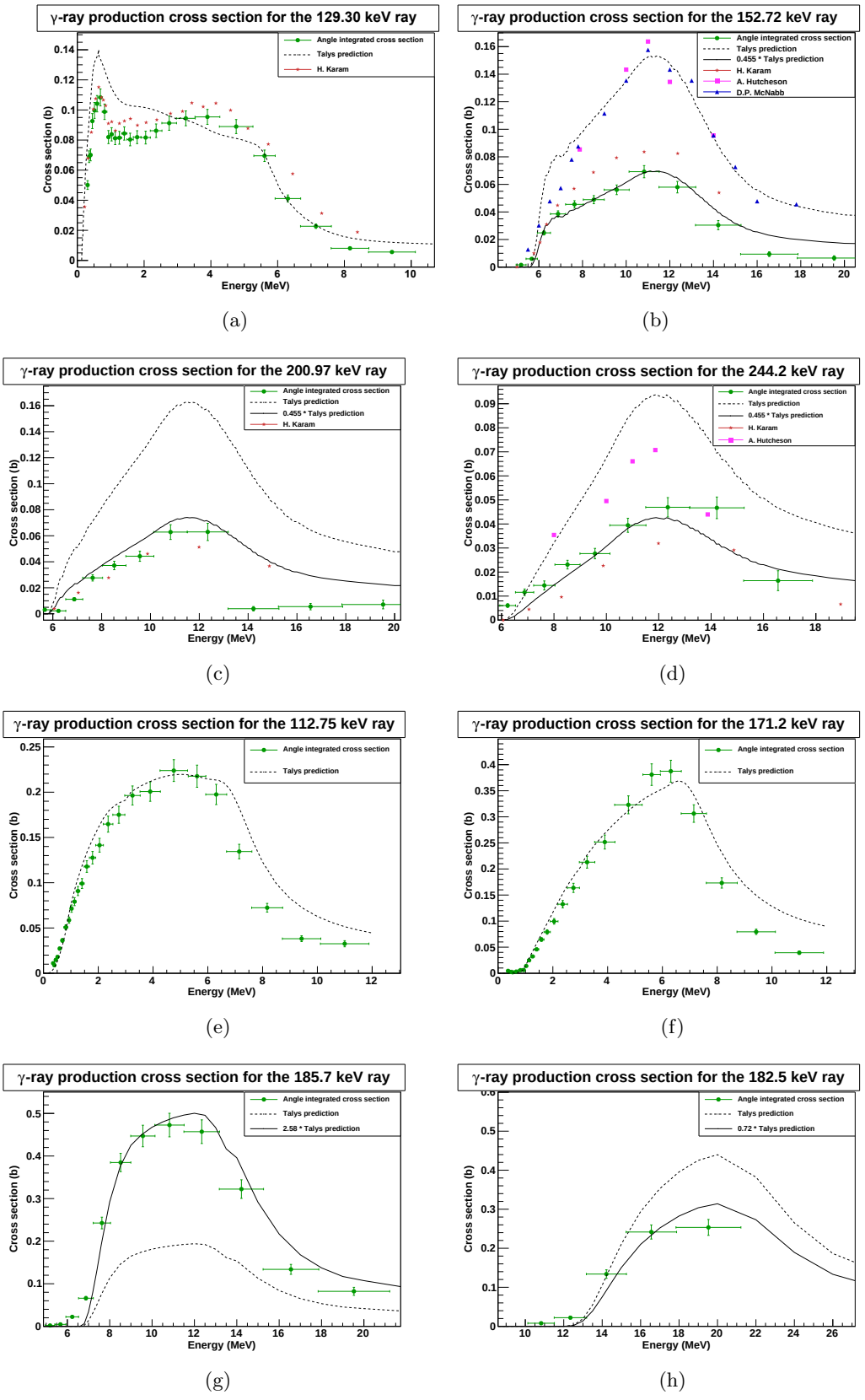

Figure 3: Exemples de sections efficaces mesurées sur ^{235}U (a)-(d) et sur ^{232}Th (e)-(h).

par la théorie. Dans le cas des transitions de 152,72, 200,97 et 244,2 keV en revanche, on note un facteur presque constant de 0.45 entre les valeurs issues du code TALYS et nos mesures. Les données expérimentales de D.P. McNabb et al. sont à considérer avec précaution, puisqu'elles ont été normalisées à l'aide d'un facteur inconnu.

Dans une seconde série de mesures, des sections efficaces sur ^{232}Th ont été analysées dans une expérience d'une durée de 375 heures. Cette mesure nous a permis d'observer les désexcitations γ de 49,369, 112,75, 171,2 et 223,6 keV suivant une diffusion inélasique, la transition γ d'une énergie de 185,7 keV provenant d'une réaction (n,2n) et celle de 182,5 keV crée par une réaction (n,3n) sur ^{232}Th. Les Fig. 3 montrent uniquement des comparaisons avec des modèles théoriques, comme il n'existe pas de données expérimentales publiées de ces réactions. Les calculs TALYS ont été réalisés par Arjan Koning du *Nuclear Research and Consultancy Group (NRG), Petten, The Netherlands*.

De ces comparaisons, nous pouvons remarquer un très bon accord pour les raies de diffusion inélastique entre nos valeurs et celles données par TALYS, même si le code théorique prévoit une partie descendante plus lente. Pour les rayonnements γ en provenance de réactions (n,2n) et (n,3n), en revanche, des facteurs de respectivement 2.6 et 0.7 peuvent être observés.

De façon générale, l'accord est assez bon pour des énergies de neutrons incidents inférieures à 8 MeV, tandis qu'au delà, les courbes TALYS divergent. Cette dernière situation peut se comprendre par le fait que dans ces régions, les réactions ont lieu via le mécanisme de pré-équilibre, pour lequel TALYS utilise une description semi-classique, ne prenant pas en compte la distribution de spin au niveau microscopique. D'autres écarts peuvent provenir du fait que pour des noyaux fissionables, la section efficace de fission (n,f) est en compétition avec les réactions (n,xn) et doit être bien paramétrée dans les codes, ce qui s'avère être très délicat à réaliser. Enfin, les rapports d'embranchement ainsi que les paramètres des densités de niveau, pour lesquels un bon ajustement est également difficile à obtenir, jouent un rôle important dans les prédictions théoriques.

Finalement, les mesures effectuées montrent que les incertitudes sur les sections efficaces peuvent descendre jusqu'à 5% si la statistique de comptage est suffisante et dans le cas contraire (énergie des neutrons élevée ou transitions moins probables) l'erreur est toutefois plus élevée.

Perspectives: Un nouveau détecteur segmenté

Les expériences réalisées dans ce travail montrent que l'erreur sur les résultats peuvent actuellement atteindre un minimum de 5%, mais uniquement sous condition de disposer d'une statistique assez importante. Dans le cas de cibles très fortement radioactives, le problème est encore plus délicat. En effet, celles-ci créent un fond constant de comptage, et par conséquent un temps mort de détection élevé ce qui se traduit par une perte d'événements et donc de statistique.

Afin de remédier à ce problème et de rendre possible des mesures de haute précision sur des cibles comme ^{233}U, nous avons étudié la possibilité de segmenter l'électrode du cristal de Germanium afin de le séparer en pixels indépendants. En fait, cette pixelisation revient à réduire le volume du cristal et par voie de conséquence le temps mort dû à un

comptage élevé.

Dans un tel cristal, un effet d'induction fait que lors de la détection d'un signal dans une cellule, une charge miroir est créée dans les cellules avoisinantes pendant le temps de montée du signal original. Comme la présence d'une telle charge miroir peut affecter la détection simultanée d'un événement dans une cellule, des simulations avec le logiciel MGS[4] ont été réalisées afin d'étudier l'impact de différents scénarios de segmentation sur l'amplitude de ces signaux.

Ce travail a montré que les charges miroirs dépendent du volume des pixels, et sont plus faibles si les segments de l'électrode sont légèrement espacés. La meilleure configuration est une segmentation en 6x6 pixels avec un espace de 0,5 mm entre chaque pixel. Cette étude a donc permis de concevoir un tel détecteur qui a été acheté grâce au financement du projet DISPALEND de l'Agence Nationale pour la Recherche (ANR), et qui sera livré fin de l'été 2010. Après des tests de caractérisation, il complètera le dispositif expérimental à Geel ce qui permettra d'étudier des réactions (n,xnγ) sur des cibles très fortement radioactives.

Conclusions

Les travaux menés au cours de cette thèse ont permis de créer un dispositif expérimental capable d'évaluer les sections efficaces des réactions (n,xnγ) avec une précision allant jusqu'à 5% et de développer un nouveau détecteur destiné à étendre cette capacité à des cibles très fortement radioactives.

Nous avons ainsi pu estimer les sections efficaces des réactions (n,xnγ) sur les noyaux ^{235}U et ^{232}Th et observer des grandes différences entre les prédictions théoriques et nos mesures. Néanmoins les résultats obtenus contribueront à l'amélioration de la paramétrisation des codes théoriques.

Tout prochainement, l'équipement réalisé sera utilisé pour observer, entre autres, les réactions de diffusion inélasique sur ^{238}U, une mesure qui fait partie de la liste des données nucléaires de haute priorité de l'OCDE.

[4]Multi Geometry Simulation, développé à l'IPHC

Abstract

The design of Generation IV nuclear reactors and the research of new fuel cycles require knowledge of the cross sections of different nuclear reactions. The research in this work is focused on cross section measurements of (n,xnγ) reactions occurring in these new reactors. The aim is to measure unknown cross sections and to reduce the uncertainty on current data relative to reactions and isotopes present in transmutation or regeneration processes.

The presented work consists of studying ^{232}Th(n,xnγ) and ^{235}U(n,xnγ) reactions in the fast neutron energy domain (up to 20 MeV) with the best precision possible. The experiments are performed at GELINA which delivers a pulsed, white neutron beam at IRMM, Belgium. The time characteristics of the beam enable us to measure neutron energies with the time-of-flight (TOF) technique. The neutron induced reactions (in this case inelastic scattering, (n,2n) and (n,3n) reactions) are identified by online prompt γ spectroscopy with an experimental setup including four HPGe detectors. A double layered fission chamber is used to monitor the incident neutron flux. The obtained results are presented and a comparison between the measured cross sections and the TALYS code predictions will be discussed.

In order to achieve a very high precision on the reaction cross sections, an extensive work has been realised on the detection efficiencies of the counters used in the experiment. These quantities were in fact the largest sources of uncertainty in foregoing campaigns. After important efforts including high precision measurements together with Geant4 simulations, the efficiency of the fission chambers as well as of the HPGe detectors could be determined with accuracies below 3%, accomplishing the final goal of a cross section determination with a precision of 5%.

This work is a further step in the preparation of the measurement of ^{233}U(n,xnγ) reactions, which are completely unknown at this stage although of very high importance in the ^{232}Th regeneration process. For this reason, a new, segmented HPGe detector was conceived, which will complete the current experimental setup.

Acknowledgements

I would like to thank several people who, in different ways, contributed to the accomplishment of this Ph.D. thesis.

First, I have to thank my advisor, Philippe Dessagne, for his guidance and support through the past years of study. Moreover, I would like to thank the entire research team of the *Groupe de Recherche pour l'Aval du Cycle Électronucléaire*, especially Gérard Rudolf for accepting me as a fellow in his research group, but also Maëlle Kerveno for her help on this dissertation. Without this fruitful collaboration, this work would not have been possible.

I have been privileged to work with a number of skilled an knowledgeable researchers from different laboratories during this work. In particular, I would like to thank Arjan Plompen from the *Institute for Reference Measurements and Materials (IRMM), Geel, Belgium*, Catalin Borcea and Alexandru Negret from the *Horia Hulubei National Institute of Physics and Nuclear Engineering, Bucharest, Romania* and Ralf Nolte from the *Physikalisch-Technische Bundesanstalt (PTB), Braunschweig, Germany*, who exemplify the model of responsible and successful researchers.

I am indebted to Jean-Pierre Engel for our extensive discussions about data treatment and error calculations, to Cayetano Santos for his help on the data acquisition system, to the entire team of the IRMM in Geel for interesting discussions and their constant support and to the scientists of the PTB in Braunschweig for the endless coffee breaks during our nightshifts.

A special thank should go to Janos Polonyi, Eric Christoffel and Patrick Levèque who constantly supported me with my teaching assistance during this Ph.D. thesis.

I owe my deepest gratitude to my University professor Abdel-Mjid Nourreddine, whose passion and interest for nuclear physics inspired me through my entire formation. His constant support and persistence played a key role in the choice of my studies.

Also I want to thank the other members of my thesis committee, namely Bernard Haas, Frank Gunsing and Jean-Claude Steckmeyer, and everyone else who contributed to this work and who I have not mentioned personally.

Finally the most important I have to thank are my family and friends, and mostly my girlfriend Marilyn, for their continuous support.

Contents

List of Figures

List of Tables

Chapter 1

Introduction

This chapter is a general initiation into the domain of energy needs and production, with a special focus on nuclear energy. After the introducing sections, the context of nuclear energy and its future is discussed along with the required research that has to be made in this field. The chapter is concluded by the situation of the performed measurements in this work.

1.1 Energy consumption and needs

The past decades show that the growth of the population as well as of the economy leads to ever higher energy consumptions. Indeed, the evolution of the world energy consumption is mainly affected by two major aspects. On one hand, the earth population is constantly growing with a current rate of approximately 200 000 inhabitants per day, which corresponds to an annual increase of the order of 1%. In order to provide these people with energy, it would thus be necessary to increase the energy production by the same factor each year. On the other hand, there are many people living in the developing countries whose energy demand for the next decades will increase. In fact, today more than 20% of the world population, roughly 1.5 billion people do not have access to electricity [1].

These two factors indicate a very significant increase in energy consumption for the next decades. Globally, assuming no change in energy politics, the International Energy Agency expects the world primary energy demand to increase by 40% by 2030.

On another topic the energy production is currently strongly dominated by fossil fuels. Around 80% of the energy consumed in the world in 2006 is coming from the combustion of coal, oil and gas as shown in figure 1.1. These fuels however are present in limited quantities only. According to different studies [3] the proven quantities of oil left will be sufficient for the next 42 years, for natural gas 60 years and for coal 122 years assuming a constant use. Even if further discoveries of reserves will extend the deadlines, these fuels cannot be used to serve the growing consumption in long term.

Furthermore, another disadvantage of these fossil fuels is the CO_2 gas produced during their combustion. Indeed, CO_2 is a greenhouse gas i.e. it contributes to the global warming of the planet. To prevent the effects of this gas and to avoid a possible climate change induced by the burning of CO_2 emitting fuels, many countries agree on cutting back on

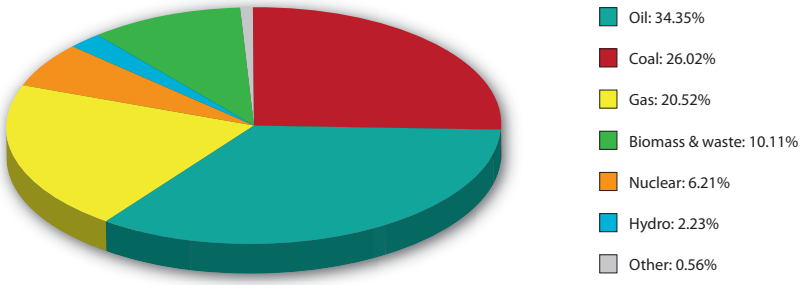

Figure 1.1: Share of the different energy resources in the world total primary energy production 2006 according to [1].

fossil fuels in the energy production.

Following this approach, the only energy resources left to cope with the ever growing energy needs are the nuclear and renewable energies, which contribute today with less than 20% to the primary energy production. The challenge to avoid energy lacks is thus extremely high and cannot be faced by one single alternative production. In the short and mid-term range nuclear energy will have to play an essential role in the energy supply of the planet [2].

1.2 Nuclear energy

The nuclear energy resource is most commonly used to produce electricity. In a reactor, atomic nuclei are exposed to a high neutron irradiation which makes the isotopes of the nuclear fuel undergo fission. As this process is exothermic, heat is released which can be used to power turbines and hence generate electricity.

A very important aspect of nuclear reactors is the nuclear fuel used. Indeed, this fuel must fulfil two important properties. First, it has to be fissionable, i.e. it must be able to undergo the process of nuclear fission. Secondly its fission barrier must be sufficiently low to achieve this after capturing low-energy thermal neutrons. Isotopes meeting both of these conditions are called *fissile*. The only fissile isotope which is sufficiently abundant in nature to be exploited and used in reactors is ^{235}U. Unfortunately this uranium isotope only presents roughly 0.7% of the natural uranium available, the most dominant part being ^{238}U with an abundance of nearly 99.3%. With such a weak percentage of fissile uranium available, the known reserves of today will be consumed by the end of this century assuming a constant fuel burn up [3].

Another issue of nuclear energy is the radioactive waste which is produced, mainly due to the extraction of the used fuel and reactor dismantling. This waste is the major drawback of the current nuclear energy cycle and has to be dealt with to take the best use of this energy resource.

These two aspects are treated in more detail along with possible solutions in the next two sections.

1.2.1 Future reactors

As already mentioned above, the exhaustion of the fissile ^{235}U isotope calls for new reactors running on another nuclear fuel. The main idea behind the conception of these reactors is the generation of new nuclear fuel by introducing so-called fertile isotopes into the reactor. These are nuclei which can be transformed, after a certain number of nuclear reactions, into fissile material. One example of a fertile isotope is ^{238}U. This one can indeed be transformed into the fissile ^{239}Pu inside the reactor itself by neutron capture and two successive β decays:

$$^{238}\mathrm{U}(\mathrm{n},\gamma)^{239}\mathrm{U} \xrightarrow{\beta^-} {}^{239}\mathrm{Np} \xrightarrow{\beta^-} {}^{239}\mathrm{Pu} \tag{1.1}$$

This is referred to as the uranium/plutonium (U/Pu) fuel cycle.

As 99.3% of the natural Uranium is ^{238}U, this technique enables us to regenerate fuel and to continue exploiting nuclear power for a very long time. This regeneration process however is best achieved in so-called fast reactors, driven by unmoderated fast neutrons unlike the current thermal reactors, where the neutrons are strongly moderated to benefit from a better ^{235}U fission cross section.

For this reason new reactors must be developed to take these regeneration scenarios into account. This is achieved by the Generation IV International Forum [4], a special organisation founded in 2001 and involving 13 countries, coordinating the research and developing of new promising techniques for nuclear reactors. Their major objectives include the optimisation of the resource use through an efficient and flexible use of the available resources in fissile and fertile materials, improved safety and reliability and enhanced resistance to proliferation risks. They also tend to develop solutions to minimise radioactive waste production as will be discussed in the following section.

A possible alternative to the U/Pu fuel cycle is the thorium/uranium (Th/U) cycle. In this scenario ^{232}Th is used as fertile material to generate fissile ^{233}U by successive β decay:

$$^{232}\mathrm{Th}(\mathrm{n},\gamma)^{233}\mathrm{Th} \xrightarrow{\beta^-} {}^{233}\mathrm{Pa} \xrightarrow{\beta^-} {}^{233}\mathrm{U} \tag{1.2}$$

Although this cycle is not prioritarily studied for fuel usage in reactors, it presents a certain number of advantages. Indeed the lighter ^{232}Th nucleus is less likely to produce heavy actinides as in the U/Pu cycle, which are more delicate in terms of waste management. Another convenience is that thorium is much more abundant in nature than uranium, thus extending the possibilities of nuclear energy in the future.

1.2.2 Nuclear waste

An inconvenience of the nuclear energy cycle is the nuclear waste generated in the structures of the reactor confinement by irradiation as well as the remaining of the used fuel. Very short-lived radioactive isotopes can be dealt with relatively easily. Isotopes presenting a short life-time are strongly radioactive and their decay is rather fast. After a storage of several decades they don't present radiative risks anymore and can be treated without special precautions.

The main focus lies on the mid- and long-lived radioactive nuclei, which present a high radiotoxicity risk even after several centuries of storage. In order to dispose of these

nuclei in the best way possible, two scenarios are applicable depending on the nature of the isotope in question [5]. The first one consists in incinerating the radioactive nuclei. In this process, the waste is introduced into a high neutron flux which induces fission of the isotopes in question. The fission products created are less radioactive than the original waste and decay much faster. The second possibility is transmutation. For this method the nuclei are also exposed to neutron radiation, and similarly as in the regeneration process illustrated above, the nuclei will capture neutrons and transform into isotopes of shorter life-time. A good example of such a transmutation application is ^{99}Tc, with a half-life of 200 000 years:

$$^{99}\mathrm{Tc}(\mathrm{n},\gamma)^{100}\mathrm{Tc} \overset{\beta^-(16\ \mathrm{s})}{\longrightarrow} {}^{100}\mathrm{Ru} \tag{1.3}$$

The ^{100}Tc isotope created by capture has a half-life of 16 s before decaying to the stable ^{100}Ru.

For both methods long-lived isotopes are transformed into short-lived ones and after a short while the waste is free from radiotoxicity and can be stored safely without jeopardy. Unlike the transmutation process, the incineration is best accomplished in the fast neutron domain, as the neutron induced fission cross sections are favourable here.

Several Generation IV reactor projects deal with the possibility of introducing waste into the reactor to transmute or incinerate it. Another type of installation that is studied for this purpose are Accelerator-Driven Systems (ADS). These are subcritical reactors designed especially to incinerate radioactive waste.

It is however noteworthy to mention that the transmutation or incineration of radioactive waste is not straightforward for every nucleus. In some cases an intense neutron bombardment could even create longer lived isotopes an thus increase radiotoxicity. For this reason it is of upmost importance to separate the isotopes of interest from the undesired ones before introducing them into such a facility.

1.3 (n,xn) reactions

As we have already mentioned before, nuclear waste management needs to exploit the fast neutron domain, especially for the incineration process. This energy range however is not known precisely enough today to make reliable and accurate calculations for new reactors, needed to obtain the best energy efficiency and safety for the future reactors.

Indeed the fast neutrons present in these reactors are involved in a certain number of threshold reactions that do not exist for thermal neutrons, which do not have sufficient energy to invest in these reactions. The most important example of such reactions are (n,xn) reactions, including for x = 1 inelastic scattering, (n,2n) and (n,3n) reactions.

These ones are of great importance, as they have a major impact on the reactor core in several ways. First, they are an important neutron slow down process. Neutrons which experience inelastic scattering for example leave the touched nucleus in an excited state, and thus lose a part of their energy in this process. It is important to estimate this energy loss of the neutrons inside the reactor, as all their reaction cross sections strongly depend on their kinetic energy.

A second reason for the importance of these reactions is neutron multiplication. When considering for example (n,2n) reactions, each such process produces an additional neutron

which is released into the reactor core. Knowledge of the number of neutrons present is a key issue in nuclear energy production, as the neutrons are responsible for inducing fission reactions, and have thus a major impact on the criticality of the reactor.

Another issue of these reactions is that they produce new isotopes which have to be dealt with inside the core. This can be illustrated in the case of the Th/U cycle, where ^{233}U is used as nuclear fuel. A (n,2n) reaction on ^{233}U leads to the creation of ^{232}U. In its decay chain the ^{208}Pb isotope is eventually produced, which is an emitter of a γ radiation of 2.6 MeV. This very energetic radiation can have significant repercussions on the reactor core temperature and must be estimated for the reactor dismantling, as it penetrates deeper in the structures.

1.3.1 The current needs

Measurement of these (n,xn) reactions involves many different isotopes, mainly those of the nuclear fuel and their descendants but also of the reactor structures. In fact, the production of new nuclei caused by these reactions changes the behaviour of the reactor criticality, meaning that uncertainties on these quantities introduce further uncertainties on the response of the core. Very small errors on an important isotope participating in neutron induced reactions can then lead to large uncertainties on the reactor criticality [6]. For this reason, priority lists of isotopes are established indicating desired precisions for reactions of interest [7].

Current demands for measurements include the inelastic scattering and (n,2n) reactions on ^{235}U, as the ^{235}U nuclear fuel will stay present even in the U/Pu cycle. For the Th/U cycle, these reactions are needed for the ^{232}Th isotope. A precision of 5% on these data should be obtained.

Further needs for high precision measurements are inter alia the inelastic scattering on ^{238}U, for which a target accuracy better than 3% is desired [8] as well as inelastic scattering and (n,2n) reactions on ^{233}U, for which no differential experimental data exists at this stage.

1.3.2 State of the art

While previous projects of our collaboration [9, 10] have already studied the feasibility of measuring (n,xn) reactions on radioactive isotopes using the prompt γ spectroscopy method, this work focuses on the precision of the existing technique. As mentioned in section 1.3.1, it is of upmost importance to develop an experimental setup, able to reduce the uncertainties on the measured quantities to a minimum, to fulfil the standards needed for the design of new nuclear reactor types.

The aim of this work is to work out a measurement technique able to decrease the uncertainties on the cross section data to 5% or below. For many important isotopes, this precision can be interpreted as the maximum error tolerable for the measurement of (n,xn) reaction cross sections.

In the next chapters all the information needed to understand the experimental technique used to probe the (n,xnγ) reactions is provided. First, the theoretical backgrounds are presented along with the different measurement techniques in chapter 2.

The experimental setup used for these measurements is presented in detail in chapter 3. In fact, the same experimental technique was applied as in the previous projects, but the setup was completely rebuilt to discard noise effects and to improve the precision of the results. A special emphasis is made on the shielding efforts that were made on the setup.

As the efficiencies of the detectors used in this work, namely HPGe detectors and a fission chamber, present the major impact on the uncertainties created by the experiment, a special chapter is dedicated to the extensive work that has been realised to reduce this error to a minimum. The two detector types are studied in detail in chapter 4.

Chapter 5 presents the results of measurement campaigns, that have been realised on (n,n'γ) and (n,2nγ) reactions on ^{235}U and (n,n'γ), (n,2nγ) and (n,3nγ) on ^{232}Th. The obtained results are discussed and compared to theoretical predictions computed with the TALYS code.

Another objective of this work is to enable the setup to be used on very highly radioactive isotopes, such as ^{233}U. In fact the radioactive decay of such isotopes presents a very high background noise on the detectors, inducing a large dead time. For this purpose a new, segmented HPGe detector was designed and is presented in chapter 6, before concluding this work in the final chapter 7.

Bibliography

[1] International Energy Agency, *World Energy Outlook*, 2008 Edition, OECD.

[2] S. Bouneau, S. David, J.-M. Loiseaux, O. Méplan, *Construction d'un monde énergétique en 2050*, Volume 34, No 1, EDP Sciences, 2009.

[3] Commissariat à l'Énergie Atomique (CEA), *Mémento sur l'énergie - Energy Handbook* - Edition 2009.

[4] The Generation IV International Forum, online: http://www.gen-4.org/

[5] J.L. Bobin, E. Huffer, H. Nifenecker, *L'énergie de demain*, EDP Sciences, 2005.

[6] M. Salvatores et al., *Nuclear data needs for advanced reactor systems: a NEA Nuclear Science Committee initiative*, Proceedings of the International Conference on Nuclear Data for Science and Technology, April 22-27, 2007, Nice, France, EDP Sciences, 2008, p. 879-882.

[7] Nuclear Energy Agency, OECD, *Nuclear Data High Priority Request List*, online: http://www.nea.fr/dbdata/hprl/

[8] M. Salvatores et al., *The role of differential and integral experiments to meet requirements for improved nuclear data*, Proceedings of the International Conference on Nuclear Data for Science and Technology, April 22-27, 2007, Nice, France, EDP Sciences, 2008, p. 883-886.

[9] S. Lukić, *Mesure de sections efficaces de réactions (n,xn) par spectroscopie γ prompte auprès d'un faisceau à très haut flux instantané*, Ph.D. thesis, No d'ordre 4647, Université Louis Pasteur, Strasbourg, 2005.

[10] H.C. Karam, *Mise au point de la mesure de sections efficaces de réations (n,xn) par spectroscopie γ prompte sur des cibles très radioactives*, Ph.D. thesis, No d'ordre 0036, Université de Strasbourg, Strasbourg, 2009.

Chapter 2

Theory and methods for (n,xn) reactions

This chapter is an introduction to the theoretical backgrounds and measurement techniques appearing throughout the entire work.

In the first section, the main theoretical aspects needed to understand the backgrounds of (n,xn) reactions are presented. A brief recall of some general features of nuclear reactions is given, before discussing the different reaction mechanisms leading to the formation of the final nuclei. As these are most often produced in an excited state, we present the γ ray emission properties by which the nuclei decay to their ground state. These are of upmost importance in this work, as the reactions of interest are measured by the detection of these emitted γ rays.

The second part of this chapter is about the different methods which can be used to measure (n,xn) reaction cross sections, a special emphasis is made on the prompt γ-ray spectroscopy technique used in this work.

2.1 Theoretical Background and Models

This section presents a brief introduction to the main theoretical ingredients required to understand the basis of the reactions studied in this work. It is to be seen as a recall of the most important features needed to measure (n,xnγ) reactions, without claiming to be an exhaustive dissertation. More details on the different aspects presented can be found in the references cited throughout the chapter.

2.1.1 Reactions and thresholds

Nuclear reactions are interactions occurring via nuclear forces. They can take place when an energetic particle approaches a target nucleus sufficiently close enough [1]. Such reactions, implying a projectile a and target nucleus X resulting in products Y and b can be written as

$$a + X \rightarrow Y + b \tag{2.1}$$

or, in a more compact way:

$$X(a,b)Y \tag{2.2}$$

The benefit of the second notation is that it emphasises the given reaction type, also called reaction channel. These are classes of reactions sharing common properties. Studied reactions in this work include (n,n') and (n,2n) reactions.

The probability of such reactions taking place is referred to as the *reaction cross section*. It depends on the structure of the nucleus in question and, for a given isotope, on the incident projectile energy. It is expressed in units of *barns*, where 1 b = 10^{-28} m^2.

For these reactions we can define the Q *value* by

$$Q = (m_X + m_a - m_Y - m_b) \cdot c^2 \tag{2.3}$$

where m_i are the rest masses of the reaction participants. As nuclear reactions are governed by certain conservation laws, such as the *conservation of the total energy*, the Q value may also be written as

$$Q = T_Y + T_b - T_X - T_a \tag{2.4}$$

where T_i denote the kinetic energies of the reaction participants.

In case of positive Q values, so called *exothermic* reactions, energy is released in form of kinetic energy of the products. For negative Q values, i.e. *endothermic* reactions, energy must be furnished by the incident particle for the reaction to be possible.

This is also the case for (n,2n) reactions, where the Q value corresponds to the neutron separation energy S_n [2]:

$$S_n = -Q \tag{2.5}$$

In these particular reactions, which may be expressed as

$$^{\mathrm{A}}_{\mathrm{Z}}\mathrm{X} + \mathrm{n} \rightarrow \ ^{\mathrm{A}-1}_{\mathrm{Z}}\mathrm{X}^* + 2\mathrm{n} \tag{2.6}$$

the neutron separation energy corresponds to the mass difference of the final and initial participants:

$$S_n = (m_{^{\mathrm{A}-1}_{\mathrm{Z}}\mathrm{X}^*} + m_{\mathrm{n}} - m_{^{\mathrm{A}}_{\mathrm{Z}}\mathrm{X}}) \cdot c^2 \tag{2.7}$$

where $^{\mathrm{A}}_{\mathrm{Z}}\mathrm{X}$ denotes an isotope of atomic mass number A and atomic number Z. The asterisk shows the possibility of an excited residual nucleus.

A representation of (n,n'), (n,2n) and (n,3n) reactions on ^{232}Th is shown in figure 2.1 for which the cross section data has been retrieved from the ENDF/B-VII.0 database. Knowledge of these reactions is of high importance, as their cross sections are above several barns. In the figure one can also observe the neutron separation threshold energies which are in the order of several MeV for these reactions.

2.1.2 Reaction mechanisms

Nuclear reactions may take place in a variety of ways, depending on the nature and energy of the incident particle and of the reaction channel. While many different models describing these interactions exist, we will focus on the three main mechanisms involved

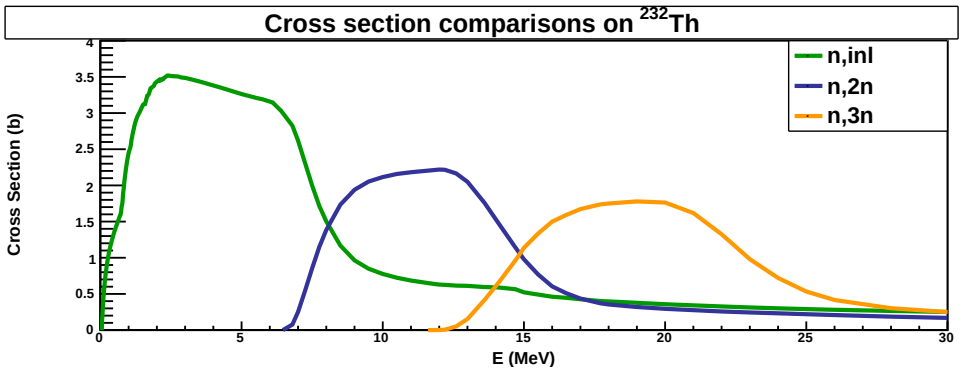

Figure 2.1: Comparisons of the (n,n'), (n,2n) and (n,3n) reaction cross sections on ^{232}Th from the ENDF/B-VII.0 database.

in modelling (n,xn) reactions: *Direct reactions*, *Compound nucleus reactions* and *Pre-equilibrium reactions*. In all these reactions the incident neutron is absorbed by the target nucleus, and reemitted after a certain process, differing from reaction type to type. The mechanism dominating the interaction depends strongly on the energy of the incident, and thus also of the outgoing particle(s). This is shown schematically in figure 2.2 and discussed in the following subsections.

2.1.2.1 Direct Reactions

Direct reactions are likely to occur for rather high projectile energies. For these energies the *de Broglie wavelength* of the incident particle is small enough to interact with individual nucleons of the target nucleus. In fact a 20 MeV nucleon has a de Broglie wavelength of about 1 fm, and thus is likely to interact in a direct reaction mechanism.

In this mechanism the incident neutron interacts with a single nucleon, or a small group of nucleons. It is primarily a surface reaction, without creation of an intermediate state. The reaction is very fast, typically around 10^{-22} s which corresponds to the time needed by the incident neutron to traverse the target. Ejected particles in such reactions have a highly anisotropic, forward-peaked angular distribution.

Direct Reactions can be predicted using different models, such as the *Optical Model* [3]. This model is based on the introduction of a one-body complex potential, which yields correct particle wavefunctions for elastic scattering. In the case of inelastic scattering, approximate solutions can be obtained using algorithms as the *Distorted Wave Born Approximation* for spherical nuclides, *coupled-channel* for deformed nuclides and the *weak-coupling model* for odd nuclei.

2.1.2.2 Compound Nucleus Reactions

In compound nucleus reactions, the incident particle is completely absorbed by the target nucleus. These reactions occur for low projectile energies, for which the de Broglie wavelength is too large to interact with individual nucleons, and thus the reaction affects

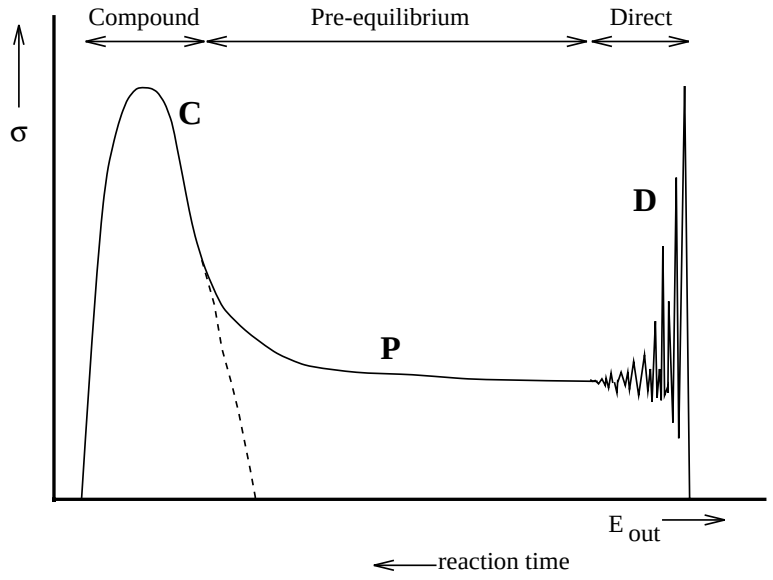

Figure 2.2: Strength of the different mechanisms dominating depending on the particle energy: at low energies the reaction is dominated by the compound nucleus mechanism, at high energies it is ruled by the direct type and the intermediate domain is governed by pre-equilibrium reactions [9].

the entire nucleus. A characteristic neutron energy for this mechanism is 1 MeV, for which the de Broglie wavelength is around 4 fm.

After the capture of the projectile its exceeding energy is shared and re-shared among the nucleons of the compound nucleus formed before reaching a statistical equilibrium. At this point the "memory" of the formation process of the compound nucleus is lost. The average energy gained by the nucleus is not sufficient per nucleon to escape directly, but due to statistical fluctuation of random collisions inside the nucleus it will be possible for a neutron, proton or composed particle to escape through *evaporation*. As the relaxation process is completely independent of the formation process, the ejected particles have an isotropical angular distribution. This process is much slower than direct reactions, the life time of the compound nucleus can reach up to 10^{-15} s.

This type of reactions can be modelled using different theories such as the *Weisskopf-Ewing theory* or the more recent *Hauser-Feschbach theory* taking account of the conservation of angular momentum. The latter one can be completed using the *Hofmann-Richert-Tepel-Weidenmüller (HRTW)* model, the *Moldauer expression* or the *Gaussian orthogonal ensemble (GOE)* approach, to take into account possible correlations between incoming and outgoing channels.

2.1.2.3 Pre-equilibrium Reactions

An intermediate reaction mechanism, between direct reactions and compound nucleus reactions, is the pre-equilibrium mechanism. In fact, it is possible for a nucleon to escape the nucleus before the statistical equilibrium is established. In this case the projectile energy is shared among a certain number of nucleons only, and during the cascade of further nucleon-nucleon interactions, a neutron or proton is emitted.

This process is characterised by a partial loss of memory of the formation process of the pre-compound nucleus. It results that its angular distribution is forward-peaked, but less sharply than those of direct reactions. The duration of these reactions is intermediate between direct and compound nucleus reactions.

These reactions can be simulated using the one or two component *Exciton model*.

2.1.3 Reactions in competition with (n,xn) reactions

As seen just above, the absorption of a neutron by a target leaves the formed intermediate nucleus in an excited state. The decay of the latter one can occur through different reaction channels. The ones studied in this work are (n,xn) reactions, i.e. the emission of one or several neutrons by the excited target, but this is not the only reaction type that can lead to the decay.

A reaction channel in competition with (n,xn) reactions is the process of neutron induced fission (n,f). This can be interpreted by the *Compound nucleus reaction mechanism* and the *Liquid drop model*. In fact, after the absorption of an incident neutron, the exceeding energy of the nucleus allows it to undergo states of collective deformation. While the nuclear force tends to keep the nucleus in a spherical shape, the large nuclear charge in heavy nuclei lead to *Coulomb repulsion*, and support the deformation process. At a critical point, this repulsion dominates over the nuclear force, and the nucleus divides into two neutron rich fragments, which decay by the prompt emission of neutrons [3]. This effect can however only occur in rather heavy nuclei.

The different possible decay reactions are linked to each other, and it is important to consider all these channels when modelling the reactions in order to obtain reliable results.

2.1.4 γ ray emission

For the considered reactions, the resulting nucleus is mostly not left in its ground state and thus deexciting will occur. This can be achieved in several ways: when the energy is sufficient, particle emissions can lead to decay as described above, but when the remaining energy is not large enough to eject particles from the nucleus, it is disposed of by the radiative transitions between quantised energy levels in the nuclei [1]. The properties of these γ emissions are discussed in the following subsections.

2.1.4.1 Multipolarity

The law of conservation of angular momentum and parity imply a set of rules for γ transitions between two given nuclear states [3]. For a radiative decay between states with

angular momentum and parity J_i,π_i and J_f,π_f respectively, the multipolarity L of the emitted γ ray must satisfy:

$$|J_i - J_f| \leq L \leq J_i + J_f, \quad L \neq 0 \tag{2.8}$$

If the transition is not affected by parity change, i.e. $\pi_i = \pi_j$, the transitions of even multipolarity are electric, while those corresponding to odd orders are magnetic. They are denoted M1, E2, M3, E4, etc.

For transitions between two states of different parity, i.e. $\pi_i = -\pi_j$, the even order transitions are magnetic and the odd ones are electric, denoted E1, M2, E3, M4, etc.

According to Weisskopf [2], the transition probability for magnetic transitions are much weaker than those for electric transitions for a given order and the γ decay rate decreases rapidly as the multipolarity of the emitted radiation increases [4]. This means that in most cases it is sufficient to take into account the lower order transitions only, knowing that it is possible for electric transitions to be in competition with a higher order magnetic transition:

- for $J_i \neq J_f$ and $\pi_i\pi_f = (-1)^{|J_i - J_f|}$, the dominant multipole is electric of order $L = |J_i - J_f|$
- for $J_i \neq J_f$ and $\pi_i\pi_f = (-1)^{|J_i - J_f|+1}$, the lowest order multipole is magnetic of order $L = |J_i - J_f|$ in competition with a higher order $L = |J_i - J_f| + 1$ electric multipole
- for $J_i = J_f \neq 0$ and $\pi_i\pi_f = 1$, the lowest allowed order is a magnetic multipole of first order (M1), in competition with an electric transition of second order (E2)
- for $J_i = J_f \neq 0$ and $\pi_i\pi_f = -1$, the favoured transition is electric dipole (E1).

2.1.4.2 Angular Distribution

The angular distribution of the emitted γ radiation is not isotropic. Its distribution depends strongly on the multipolarity L of the γ transition, but not on the reaction mechanism in which the nucleus was formed, contrary to the spacial distribution of massive particles emitted by the excited nucleus.

In the case where the target is bombarded by a unidirectional beam, the distribution function is independent on the azimuth angle φ, whereas its dependence along the inclination angle θ can be expressed as a series of Legendre polynomials $\mathrm{P}_i(\cos\theta)$. A schematical representation of this symmetry is shown in figure 2.3, where the blue cones represent regions for which the observed angular cross section is constant. The differential cross section $\frac{\mathrm{d}\,\sigma}{\mathrm{d}\,\Omega}$ can be written as [5]:

$$\frac{\mathrm{d}\,\sigma}{\mathrm{d}\,\Omega}(\theta) = \frac{\sigma_{tot}}{4\pi} \cdot \sum_{i=0}^{\infty} \alpha_i \,\mathrm{P}_i(\cos\theta) \tag{2.9}$$

where σ_{tot} is the total angle-integrated cross section, and the α_i are coefficients depending on the angular momentum of the initial and final state J_i, J_f and the transition multipolarity L [6]. As the highest order Legendre polynomial in the decay distribution has

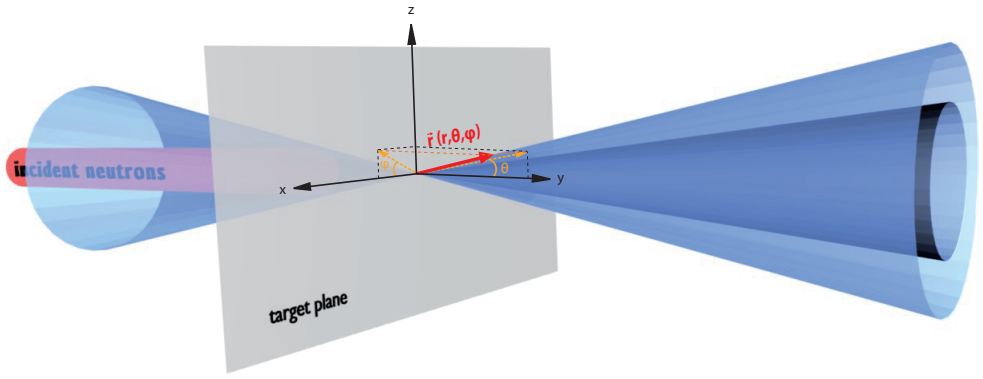

Figure 2.3: Schematical representation of the angular distribution.

an order $\leq 2L$ and $\leq 2J_i$, this infinite summation can be limited to M terms, where M = min{2L,2J_i}.

The total cross section for a given γ ray emission is obtained by integrating the differential cross sections over all angles:

$$\sigma_{tot} = \int_{4\pi} \frac{\mathrm{d}\,\sigma}{\mathrm{d}\,\Omega}(\theta)\,\mathrm{d}\,\Omega = 2\pi \int_{-1}^{1} \frac{\mathrm{d}\,\sigma}{\mathrm{d}\,\Omega}(\theta)\cos\theta \tag{2.10}$$

This can be conveniently achieved using Gauss-Legendre integration. In fact the Gaussian quadrature rule says that the integral of a polynomial $f(x)$ of degree less or equal to 2N-1 in the interval [-1,1] can be expressed as discrete summation of the function $f(x)$ evaluated at the N zeroes x_i of the Legendre polynomial $\mathrm{P}_N(x)$ and a weighting function [7]:

$$\int_{-1}^{1} f(x)\,\mathrm{d}\,x \approx \sum_{i=1}^{N} w_i f(x_i) \tag{2.11}$$

Using equations (2.10) and (2.11), σ_{tot} can be expressed as:

$$\sigma_{tot} \approx 2\pi \sum_{i=1}^{N} w_i \frac{\mathrm{d}\,\sigma}{\mathrm{d}\,\Omega}(\theta_i) \tag{2.12}$$

where the θ_i are chosen to correspond to the N nodes of the Legendre polynomial $\mathrm{P}_N(x)$. The weighting coefficients w_i for the values N = 2 and 4 are given in table 2.1. They have been computed according to the formula [7]:

$$w_i = \frac{2}{(1-x_i^2)|P'_N(x_i)|^2} \tag{2.13}$$

N	$\cos(\theta_i)$	θ_i	w_i
2	0.5774	54.7°	1.0000
	-0.5774	125.3°	1.0000
4	0.8611	30.6°	0.3479
	0.3400	70.1°	0.6521
	-0.3400	109.9°	0.6521
	-0.8611	149.4°	0.3479

Table 2.1: Roots and weighting coefficients for the Gauss-Legendre integration for N = 2 and 4.

Furthermore, electromagnetic transitions inside nuclei have the property of connecting two states with well defined parity. This implies that the plane perpendicular to the beam axis including the target nuclei is a symmetry plane, i.e.

$$\frac{\mathrm{d}\,\sigma}{\mathrm{d}\,\Omega}(\theta) = \frac{\mathrm{d}\,\sigma}{\mathrm{d}\,\Omega}(180^\circ - \theta) \tag{2.14}$$

As a consequence, an experimental setup featuring two detectors at the forward or backward angles θ_i specified in table 2.1 can be used for an angular integration using Gaussian quadrature of order N = 4. The integration results are correct for differential cross section expressions up to order M = 2N-1 = 7 and thus for multipolarities L $\leq$ 3. The final total cross section for this configuration is then given by:

$$\sigma_{tot} \approx 2 \cdot 2\pi \left[w_1^* \frac{\mathrm{d}\,\sigma}{\mathrm{d}\,\Omega}(\theta_1^*) + w_2^* \frac{\mathrm{d}\,\sigma}{\mathrm{d}\,\Omega}(\theta_2^*) \right] \tag{2.15}$$

with $\theta_1^* = (30.6^\circ \text{ or } 149.4^\circ)$, $\theta_2^* = (70.1^\circ \text{ or } 109.9^\circ)$, $w_1^* = 0.3479$ and $w_2^* = 0.6521$. Note the additional factor 2 with respect to equation (2.12), due to the fact that only two out of the four angles are measured.

2.1.4.3 Internal Conversion

Internal conversion is a process competing with γ decay in excited nuclei. In fact, the transition from an excited level to a lower level can take place without emission of a photon: the energy of the transition can directly be transferred to an electron of the atom, which is then ejected. The ratio of decay rates due to internal conversion and γ emission is defined as the *internal conversion coefficient* α_{IC}:

$$\alpha_{IC} = \frac{\lambda_e}{\lambda_\gamma} \tag{2.16}$$

This factor increases rapidly with the nuclear charge Z and the multipolarity L, and decreases with increasing energy difference between the decaying state and the lower energy state. It also varies strongly with the nature of the transition (electric or magnetic) [3]. For the ^{232}Th isotope for example the value ranges between $\alpha_{IC} = 327$ at $E_\gamma = 49.63$ keV and $\alpha_{IC} = 0.44$ for the $E_\gamma = 223.6$ keV transitions studied in this work.

Different model approximations for these coefficients exist. The ones used in this work correspond to the Band-Raman conversion tables, recommended by the National Nuclear Data Center (NNDC) [8].

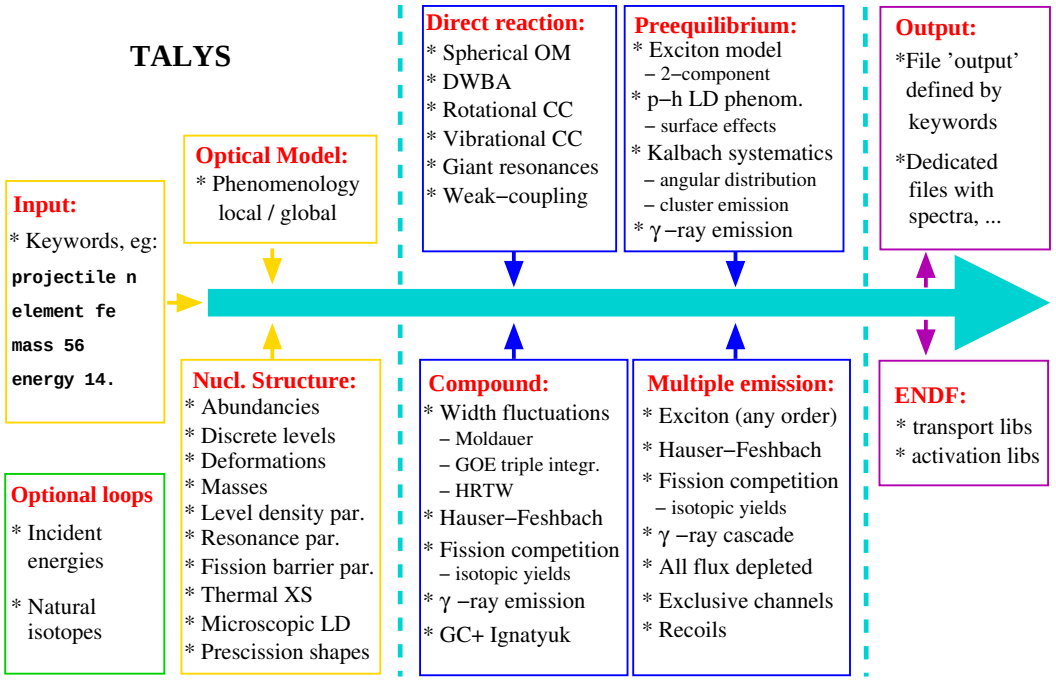

Figure 2.4: Schematical description of the TALYS code [9].

2.1.5 Model calculations with TALYS

With the reaction mechanisms and decay possibilities of excited nuclei presented above, all the ingredients are given to modelize the different reactions. There exist several codes using different models to achieve this, such as GNASH and TALYS. The model comparison in this work is made with respect to the TALYS code.

TALYS is a nuclear reaction program, providing complete simulations of nuclear reactions involving neutrons, protons, photons, deuterons, tritons, ^{3}He and α particles in the energy range of 1 keV to 200 MeV for target nuclei of mass A $\geq$ 12 [9]. Its goal is to predict nuclear reactions using theoretical codes where no or just partial experimental data is available. This is achieved by assuming that total reaction cross sections can be expressed as a series of binary reactions, for which parameters as particle or γ emissions are computed respecting the conservation laws for energy, spin and parity.

A schematical description of the TALYS code is shown in figure 2.4. The calculations made are based on the optical model, for which an extensive library featuring isotope properties, such as level densities and fission barrier parameters, is mandatory. The models used by TALYS depend on the reaction mechanisms of direct, pre-equilibrium and compound nucleus reactions which were presented in section 2.1.2.

After emission of a particle, the binary reaction is finished, but not the entire process. The resulting residual nuclei formed in the first step can be subject to further reactions,

especially at higher energies. For this reason it is of uppermost importance to include a complete library set of all the parameters of the nuclei in the decay chain. This is particularly important for the fission cross sections of fissionable isotopes.

As these parameters are not included in TALYS by default, the computations in this work were realised by Pascal Romain from the *Commissariat à l'énergie atomique (CEA), Bruyères-le-Châtel, France*, which is in possession of well fitted fission cross sections for ^{235}U and by Arjan Koning, one of the authors of the TALYS code from the *Nuclear Research and Consultancy Group (NRG), Petten, The Netherlands* for the ^{232}Th cross sections.

2.2 The different measurement techniques

After the theoretical study of the reactions performed in this work, this section is dedicated to the different techniques that can be adopted to measure the reactions. In fact, the measurement of (n,xn) reactions may be accomplished in three different manners: Measurement by activation, by secondary neutrons or using prompt γ-ray spectroscopy.

Depending on the reactions and isotopes of interest, different techniques can be used. In this section the mentioned methods will be presented, with a special emphasis on the prompt γ-ray spectroscopy, which is used for the experiments in this work.

2.2.1 Activation

The method of activation consists of two different steps: in a first time, the studied sample is irradiated using a monoenergetic neutron beam. Occurring reactions will lead to unstable isotopes or metastable states of the remaining nuclei. In a second phase the sample is analysed off beam. The produced isotopes will decay via α, β and γ emissions, which can be measured using for example γ spectroscopy. This method has been applied for inter alia ^{232}Th(n,2n)^{231}Th reaction cross sections by P. Raics et al [10] and D. Karamanis et al [11].

The advantage of this method is that it gives direct access to the total (n,xn) reaction cross sections. Furthermore it is not destructive, which is especially interesting for archaeological measurements.

The inconvenience is that the irradiation and measurement time have to be of the same length as the half life of the produced isotopes. Short-lived isotopes will decay too quickly, before the measurement can be performed, whereas long-lived nuclei will need very long experimental runs. Another disadvantage of this technique is that different reactions on different isotopes can produce the same nucleus. For example a (n,γ) reaction on an isotope of atomic mass number A = x and a (n,2n) reaction on an isotope of mass number A = x+2, will both yield an isotope of atomic mass number A = x+1. Highly enriched samples are mandatory for this type of measurements.

2.2.2 Secondary neutron measurements

The most straightforward way to measure (n,xn) reactions is to measure the neutrons resulting from these reactions directly. For this method, an online setup must be used. The measurement can be performed by bombarding a sample with a neutron beam and

positioning different neutron sensitive detectors (such as for example plastic or liquid scintillators) around the target. Measurements using this technique have been made among others on ^{235}U(n,2n)^{234}U cross sections by J. Frehaut et al. [12, 13] or, more recently, on (n,xn) reactions of bismuth and tantalum by X. Ledoux et al. [14].

The benefit of this technique is that it is unnecessary to use codes predicting the different excitation level branching ratios to compute the total cross section.

Nevertheless, this procedure presents some major inconveniences: the angular distribution of the neutrons depends strongly on the reaction mechanism. As the latter depends on the incident neutron energy, precise knowledge of the mechanism as well as a detailed angular distribution study at a monoenergetic beam are necessary.

Furthermore it is not straightforward to distinguish between neutrons coming from inelastic scattering or (n,2n) reactions in the overlapping region. The situation is even more complicated for fissionable isotopes, for which additional neutrons are produced due to neutron induced fission.

2.2.3 Prompt γ-ray spectroscopy

This measurement method consists of bombarding a sample with a unidirectional neutron beam and measuring the emitted γ radiation accompanying by the neutron emission in (n,xn) reactions. The technique has been first used at the Los Alamos National Laboratory, where (n,xnγ) reactions on ^{207,208}Pb [15] and later also on other isotopes as e.g. ^{239}Pu [16] were probed.

The particular interest of this method is that it is not limited to monoenergetic beams, but can be extended to so-called *pulsed white beams*. Using the time-of-flight technique (see experimental setup section 3.1.4 for more details), one can determine the energy of the incident neutrons and perform the measurements for a large domain of energy and several reaction channels simultaneously. Using detectors presenting a high energy resolution is essential to be able to differentiate between several energy peaks, especially in the case of radioactive samples.

Limitations of this technique can appear when there exist intermediate isomeric states in the decay of the excited nuclei. In this case the deexciting γ emission may be retarded and is not correlated to the correct neutron energy anymore. Another disadvantage can be caused due to the *Doppler effect* [1]. In fact, at high neutron energies, the emission of the γ ray may be influenced by a recoiling target nucleus. In that case, the energy resolution is affected, as the measured γ energy is not equal to the emitted energy. However, this phenomenon can be neglected when probing heavy nuclei, for which the nucleus recoil is much smaller.

The downside of these measurements is that they do not give direct access to the total (n,xn) cross section, but only to the deexcitation spectra of characteristic γ levels. The total cross section is then obtained using theoretical codes, such as for example TALYS, on the acquired data.

On the other side however this method does not only enable us to determine (n,xn) reaction cross sections but also to verify the existing codes and their parametrisation (as e.g. nuclear level densities or branching ratios). The γ level information deduced from the measurements can be used to obtain new data on the structure of the isotopes of interest

and thus contribute to a better understanding of the fundamental physics and to enhance theoretical models.

Bibliography

[1] K.S. Krane, *Introductory Nuclear Physics*, John Wiley & Sons, New York, 1987

[2] R.D. Evans, *The Atomic Nucleus*, McGraw-Hill Book Company, Inc., New York, 1955

[3] P.E. Hodgson, E. Gadioli, E. Gadioli Erba, *Introductory Nuclear Physics*, Clarendon Press, Oxford, 1997

[4] V.F. Weisskopf, *Radiative Transition Probabilities in Nuclei*, Physical Review **83** (1951), 1073

[5] C.R. Brune, *Gaussian quadrature applied to experimental γ-ray yields*, Nuclear Instruments and Methods in Physics Research **A493** (2002), 106-110

[6] L.C. Mihailescu, *Neutron (n,xnγ) cross-section measurements for ^{52}Cr, ^{209}Bi and $^{206,207,208}Pb$ from threshold up to 20 MeV*, Ph.D. thesis, University of Bucharest, 2005

[7] K.F. Riley, M.P. Hobson, S.J. Bence, *Mathematical Methods for Physics and Engineering*, Second Edition, Cambridge University Press, 2004

[8] NNDC, National Nuclear Data Center, http://www.nndc.bnl.gov/

[9] A.J. Koning, S. Hilaire and M.C. Duijvestijn, "TALYS-1.0", *Proceedings of the International Conference on Nuclear Data for Science and Technology*, April 22-27, 2007, Nice, France, editors O.Bersillon, F.Gunsing, E.Bauge, R.Jacqmin, and S.Leray, EDP Sciences, 2008, p. 211-214

[10] P. Raics, S. Daróczy, J. Csikai, *Measurement of the cross sections for the $^{232}Th(n,2n)^{231}Th$ reaction in the 6.745 to 10.450 MeV energy range*, Physical Review **C32** (1985), 87-91

[11] D. Karamanis, S. Andriamonje, P.A. Assimakopoulos, G. Doukellis, D.A. Karademos, A. Karydas, M. Kokkoris, S. Kossionides, N.G. Nicolis, C. Papachristodoulou, C.T. Papadopoulos, N. Patronis, P. Pavlopoulos, G. Perdikakis, R. Vlastou, The n-TOF Collaboration, *Neutron cross-section measurements in the Th-U cycle by the activation method*, Nuclear Instruments and Methods in Physics Research **A505** (2003), 381-384

[12] J. Frehaut, A. Bertin, R. Bois, *Measurement of the ^{235}U(n,2n) cross section between threshold and 13 MeV*, Nuclear Science and Engineering **74** (1980), 29-33

[13] J. Frehaut, *Use of the large Gadolinium-loaded liquid scintillator technique for (n,2n) and (n,3n) cross section measurements*, Nuclear Instruments and Methods **135** (1976), 511-518

[14] X. Ledoux, I. Lantuéjoul, N. Arnal, J.M. Laborie, J.P. Lochard, P. Pras, C. Varignon, *An improved experimental set-up for (n,xn) reaction studies*, Proceedings of the 2006 International Workshop on Fast Neutron Detectors and Applications, online: http://pos.sissa.it.

[15] H. Vonach, A. Pavlik, M.B. Chadwick, R.C. Haight, R.O. Nelson, S.A. Wender, P.G. Young, *$^{207,208}Pb$(n,xnγ) reactions for neutron energies from 3 to 200 MeV*, Physical Review **C50** (1994), 1952-1963

[16] L.A. Bernstein et al, *^{239}Pu(n,2n)^{238}Pu cross section deduced using a combination of experiment and theory*, Physical Review **C65** (2002), 1952-1963

Chapter 3

Experimental Setup

This chapter presents the experimental setup that was used for the (n,xnγ) reaction cross section measurements in this work. In the first section the neutron production facility GELINA[1] of the Institute for Reference Measurements and Materials (IRMM) in Geel, Belgium along with its characteristics is presented while the second part of this chapter is dedicated to the actual experimental setup, where the reactions of interest are generated and detected.

3.1 The GELINA neutron time-of-flight facility

For the experiments in this work, the neutron beam of GELINA was used. In fact, this facility produces a white, pulsed neutron beam with energies ranging from 1 meV to 20 MeV at a unique time resolution and is best suited for the measurements of our interest.

The GELINA facility consists of four distinct units: a pulsed linear electron accelerator, a beam compression magnet, a uranium target and different flight paths. A schematical overview of these are given in figure 3.1. A detailed description for each of these elements is presented in the following sections [1, 2].

3.1.1 Pulsed linear accelerator

The backbone of the GELINA facility is the electron accelerator. Here a pulsed electron beam of a duration of 10 ns and a very high peak current of 12 A is injected by a triode gun. In the accelerating part these highly charged pulses are travelling along synchronously with an electromagnetic wave which is introduced into the accelerator sections for each pulse by three high power klystrons. The maximum repetition rate of the klystrons is 800 Hz and thus defines the maximum frequency of the finally generated neutron beam.

The energy of the accelerated electrons varies linearly from 140 MeV down to 70 MeV. Indeed, this is due to the fact that the first electrons are speeded up by the full power of the electric field inside the accelerator cavities. Through the passing of the electron bunch, the field is weakened. Since the pulse is very short the klystrons cannot replenish the cavities fast enough to compensate for this power loss. As a consequence the following

[1] GELINA: GEel LINear Accelerator

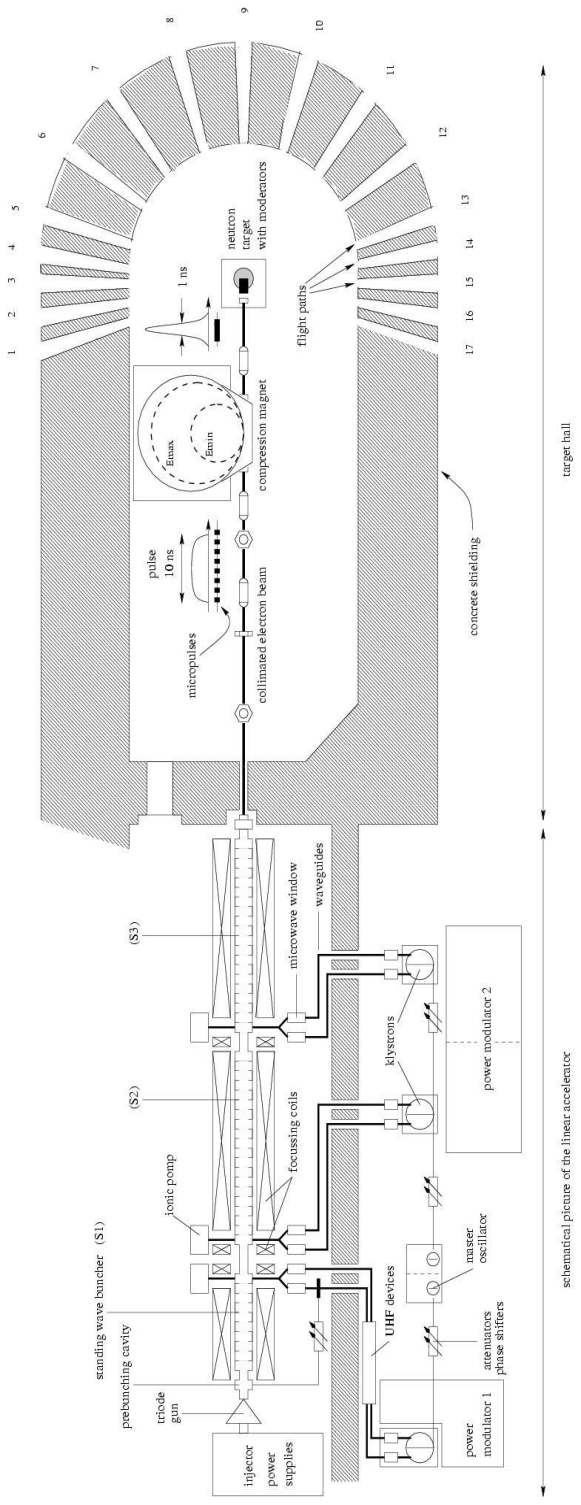

Figure 3.1: Overview of the different units of the GELINA accelerator.

electrons suffer from a weaker electromagnetic field, due to their forerunners, and only reach energies of around 70 MeV.

3.1.2 Compression magnet

At the exit of the LINAC the beam has a pulse width of 10 ns with electron energies ranging from 70 to 140 MeV. As time resolution is a key issue in the cross section measurements it is very important to furtherly reduce the pulse duration. This is done in the compression magnet, which physically corresponds to a 50 tons circular magnet with a diameter of 3 m.

After acceleration in the LINAC, the electron bunches will take a loop in the compression magnet. As the bending radius of an electron in a magnet is proportional to its energy and as their speed is very close to the velocity of light, the high energy electrons will follow a longer circular trajectory than the slower ones. Hereby, the fast electrons will be delayed with respect to the slower ones thus reducing the duration of the pulse.

The magnet is designed in a way that all electrons in a 10 ns pulse will leave in a 1 ns pulse. As this compression is charge conserving, the peak current rises from 12 to 120 A.

3.1.3 Neutron production

The 1 ns short electron beam emerging from the compression magnet will now hit a neutron producing target. This target is made from an uranium-molybdenum alloy, with depleted uranium and 10wt% Mo. It is cooled by liquid mercury, to avoid neutron moderation, and sealed in stainless steal. As the target has to dissipate the entire power of the electron beam (of the order of 10 kW) it is rotating perpendicularly to the beam axis, so that the impact location varies from pulse to pulse.

In the target, the electrons are decelerated by the high density of the U-Mo alloy and thus produce high-energy photons via the *Bremsstrahlung* process. The latter ones may then interact with the target nuclei and produce neutrons via (γ,xn) and to a lesser extent via (γ,f) reactions. Uranium gives the best neutron production rate: for 100 electrons of 100 MeV roughly 6 neutrons are emitted from the target. On average the produced neutron intensity is $3.4 \cdot 10^{13}$ neutrons per second.

The rotating uranium target is surrounded to one side by a water filled beryllium tank. This one is used to moderate the neutrons coming from the target, and thus optimising the neutron flux for energies below 100 keV. For our experiments the neutrons are coming directly from the target and are optimised for energies above 100 keV. The observed neutron flux yield is a *white* spectrum, i.e. containing neutrons of a large domain in energy, resulting from combined evaporation and fission reactions.

3.1.4 Measurement stations and the time-of-flight technique

The neutrons produced in the rotating uranium target are collimated into 17 different flight paths installed in a star-like configuration around the source. The flight tubes are kept under vacuum to prevent from flux attenuation and scattering. The neutron collimation can be adjusted to obtain a desired beam diameter and the flux can be filtered to get an optimised neutron energy spectrum.

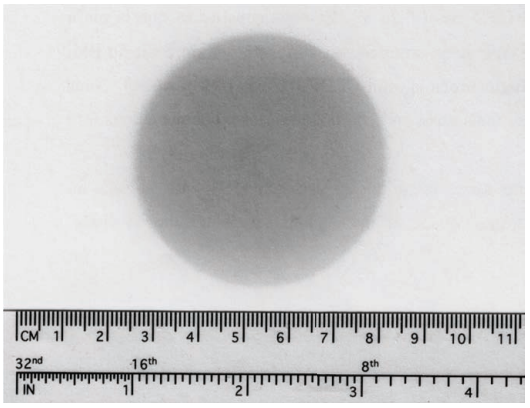

Figure 3.2: Beam section at the sample position for the FP16 flight path obtained with a γ sensitive film.

The measurements presented in this work take place in a station on flight path FP16. For this flight path, the beam is collimated to have a diameter of 55 mm at the measurement point. Figure 3.2 shows the section of the beam which has been obtained introducing a γ sensitive film into the beam. Indeed, the γ radiation created in the rotating neutron source is travelling along with the neutrons on the different beam lines. The diameter of the beam measured with the use of these high energetic photons thus reflects the section of the neutron beam.

The beam line of FP16 also holds two types of filters. The first type consists of ^{10}B and is used to cut out thermal neutrons. Indeed, for a high neutron frequency (the experiment is realised at a burst rate of 800 Hz) slow and thermal neutrons from one burst will overlap with the fast neutrons from the following pulse. As the experiments are focused on fast neutrons, a boron filter absorbs thermal and slow neutrons in order to select the desired energy domain and eliminate neutrons from previous bursts.

A second type of filter is made of depleted uranium. Its role is mainly to attenuate the γ flash, i.e. remaining γ radiation which was created in the rotating neutron source and which is accompanying the neutrons. As this γ flash is very intense it is important to be weakened as much as possible to prevent high dead time on the data acquisition. The collimation scheme of the used flight path is given in figure 3.3.

At the different measurement stations, the neutron energy can be determined by the time-of-flight technique. Indeed, the neutron energy E_n is related to its speed by the relativistic formula

$$E_n = (\gamma - 1)m_n c^2 \tag{3.1}$$

where m_n is the neutron mass and γ is the Lorentz factor expressed as

$$\gamma = \sqrt{\frac{1}{1 - \frac{v^2}{c^2}}} \tag{3.2}$$

with c the velocity of light and $v = \frac{d}{t}$ the neutron speed, thus the quotient between the travelled distance d and the elapsed time t.

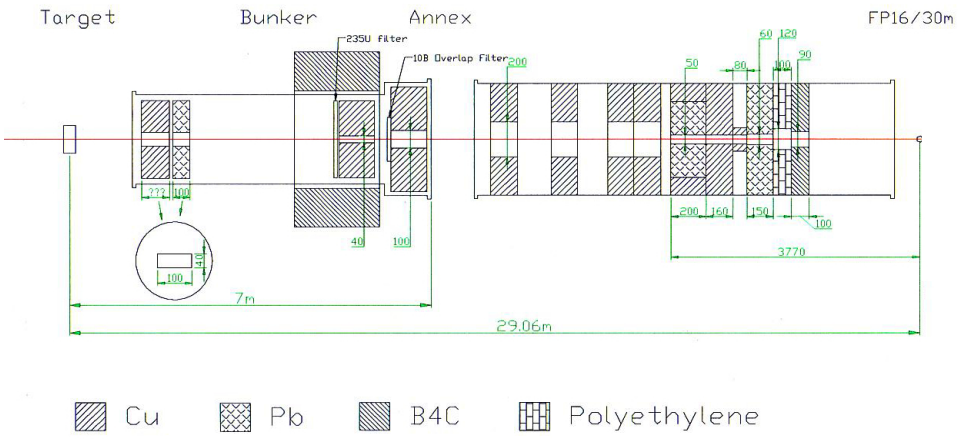

Figure 3.3: Collimation of the beam of flight path 16 used for the experiments in this work.

Knowing the exact source distance at which the experiments are performed, this method enables us to compute the neutron energy by measuring their flight time. To achieve this the reference time t_0, at which the electrons hit the rotating uranium target, is provided to the different stations.

At GELINA the measurement stations are located at distances between 8 up to 400 m from the neutron source. The choice of the best source distance is a compromise between the desired neutron energy resolution and flux intensity.

3.2 Experimental Setup

In this section the actual experimental setup, especially designed for the measurements in question, shown in figure 3.4, is presented. The choice of the flight distance is discussed along with the generation of (n,xn) reactions and their detection. A special emphasis is made on the noise reduction, which was a constant issue kept in mind while conceiving the setup.

3.2.1 Flight distance for radioactive sample measurements

Before building an experimental setup, the right flight distance has to be chosen. As already mentioned earlier, the flux intensity as well as the energy resolution depend on the source distance. When approaching the neutron source the solid angle increases squared, and thus the incident neutron flux is much higher. On the other side, the neutron bunches are shorter, i.e. the slower neutrons follow shortly after the fast ones, unlike at larger distances where the time distribution of the pulses is larger. For a given data acquisition system, it will be possible to get a better time-of-flight and hence neutron energy resolution at higher source distances as the time separation is larger here.

In our case we are measuring radioactive samples of rather high density with $\rho >$

Figure 3.4: Picture of the experimental setup showing the lead shielding as well as the different HPGe detectors on the table in the left and the data acquisition system in the right.

10 $\frac{g}{cm^3}$. For this purpose it is preferable to use thin samples for two reasons: Thick samples at this density would strongly absorb emitted γ rays which are to be detected and hence lead to an important correction factor due to auto-absorption inside the target. Another problem of the radioactive samples is their background. The higher the mass of the sample, the more activity is emitted, creating dead time on the detectors. The thicknesses of the samples used in this experiment are of the order of several hundred micrometres, thus presenting a density of several hundred milligrams per square centimeter.

When using thin samples, a higher incident neutron flux is necessary to compensate for the sample mass reduction, as the reaction rate depends on both of these factors. For this reason the experiment is performed at a measurement station located 30 m from the neutron source, where the exact sample distance is (28.817 $\pm$ 0.001) m. A 10 ns time resolution on the data acquisition allows a neutron energy resolution of 0.86 MeV at 20 MeV and 0.3 keV at 100 keV.

3.2.2 γ generation and detection

A schematical view of the experiment is shown in figure 3.5. A thin sample with a diameter larger than the beam section, highly enriched in isotopes of interest is exposed to the neutron beam of GELINA. The neutrons in the sample will induce inter alia (n,xn) reactions and leave the resulting products of these reactions in excited states, which will decay through the emission of γ radiation.

Around the sample, four semi-planar High Purity Germanium (HPGe) detectors referred to as grey, green, red and blue are installed at the angles of 110° and 149° as discussed previously (cf. section 2.1.4.2). The detector to sample distances are shown in figure 3.5. For this experiment backward angles were chosen. Indeed they observe the

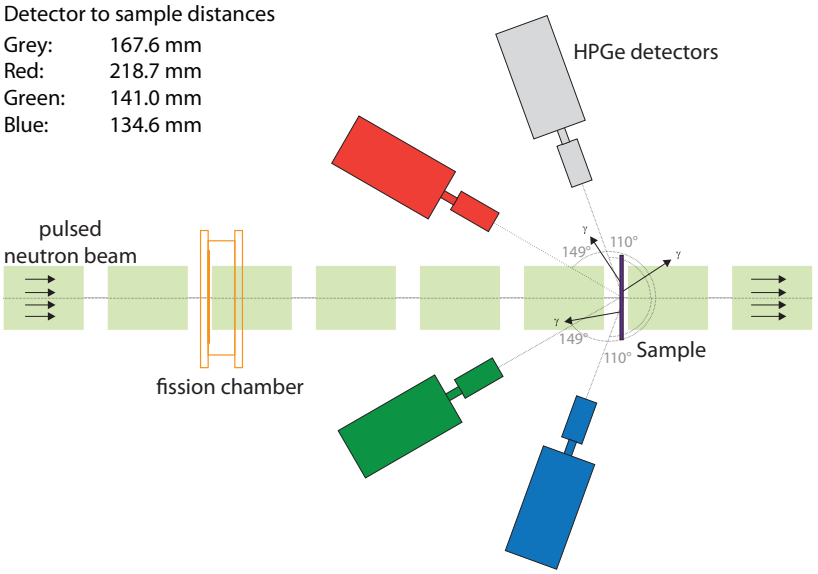

Figure 3.5: Schematical overview of the experimental setup.

same γ distribution as forward angles, but suffer from less scattering of the γ flash and thus from less background noise.

The properties and the efficiency of these detectors are discussed in section 4.2, where the exact specifications of the counters are given.

The HPGe detectors are used with a digital data acquisition system shown in the right part of figure 3.4 and described in more detail later. With this system list mode files are generated, i.e. γ-ray amplitudes and timestamp information are saved at the same time. Subtracting a reference time provided for each pulse by the accelerator from the timestamp of each event gives a non-calibrated time-of-flight spectrum. An example of such time-of-flight and energy spectra, generated by the acquisition system during the measurement campaign of the ^{235}U isotope is shown in figure 3.6.

In the time-of-flight spectrum one can observe a constant counting plateau with a large peak followed by a hump. The constant contribution is caused by the detection of the sample radioactivity, and gives thus rise to a permanent counting. The large peak is the so-called γ flash, already mentioned earlier. It is caused by the scattering of γ rays issued from the primary neutron target and has conveniences as well as downsides. The major inconvenience is the dead time caused by the detection of these γ rays. Indeed, as one can clearly observe in figure 3.6(a), the counting rate peaks to 10^7 and is responsible for a dead time rate going up to 60% depending on the detector. The benefit of the flash is however that it allows us to precisely calibrate the time spectrum. Indeed, as the γ rays are created at the same time than the neutrons, and knowing the exact distance of the experimental setup to the neutron source, we can calibrate the reference time t_0 at which the neutrons are born. Setting $t_0 = 0$, the γ flash travelling the source-sample distance

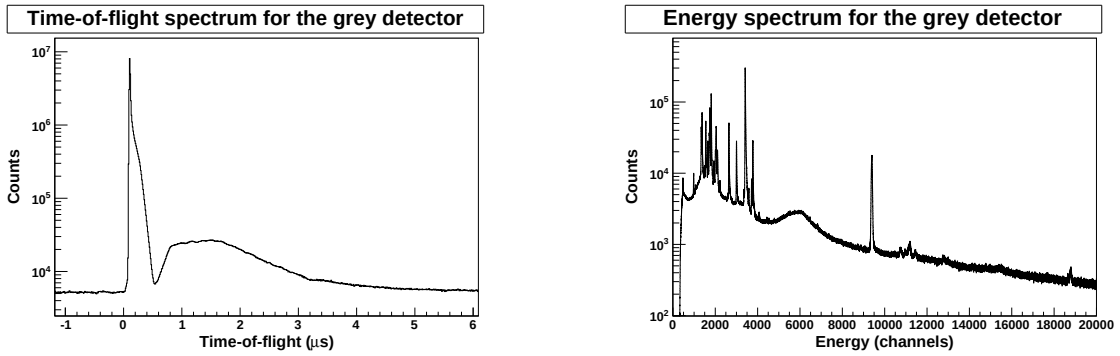

(a) (b)

Figure 3.6: Time-of-flight (a) and energy (b) spectra for the grey detector acquired with a ^{235}U sample.

$d = 28.817$ m at the speed of light c, is arriving at the sample position at:

$$t_\gamma = \frac{d}{c} = 96.06 \text{ ns} \tag{3.3}$$

The hump following this γ production is due to neutron induced events. Once the time-of-flight spectrum is calibrated as described above, it can be gated on the neutron hump, thus selecting well defined neutron energy ranges by applying equation (3.1). For these, energy spectra can be generated in order to extract the information on the studied reactions.

Such an energy spectrum is shown in figure 3.6(b), for which a neutron energy range of 100 keV to 20 MeV has been selected. The major part of the rays observable here are due to radioactivity γ emissions. Knowing the energy values of the radioactive decay of the sample, the spectrum can be calibrated. In this spectrum one can find the different deexcitation rays of the reactions of interest. Counting the number of hits in these rays, the total cross section of a reaction can be computed, as discussed in section 5.1.2.

3.2.3 Noise reduction

The amount of γ rays of interest observable in the spectra is rather low, therefore it is important to reduce the radioactivity counting to a minimum in order to be able to extract the rays of interest satisfactorily. Indeed, a strong background noise causes a large error when extracting rays of interest and leads thus to a large uncertainty on the final cross section quantities. Factors influencing the data extraction are the natural radioactivity of the sample, counting of events due to the γ flash, the ambient background due to scattering of the γ flash in other experiments as well as electromagnetic noise from the accelerator. In the following sections two of the sources of such background noises, for which a significant care was taken, are elaborated.

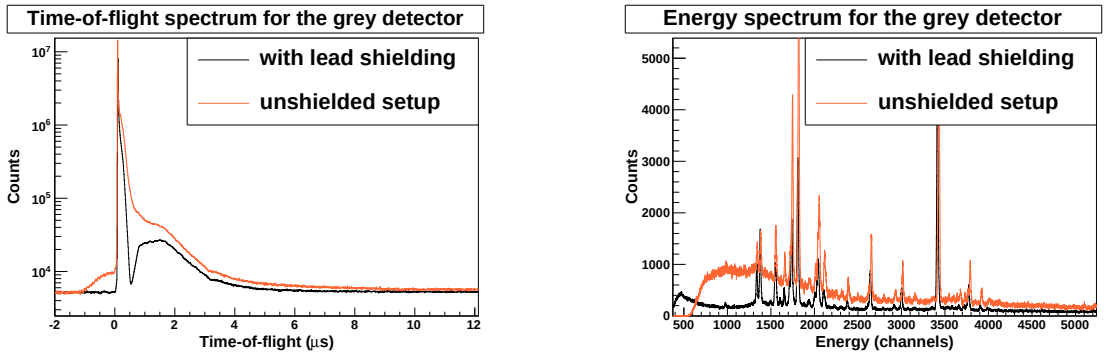

(a) (b)

Figure 3.7: Time-of-flight (a) and energy (b) spectra for the grey detector acquired with a ^{235}U sample. The red contributions were obtained without shielding, the black ones with a specially designed lead castle.

3.2.3.1 γ background

One source of background detections are scattered γ rays. As already observed, the γ flash of the GELINA facility is very strong. This radiation is impinging on all the experimental setups situated all around the accelerator and a certain portion is thus scattered back onto the other flight paths of the installation. As this background is caused by backscattering it does not arrive at the same time than the direct γ flash compound but a little later and is thus overlapping in time with the neutrons. A resulting time-of-flight and neutron gated energy spectrum obtained with a ^{235}U sample for the grey detector is shown in figure 3.7 in red.

To eliminate this background radiation, a special lead shielding was designed. Test measurements showed that the radiation is not coming from one single direction, but is rather distributed isotropically around the entire setup, including bottom and top directions. As the detectors are of different size and positioned at well defined angles a dedicated construction was built at the IPHC workshop with a shielding designed to encase all the sensitive detector parts as well as the studied sample. It is made of single lead bricks which can be taken off manually in order to modify the arrangement of the detectors. The base is made of 50 mm thick bricks, the vertical surfaces surrounding the setup consist of bricks of 25 mm thickness and the top can be closed with 3 layers of 10 mm lead plates. A 3D drawing of this lead castle is shown in figure 3.8.

Comparing the unshielded spectra in figure 3.7 (in red) with the ones obtained with the new lead construction (in black) one can clearly observe the benefits of this work. In the time-of-flight spectra we managed to separate the γ flash almost completely from the neutron hump and the energy spectra show a strongly reduced Compton scattering in the low energy domain. This shielding enables us to better measure low energy transitions with low statistics as their background is much weaker, and hence also the error on its subtraction.

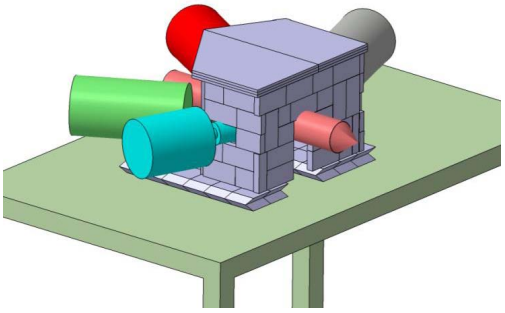

Figure 3.8: 3D drawing of the lead shield designed for the experimental setup showing the four HPGe detectors. The pink cone represents the materialisation of the neutron beam.

3.2.3.2 Electromagnetic compatibility

A second type of background is due to an electromagnetic field generated by the accelerator. In fact, the highly powerful klystrons injecting the electromagnetic waves into the linear electron accelerator emit a very strong field which is captured by the cables of the setup. As this noise is very close to the γ flash, it arrives with the neutron bursts and may thus generate a signal distortion which is superimposed with pulses of interest detected on the germanium detectors. For this reason, only well isolated coaxial cables developed initially for the Euroball experiment equipped with a triple shielding in conjunction with ferrites filtering these high frequency amplitudes were used for the setup. The different connections as well as the cables are wrapped in aluminium foil to be shielded from the electromagnetic field and are attached to the table of the setup to be closest to the ground plane to avoid additional amplifications of these signals.

Furthermore this electromagnetic field does not only interfere with the signals of the setup itself, but is also transported by the electric circuit of the entire facility. For this reason all the instruments were connected to an isolation transformer, filtering out the noise signals coming from the klystrons [3].

The effect of these noises is shown in figure 3.9(a). This is the reference t_0 pulse given by the accelerator for each neutron burst. When zooming on the low amplitudes, one can observe the interferences caused by the electromagnetic noise. If such a noise is superimposed with a signal from the detector, the time-of-flight spectra can be crucially deteriorated as shows the comparison of figures 3.6(a) and 3.9(b). Indeed, the time information cannot be read correctly in such a scenario as the amplitude of the electromagnetic signal interferes on the triggering of the data acquisition.

3.2.4 Incident neutron flux measurements

In order to measure reaction cross sections, it is evident that one must determine the neutron flux delivered by the accelerator, and thus the number of neutrons impinging on the sample of the experimental setup. This is realised with a fission chamber featuring two highly enriched uranium deposits. Details on the operation of the fission chamber is

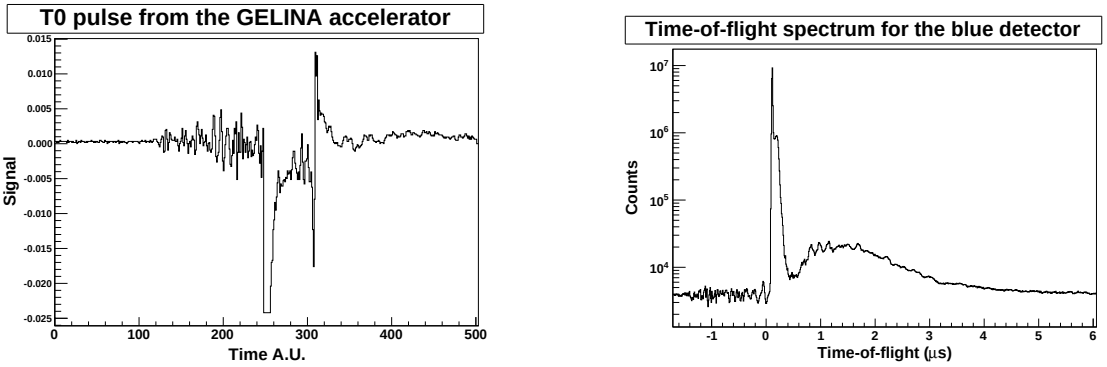

(a) (b)

Figure 3.9: t_0 pulse coming from the accelerator announcing a neutron burst (a) and a time-of-flight spectrum for which an electromagnetic noise occurred.

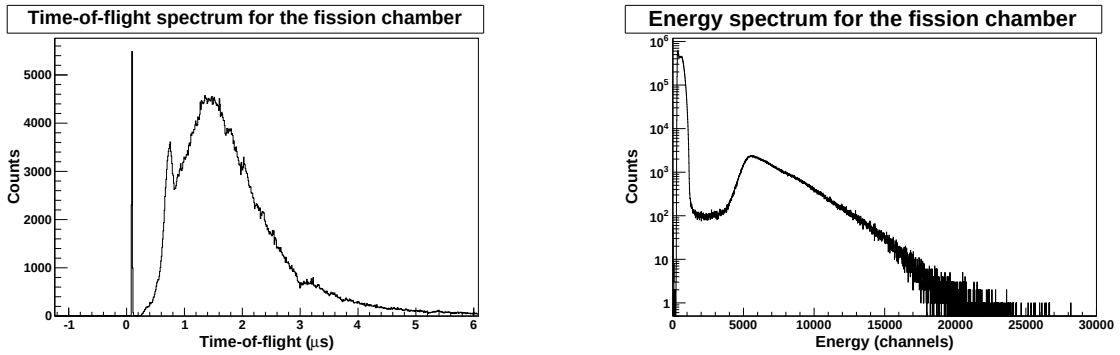

(a) (b)

Figure 3.10: Time-of-flight (a) and energy (b) spectra for the UF_4 deposit of the most recent configuration of the fission chamber shown in figure 4.1 acquired with a ^{235}U sample.

discussed extensively together with its efficiency in chapter 4.

The fission chamber is located at a flight distance of 27.260 m and is connected to the same data acquisition system than the germanium detectors and the same type of list mode files with energy and time information is stored. An example of the shape of the energy and time-of-flight spectra is presented in figure 3.10. For the left spectrum, the α background counting was subtracted for a better illustration.

The time-of-flight spectrum in figure 3.10(a) shows a first peak which is due to fissions induced in the deposits of the ionisation chamber by (γ,f) reactions, followed by neutron induced fission events. Structures in the latter one are due to the shape of the neutron induced fission cross section of the uranium sample. The spectrum can be calibrated similarly than the ones of the HPGe detectors explained above. It is noteworthy to mention that the main cause of background in this case is not due to the γ flash, but due to the radioactivity of the uranium foils of the fission chamber.

This can be illustrated by having a closer look at the energy spectrum in figure 3.10(b).

A first contribution at low energy can be attributed to the α activity of the deposits, while the second contribution is due to fission products. As the separation of both contributions is very delicate, a detailed discussion on this topic is following in chapter 4.

As the neutron flux intensity may vary from week to week, it is important to measure the neutron flux continuously. For this reason the fission chamber is operated together with the germanium detectors and the flux is computed separately for each data set.

In the following chapter more details about the detection properties of the fission chamber and its efficiency will be discussed. The results of a typical flux calculation are presented in chapter 5 along with the studied cross section results.

3.2.5 Data acquisition

The data acquisition in this experiment is performed thanks to digital TNT2[2] cards developed at IPHC [4]. The digital treatment unifies all the different analogical modules on one card, where treating algorithms are executed via a Field Programmable Gate Array (FPGA) which has a sampling rate of 100 MHz, allowing a time resolution of 10 ns and encoding the energy information on 14 bits.

The signals issued from the preamplifier are directly treated by the acquisition cards. The pulses present a rising part corresponding to the collection time of the created ionisation inside the crystal which is then accumulated on a capacitor integrated in the preamplifier. The discharge of the latter one can be compared to a simple RC circuit and is thus creating an exponential signal decay [5]. This signal is then treated in parallel in two individual channels:

- the so-called time channel, determining the time of the event
- the so-called energy channel, determining the energy of the pulse

the algorithms of these channels will be discussed in the following sections. A schematical illustration of the operation mode of the card is given in figure 3.11.

3.2.5.1 Time determination

In order to extract time information on the preamplifier signal, it is first processed using a Timing Filter Amplifier (TFA). The initial pulse is differentiated then integrated to discard noise effects, which creates a signal of symmetrical shape.

The TFA signal will then be handled by a Constant Fraction Discriminator (CFD). In this algorithm the signal is duplicated and the first copy is inverted and attenuated while the second one is delayed. Both of these compounds are then superimposed, and the timing is taken at the zero value of the constructed pulse. The benefits of this way to process the signal is that the timing result does not depend on the amplitude of the initial signal.

As electronic noise can cause multiple zero values of the final signal, a window is defined by applying a threshold on the TFA signal as shown in figure 3.11. This one is then used to gate the zero value of the CFD signal.

[2]TNT: Treatment for Numerical Tracking or Treatment for NTof

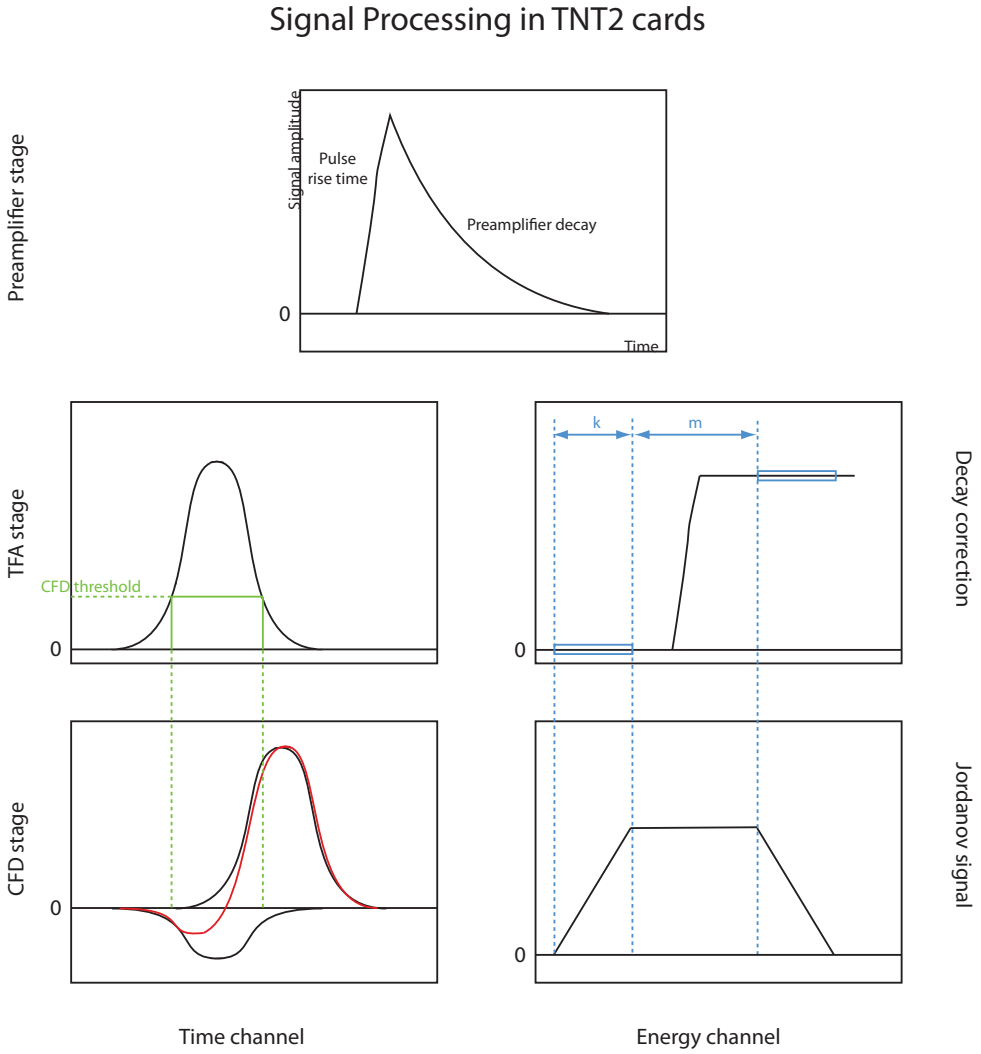

Figure 3.11: Schematical illustration of the signal processing with TNT2 cards. For explanations see text.

3.2.5.2 Energy determination

In order to compute the energy of the pulses detected, the Jordanov [6] algorithm is applied. To achieve this, the signal is first corrected for its exponential decay. As the decay constant $\tau = RC$ only depends on the internal resistor and capacitor of the preamplifier it is determined once and is independent of the detected energy. The signal is then multiplied by $e^{t/\tau}$, and a flat top is obtained as shown in figure 3.11.

The next step consists of defining two windows of width k, delayed by a time m, moving along the signal. Inside the windows the signal mean value is calculated and the final Jordanov signal is obtained by subtraction of the two mean values. Its shape is trapezoidal with a rise time k and a plateau of size m.

The energy of the event is then determined at the end of the plateau. The energy extraction of the signal takes thus a certain time $k+m$ defined by the choice of parameters. For the detectors used in the experimental campaign presented in this work, the energy and time resolution was found optimal for $k = 3$ μs and $m = 1$ μs.

The benefits of this technique is that it is very well adapted to online signal treatment. Computing mean values with moving windows cuts out possible noise on the signals and the multiplication by the decay constant corrects the signal for ballistic deficit, i.e. amplitudes depending on the rise time of the signal. Indeed, depending on the location of detection the collection of the charge may take longer and through the discharge of the capacitor the signal may vary in amplitude. This is however avoided by this technique.

3.2.5.3 Dead time treatment

A very important aspect of data acquisition systems is the precise knowledge of the dead time. As the TNT2 cards work on two parallel channels, we distinguish here between real dead time and so-called pile-up events.

When two events are occurring in a very short time, the generated TFA signal on the time channel cannot determine a difference between the signals. In this case the construction of the CFD signal has only one zero value in the destined gate and there will hence just be one single time information extraction. The analysed signal corresponds then to the overlay of both events. This can be compared to the dead time with classical acquisition systems.

As the time channel, which takes around 0.3-0.4 μs, is generally much faster than the energy channel, a second type of dead time is created. As already mentioned above, the dead time of the energy channel can be attributed to the time needed to extract the energy information from the signal, in our case this time corresponds to $k + m = 4$ μs. When the time channel announces a second event before the previous one has been treated completely, the energy of neither of the pulses can be determined properly. The event is then tagged as a pile-up and only the time information of both events is stored.

Effects due to pile-ups can easily be corrected, as the extracted time information is reliable. The energy spectra can then be multiplied by a correction factor obtained from the fraction of events tagged as pile-up versus those detected properly in each selected time window, whereas the time channel dead time has to be determined experimentally.

Such corrections can be easily applied when working at constant counting rates, mea-

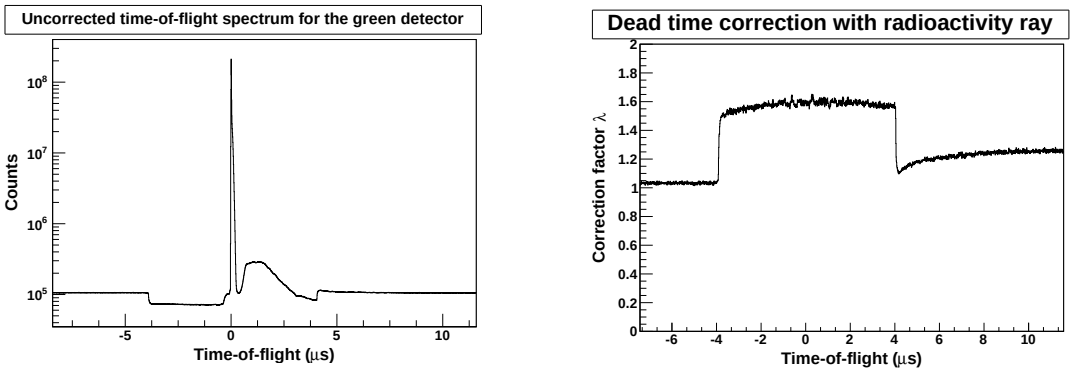

(a) (b)

Figure 3.12: Raw time-of-flight spectrum where no pile-up events are considered for the green detector (a), correction factor λ as a function of time for the dead time and pile-up correction.

suring for example radioactivity only. When using in-beam data however, the very intense γ flash complicates the situation and the correction is not so straightforward as the unknown time channel dead time varies strongly.

For this reason, a radioactivity ray emitted by the highly radioactive samples used in the experiments is monitored constantly to obtain precise time-of-flight dependent dead time information. This radioactivity ray is then corrected for constant counting dead time as explained above.

Figure 3.12(a) shows a time spectrum for which neither pile-up events, nor events lost due to dead time are considered. The drop in the count yield caused by the γ flash, can be clearly observed starting 4 μs before the flash and extending to 4 μs after. Figure 3.12(b) shows the correction factor λ for the spectra obtained by monitoring a radioactivity ray.

The correction factor at the beginning of the time gate equals roughly 1.03, caused by a 3% dead time measured for constant radioactivity counting. Upon the arrival of the γ flash however one can observe a correction of $\lambda > 1.6$. The γ flash is thus the main factor creating dead time, in this case around 60% for the green detector.

Bibliography

[1] W. Mondelaers and P. Schillebeeckx, *GELINA, a neutron time-of-flight facility for high-resolution neutron data measurements*, Notiziario neutroni e luci di sincrotrone **Vol. 11** (2006), 19-25.

[2] D. Ene, C. Borcea, S. Kopecky, W. Mondelaers, A. Negret, A.J.M. Plompen, *Global characterisation of the GELINA facility for high-resolution neutron time-of-flight measurements by Monte-Carlo simulations*, Nuclear Instruments and Methods in Physics Research **A618** (2010), 54-68.

[3] R. Morrison, *Grounding and Shielding Techniques in Instrumentation*, 3^{rd} edition, Wiley-Interscience, 1986

[4] M. Richer, C. Santos, *TNT2 Digital Pulse Processor Functionalities & TUC control software*, online: http://www.iphc.cnrs.fr/-TNT-.html, IPHC, 2007.

[5] A.-P. Malvino, *Principes d'électronique*, 6^{e} édition, Dunod éditions, 2002

[6] V.T. Jordanov, G.F. Knoll, *Digital synthesis of pulse shapes in real time for high resolution radiation spectroscopy*, Nuclear Instruments and Methods in Physics Research **A345** (1994) 337-345

Chapter 4

High Precision Measurements

This chapter presents two different topics which have been investigated to improve the performance of the designed experimental setup, keeping in mind that the setup must be able to measure (n,xn) reaction cross sections with the highest precision possible.

These investigations focus on the efficiency of the different detectors. In fact, the efficiencies play a key role in the computation of the cross sections, and it is mandatory to reduce their uncertainty to an absolute minimum. The first section of this chapter is dedicated to the detection precision of the fission chamber, while the second one treats the efficiencies of the HPGe[1] detectors.

4.1 Fission chamber efficiency

Measuring cross sections at high precision requires an excellent knowledge of the incident neutron flux. In the experimental setup conceived for this work a fission chamber is used to monitor the incident neutrons. The following sections treat the operating mode of the chamber and discuss several campaigns conducted to obtain the efficiency parameter with a very high accuracy.

4.1.1 Detection properties

A fission chamber is an ionisation chamber containing a fissionable deposit, which is in our case a highly enriched ^{235}U layer. The exact specifications of the chamber used are given in table 4.2. Incident neutrons interact with the uranium and induce fission reactions yielding two or three fission products, referred to as binary or ternary fission respectively. The probability of the latter being below 0.3% [2], it can be neglected in the further discussions and all fissions can be considered as binary. The characteristics of the emitted fragments (kinematics, mass distributions, etc.) are given in table 4.1.

The fission products lose their energy inside the chamber through ionisation of the gas, which can be described thanks to the well-known *Bethe-Bloch* formula. Electron-ion pairs are created in a number proportional to the energy deposited in the gas. Applying a voltage of about 150 V/cm on the electrodes of the chamber is sufficient to prevent the

[1] HPGe: High Purity Germanium

		Mean	FWHM
Kinetic energy [MeV]	light fragment	102	12
	heavy fragment	68	18
Mass [a.m.u.]	light fragment	93	16
	heavy fragment	139	17
Charge [e]	light fragment	21	2
	heavy fragment	22	2

Table 4.1: Characteristics of the ^{235}U fission products and their normal distributions [2, 3].

created pairs from recombination and to collect them. The electrodes are connected to a preamplifier to treat the generated pulses.

The signal created by a particle interacting in the gas depends on its energy, and thus on the number of electron-ion pairs created. When the collection time of the signal and hence the RC constant of the preamplifier is sufficiently low, only the electrons are collected as their mobility is much higher than the ones of the ions. In this particular case, the signal also depends on the distance passed by the electrons to reach the anode. The signal S can then be written as the sum of a term of each charge deposition Q_i, the deposition distance d_i to the anode, the fission chamber active volume, i.e. the distance between the anode and the cathode D and the capacitance of the chamber [1]:

$$S = \sum_i \frac{Q_i}{C} \cdot \frac{d_i}{D} \tag{4.1}$$

For a fission chamber operated at a gas pressure of 1 atm, created fission products have a range of 2 to 3 cm. Chambers with an effective thickness smaller than this value can be considered as energy-loss (ΔE) chambers, as they only ingest the partial energy lost in the volume. The remaining energy is deposited on the electrodes of the chamber. It is to note that the stopping in these electrodes also creates electron-ion pairs, some of which may become subject of attraction by the electrical field and thus migrate to the anode and create an additional signal.

4.1.2 Characteristics of the fission chamber

The fission chamber used for our experiments consists of two separate uranium deposits: a vacuum evaporated UF_4 foil and a spraypainted U_3O_8 layer. Both deposits are operated as two independent detectors. The gas in the chamber is P10[2] at a pressure of 1 atm. A schematic representation of the chamber is given in figure 4.1 and the details of the different deposits are given in table 4.2.

Both deposits are very highly enriched in ^{235}U, with percentages above 99.5%. The small quantities of other uranium isotopes do not have a significant contribution to the fission chamber yield, because their neutron induced fission cross-sections are comparable to the one of ^{235}U. For this reason we can consider an isotopic percentage of 100% ^{235}U.

[2]The P10 gas is a mixture of 90% argon and 10% methane

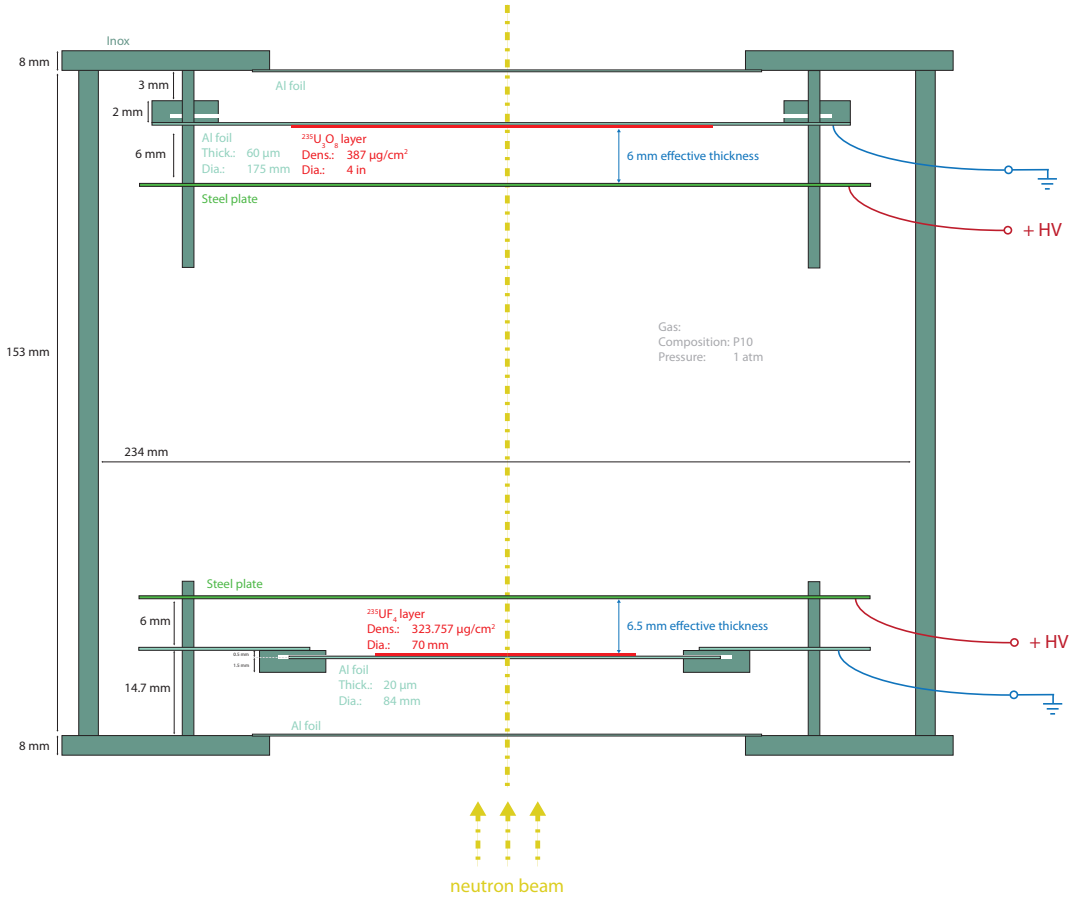

Figure 4.1: Schematical representation of the fission chamber.

UF_4	Lot number		929A (H)
	Preparation method		Vacuum evaporation
	Position		27.2601 m
	Composition		UF_4
	Density	ρ	6.7 g/cm^3
	Diameter		7.00 cm
	Surface		38.48 cm^2
	Thickness[a]	e_U	639,52 nm
	Uranium mass	m_U	12.46 mg
	Surface density of uranium	ς	$8.2978{\cdot}10^{17}$ atoms/cm^2
			323.757 $\pm$ 1.740 μg/cm^2
U_3O_8	Lot number		SP3530
	Preparation method		Spraypainting
	Position		27.4151 m
	Composition		U_3O_8
	Density	ρ	8.38 g/cm^3
	Diameter		10.16 cm
	Surface		81.07 cm^2
	Thickness	e_U	545.7 nm
	Uranium mass	m_U	31.38 mg
	Surface density of uranium	ς	$9.919{\cdot}10^{17}$ atoms/cm^2
			387 $\pm$ 3 μg/cm^2

[a]The thickness e_U of the uranium foil is calculated according to $e_U = \frac{\varsigma}{\rho \cdot f_U}$. The surface density ς along with the volume density ρ being known, a correction of the uranium mass fraction $f_U = 75.56\%$ for UF_4 and $f_U = 84.63\%$ for U_3O_8 is necessary

Table 4.2: Characteristics of the two deposits used in the fission chamber.

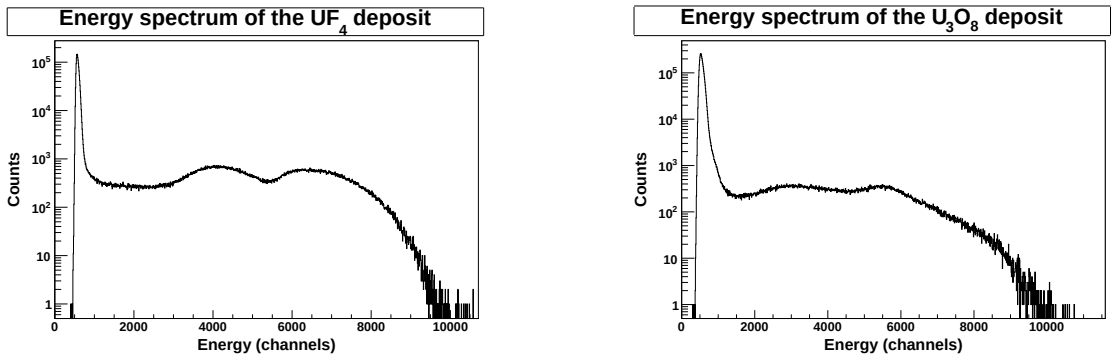

(a) (b)

Figure 4.2: Energy spectrum for the fission chamber deposits UF_4 (left) and U_3O_8 (right) with its initial configuration: the gap between the electrodes is 8 mm with reverse biasing.

The process of vacuum evaporation leads to deposits which are much more uniform than spraypainting. For this reason one can observe a much better resolution for the UF_4 energy spectra than the U_3O_8 yields as illustrated in figure 4.2.

4.1.3 Determination of the fission yield

An energy spectrum for the UF_4 deposit acquired during (n,xnγ) measurements at the GELINA facility is shown in figure 4.2(a). In the low energy domain of the energy spectra one can see a very strong contribution coming from the α particle signals, which are due to the radioactivity of the uranium foils. To the right, in the higher energy ranges one can observe events due to fission products in a double-humped shape.

Separating the α particle signals from the fission events is a delicate process. In fact, the signal amplitudes generated both by the uranium decay and the neutron induced fissions have a respective upper limit value, i.e. their pulses are always weaker than a certain energy, but they do not have a lower limit. This means that the fission product signals share a part of their energy domain with the α particle signals which makes a strict separation between both types of signals very difficult.

In the upcoming sections we discuss different possibilities to determine the most accurately possible the number of fission products in the spectra.

4.1.3.1 Alpha subtraction

A possible approach to obtain spectra without α particle signals is to use off-beam background data, for which no neutron-induced fissions occur. These can then be used to subtract the α decay signals from the data acquired during the experiments. This procedure however turns out to be very difficult, even impossible.

One one hand, the electromagnetic noise generated by the modulators of GELINA, as discussed in section 3.2.3.2, induces a shift in the experimental data of several channels. In this case the background data is not aligned with the experimental data leading to difficulties in subtracting both spectra.

On the other hand, the number of fission products produced n_{FP} is very low compared to the number of α particle detections n_α. For some regions their ratio is so weak that the absolute statistical error on the α decay signals Δn_α is superior to the detections of fission products:

$$\Delta n_\alpha > n_{FP} \tag{4.2}$$

In these circumstances a subtraction would clearly lead to a too large error on the fission yield values.

4.1.3.2 Energy threshold

The only realistic approach that may be considered to obtain the net fission spectra is to apply a threshold value to the energy yields and to correct for the portion of fission fragments lost. This can be achieved by performing a cut above the maximum expected α energies in the valley between the α peak and the main fission product peak.

To obtain a good correction coefficient we have to study precisely the behaviour of the fission fragments. Actually, as they have a very high stopping coefficient, and thus a very low range, they interact very strongly within the first μm of their trajectory. In the following we consider the three distinct scenarios:

- The fission fragment's energy loss inside the uranium layer is so important that it is completely absorbed in the foil. In this case no pulse is generated in the gas chamber.
- The fragment path is long enough to leave the uranium layer, although a high portion of its energy is lost in the deposit and the residual energy loss in the gas is very weak, so that the signal produced is located in the energy range of the α particles.
- The energy loss of the fission product inside the foil is weak with respect to the energy lost in the gas. The generated pulse will be strong enough to be outside of the α region.

Before discussing the different cases however, we will first study the effect of the fission chamber geometry on the different energy spectra to find the optimal configuration, yielding the highest efficiency possible.

4.1.4 Optimisation of the fission chamber configuration

Precise knowledge of the efficiency of the fission chamber plays a key role in lowering the uncertainties on the flux determination, although it is not the only important factor. Indeed, the configuration of the fission chamber itself is also significant: as mentioned above, it is necessary to apply a threshold on the energy spectra in order to remove the α particle contribution. It is very important to determine a configuration for which this threshold value will be able to eliminate the α compound, without losing too many signals from the fission products. Before we can determine the efficiency precisely we thus have to discuss the impact of the chamber's geometry on the fission yield results and determine the best configuration of the chamber.

For this work the fission chamber was mounted at the Van de Graaff accelerator of IRMM, Geel, Belgium. Monoenergetic neutrons were produced through

$$\mathrm{p} + \mathrm{T} \rightarrow {}^{3}\mathrm{He} + \mathrm{n} \tag{4.3}$$

reactions, yielding neutrons of $E_n = 1.25$ MeV. The accelerator was operated in continuous mode, i.e. there was no time-of-flight information available. For this reason it was not possible to eliminate secondary neutrons, created mainly by thermalisation due to scattering inside the experimental hall. Actually, these have a very high fission cross section in ^{235}U, and the measurements could hence not be used to make precise efficiency calibrations rather than just comparisons of the different configurations studied. Further configuration options have been probed by mounting the chamber at the Gelina facility at the 30 m experimental setup.

The first effect we studied was the impact of the active zone of the chamber on the signal yields. In fact its depth e_{FC} must be chosen very carefully to obtain a good separation between the fission product signals and the α contribution. For this purpose the distance between the uranium deposit and the mass electrode was set to $e_{\mathrm{FC}} = 6.5$ mm, $e_{\mathrm{FC}} = 8$ mm and $e_{\mathrm{FC}} = 27$ mm (see figure 4.3(a)). The statistics of the various sets of measurement were very different as the acquisition time varied strongly for the different runs, therefore they were normalised to monitor counts.

It is noteworthy to mention that the signal is not getting stronger when increasing the gap between the anode and the cathode. This is due to the fact that the signal also depends on the distance D between these electrodes as given by equation 4.1. Actually an increase of the volume of the chamber mainly plays on the α contribution rather than the one of the fission fragments. The range of α particles in the gas is four to five times longer than that of the fission fragments and the main energy loss occurs in the *Bragg peak*, whereas the energy loss of the fission fragments can be considered as continuous. By increasing the chamber volume the α signal grows significantly stronger, unlike the one of the fission products. The valley between the α contribution and the fission products that can be observed for small volumes vanished when reaching a thickness of over 27 mm. The value of the energy threshold required to remove the α compound is so high that a very large amount of fission events are lost. The efficiency of such a configuration is thus very low and the best configuration is obtained when the height of the valley versus the one of the main fission peak is smallest. This is given for very small thicknesses below 8 mm.

In a second step we analysed the effect of applying the positive high voltage to the uranium foil or to the opposite electrode, referred to as reverse and forward biasing respectively. As we only collect electrons, the high voltage plate will work as read-out electrode. As shown in figure 4.3(b) this configuration option strongly affects the height of the valley separating α and fission contributions. Indeed, the difference occurs for the fragments which are stopped in the gas, before reaching the other side of the chamber. When the electrons are going back to the uranium foil, the distance travelled is much shorter than if they have to go to the opposite electrode. As the signal created is proportional to the distance travelled, it is stronger in the latter case: events that would produce a signal in the valley region in reverse biasing are yielding signals at higher amplitudes, thus creating a better separation between the α and fission distributions, while the signal given for

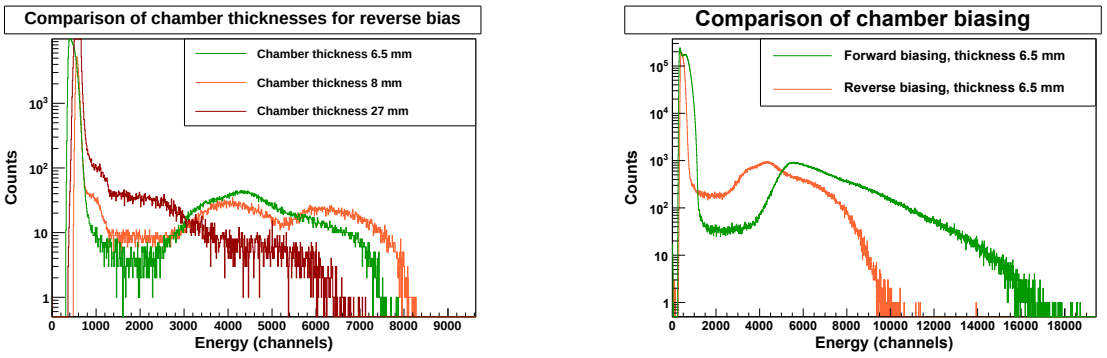

(a) (b)

Figure 4.3: Comparison of the different configuration possibilities of the fission chamber: (a) shows the effect of varying the effective volume of the chamber, (b) shows the effect of polarisation changes.

fragments not stopped in the gas (i.e. stopped in the facing electrode) is the same in both scenarios. For that reason the forward biasing has to be preferred as a higher efficiency is obtained.

These observations made us chose a gap between electrodes of $e_{\mathrm{FC}} = 6.5$ mm for the UF_4 deposit and 6 mm for the U_3O_8 deposit at forward biasing.

4.1.5 Estimation of the events lost inside the uranium foil

Considering the first case mentioned above, we have to compute the fraction of events lost when the fission fragment is entirely absorbed in the uranium sample the most precisely possible. This ratio can in fact be easily estimated from the simple equation:

$$\Delta_{t/2R} = \frac{t}{2R} \tag{4.4}$$

where t denotes the thickness of the layer and R the average range of the fission fragments inside the foil. Unfortunately, these range values vary strongly depending on the reference consulted. According to the SRIM-2010 software [4] a mean range, taking into account the distributions for fission fragments given in table 4.1, in UF_4 is approximately $R_{\mathrm{SRIM}} = 7.3$ mg/cm^2, while [5] claims tabulated values of $R_{\mathrm{Littmark}} = 5.7$ mg/cm^2. This observation leads to conclude that ranges of heavy ions in matter are not known very precisely and may be affected by uncertainties of more than 20%.

Furthermore, the correction for the loss of fission fragments inside the deposit of ionisation chambers does not only depend on the range of the ions but also needs to include corrections for back-scattering of the second fission product into the active volume of the chamber. These effects were precisely studied by Budtz-Jørgensen et al. [5], were experimental data shows a correction ratio for fission fragments lost inside a UF_4 deposit of:

$$\Delta_{Budtz} = (10.5 \pm 0.7) \cdot t \quad \% \tag{4.5}$$

Combining equations 4.4 and 4.5, one may define an *effective range* R_{eff} for fission fragments, which then equals 4.76 mg/cm^2 for UF_4 samples. Results for U_3O_8 yield an effective range of $R_{eff} = 1.35$ mg/cm^2. However, this value should be considered with extreme caution, as it is strongly affected by the poor quality of the spraypainted deposit.

While the above results were obtained for thermal neutron-induced fission, we have to adapt the correction coefficients for fast neutrons, as the energy domain of the neutrons to be detected ranges from 100 keV to 20 MeV. In fact, fast neutrons have a non-negligible impact on the angular distribution of the fission fragments. Let us define the ratio of nucleus velocity to average fragment velocity by:

$$\eta = \frac{\sqrt{T/T_f \cdot A_f}}{A_t + 1} \tag{4.6}$$

where T is the neutron's kinetic energy, T_f the average fragment kinetic energy, A_f the average fragment's atomic weight and A_t the atomic weight of the target nucleus. The inefficiencies of the fission chamber are then given [6] as:

$$\Delta_{UF_4} = \frac{t}{2R}\left(1 - \eta\left(\frac{2R}{t} - \frac{R^2}{t^2}\eta\right)\right)\left(1 - \frac{a_2}{2}\right) \tag{4.7}$$

for the UF_4 deposit, for which the foil is facing away from the source, and

$$\Delta_{U_3O_8} = \frac{t}{2R}\left(1 + \frac{2R}{t}\eta\right)\left(1 - \frac{a_2}{2}\right) \tag{4.8}$$

for the U_3O_8 deposit, for which the foil is facing the neutron source. The a_2 factors denote the second order coefficients of the Legendre polynomial describing the anisotropy of the fission fragments from ^{235}U. These formulae take into account the efficiency loss of equation 4.4 corrected by two factors, one taking into account the angular distribution of the fission fragments and another one taking into account the kinematic effect of the incident neutron.

Using the a_2 coefficients from [7] and as range values the effective ones introduced earlier we find fission chamber inefficiencies, i.e. a loss of events, varying from 3.15 to 1.40% for the UF_4 deposit (figure 4.4). One can observe that the efficiency of the UF_4 foil increases with neutron energy, as the angular distribution of the fission fragments gets more forward-peaked and thus more fragments are directed into the active volume of the chamber.

For the U_3O_8 film, the loss is much higher as the range of the fission fragments used for the calculations is much lower. Moreover the effect of the angular distribution is less pronounced as it increases with η and decreases with a_2. As both coefficients grow larger with increasing energy, they compensate and only give rise to inefficiency variations between 14.1 and 15.0%. Let us point out again that the results for the latter deposit are to be considered with extreme caution, as a very low effective range obtained from the discussions above was used.

4.1.6 Estimation of the events lost due to the energy threshold

The correction for the loss of fission fragments producing a weak signal, lost due to the application of an energy threshold can be discussed using a simple model calculation.

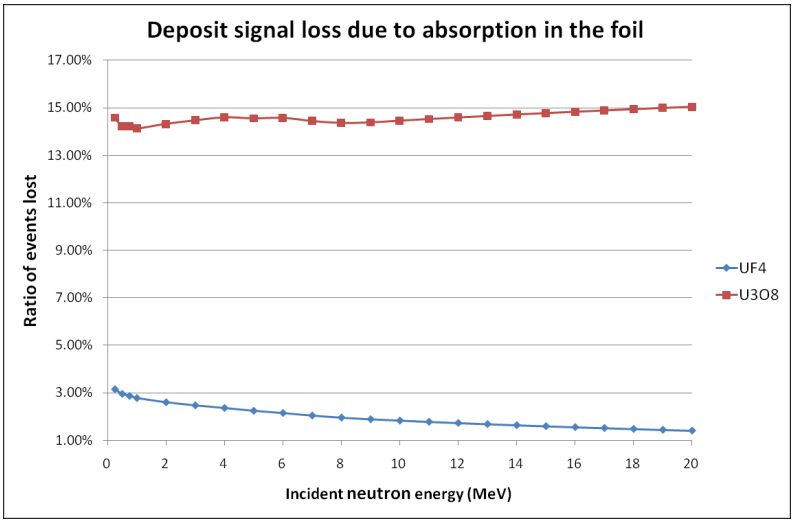

Figure 4.4: Ratio of events lost in the fission chamber due to absorption inside the deposit for the UF_4 layer (blue) and the U_3O_8 foil (red).

Indeed, considering a fission fragment with average energy and range, one can compute the signal produced inside the ionisation chamber according to equation 4.1 by assuming a constant energy loss. The results of such a model calculation [8] show that a non-zero yield of the spectra at zero energy can be expected, and that a linear extrapolation from the plateau between the α particle peak and the fission product contribution to zero energy can be adopted to take into account events lost due to an energy cut.

In order to verify the previous considerations on the energy loss inside the deposit, and to check the extrapolation to zero energy by a more complete model, Geant4 [9] simulations were performed, where one million events were simulated.

For this purpose we considered a $^{235}UF_4$ foil in which a pair of fission products were randomly shot in opposite directions using an isotropic distribution. The energy and mass distributions for the fission fragments were taken from table 4.1. Next to the uranium deposit a P10 gas filled chamber of variable size e_{FC} was simulated as active volume. The energy lost inside this volume, computed according to Geant4, was multiplied by the distance to the collection electrode according to equation 4.1 enabling us to reproduce the signal amplitudes. The adjustment of the constant multiplication factor $\frac{1}{CD}$ was done at a later point by fitting the simulated spectra to the experimental ones. The final signal S was then redistributed according to a normal distribution $\mathcal{N}(S;\, \sigma = 0{,}04 \cdot S)$, to take into account the detection resolution.

The first configuration studied was the reverse bias configuration, were the uranium foil was at high voltage, and was thus responsible for the collection of the electrons. The active volume of the fission chamber corresponds to the distance between the anode and cathode and was for this study $e_{FC} = 8$ mm. The result of this first simulation is shown in figure 4.5(a). The plateau before the main fission hump could be simulated satisfactorily, but this simulation was not able to reproduce the second hump in the high energy range.

Several changes and tests in the simulation programs finally lead us to consider part of the opposite electrode as active volume as well. In fact, as already mentioned in section 4.1.1, the fission products are not stopped entirely in the gas for an active depth of 8 mm. The remaining energy is left in the opposite electrode. Ionisation created in this electrode can be subject to a contribution in the final signal. The best fit for simulation to experimental spectra was obtained for an effective depth of 1.4 μm of the steel plate facing the uranium foil. The result is shown in figure 4.5(b).

The same operation was repeated for a chamber thickness of $e_{FC} = 6.5$ mm. Figures 4.5(c) and 4.5(d) show the output without contribution of the steel plate and with a contribution of the first 1.4 μm of the plate respectively. This verifies the observation made above, and the spectra fit better when an opposite electrode participation on the signal is taken into account. Further simulations were performed for a chamber with an active depth of 27 mm. As for such a distance almost all the fission fragments are stopped inside the gas, there is no effect of adding an opposite electrode contribution. The simulation result is displayed in figure 4.5(e) where a very nice agreement between simulated and experimental spectra is found.

Finally we also simulated the forward bias configuration with a chamber thickness of $e_{FC} = 6.5$ mm, corresponding to the optimum configuration as discussed in section 4.1.4. For this simulation the deposited energy was not multiplied by the distance to the uranium foil, but to the distance to the opposite electrode, as this one is working as collection electrode in this configuration. A contribution of the steel plate could thus be neglected, as its distance and hence the signal produced in it is very weak. The simulation result is shown in figure 4.5(f).

As the results show, the computed spectra could be fitted satisfactorily to the experimental ones at rather high energy ranges for the reverse bias configuration, whereas the agreement is less good for the forward bias case. All the results present overestimated simulation yields compared to the experimental data in the low energy domain. This phenomenon could be explained by the fact that the energy loss of heavy ions is not known at a level precise enough to reproduce the measured data and thus yielding a smaller plateau to main fission fragment contribution ratio.

Nevertheless it can be observed that for the reverse bias configuration a slight upturn is seen at zero signal amplitude, while the forward bias mode rather presents a downslope below the α particle contribution. This same observation could also be made when using the simplified model calculation mentioned above. Neglecting the fact that the low energies are not simulated at the desired level, this could be an indication of the shape of the fission fragment signal in these regions and construe an extrapolation of the experimental spectra from the threshold value to zero energy. The simulations are however not trustworthy enough to apply such an extrapolation without further investigations justifying this procedure.

The preceding study was limited to the UF_4 deposit of the fission chamber. Analogous simulations have been performed on the U_3O_8 foil showed a similar behaviour at low energies, although the agreement between simulated and observed spectra was much worse in general. This effect is due to the poor uniformity of the spraypainted deposit.

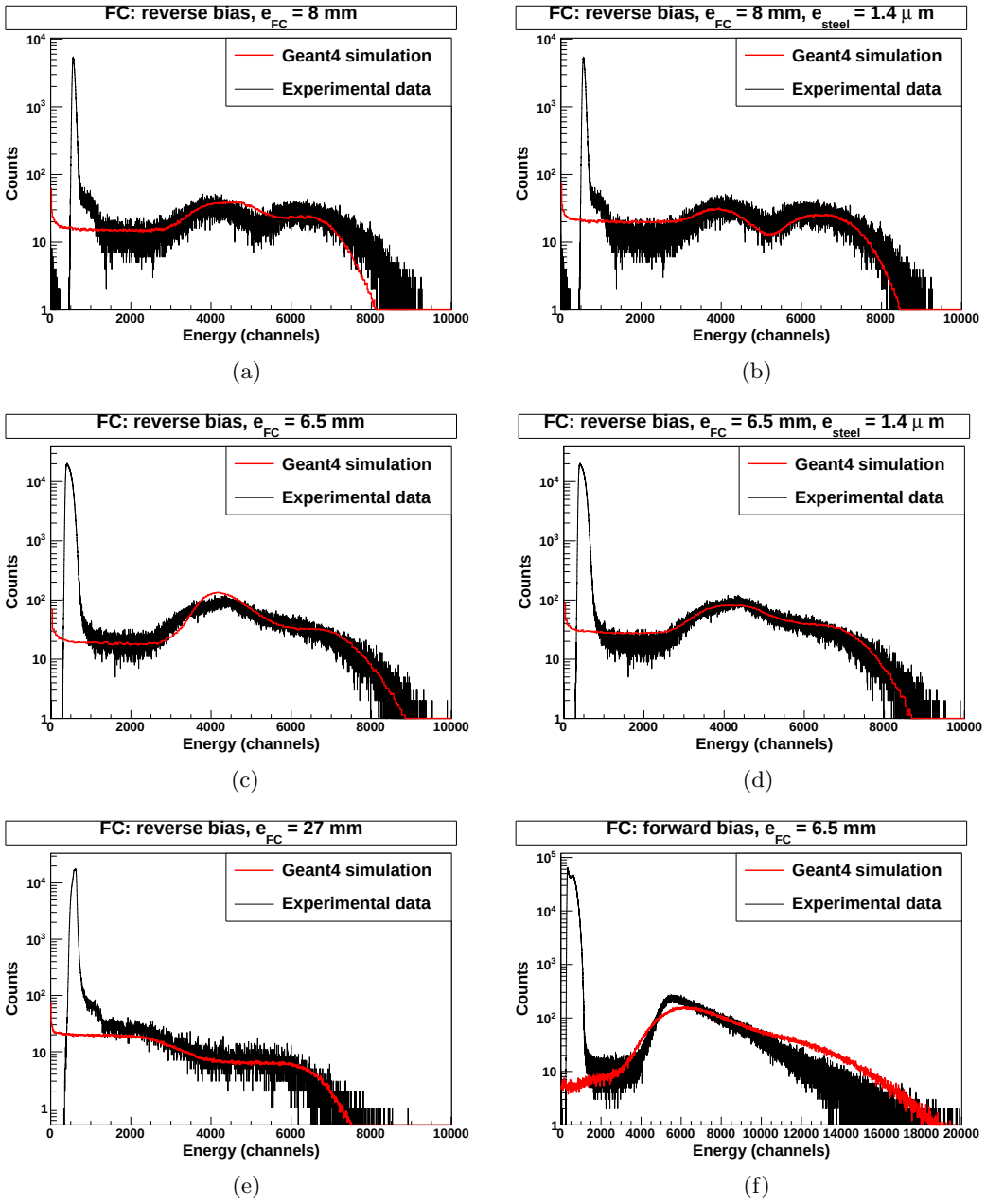

Figure 4.5: Energy spectra observed experimentally (black) versus simulated spectra (red) for different configurations of the fission chamber.

4.1.7 Calibration Measurements at PTB

To verify the previous results and mainly to obtain more information on how to account for the fragments lost due to the energy threshold, we made precise calibration measurements at the Physikalisch-Technische Bundesanstalt (PTB) in Braunschweig.

4.1.7.1 Experimental Setup

For these calibration measurements the fission chamber was mounted in front of a Van de Graaff accelerator, producing neutrons by

$$\mathrm{d} + \mathrm{D} \rightarrow {}^{3}\mathrm{He} + \mathrm{n} \tag{4.9}$$

reactions. An incident pulsed deuteron beam with kinetic energy $E_d \approx 5.5$ MeV hits a deuterium gas target at a frequency of 935 kHz. The produced neutrons have a peak energy of $E_n \approx 8.5$ MeV. The fission chamber was positioned at a distance of 1.5 m from the deuterium target.

The data acquisition was done with an analog system from the IRMM, Geel, Belgium. Time of flight and energy information were saved in list mode files, enabling time gating on the acquired data, to eliminate neutrons with wrong energy, e.g. born through break-up reactions in the deuterium target or slowed down through scattering in the experimental hall. For the measurements several foreground runs were performed to obtain statistics of at least 10000 events in the fission chamber. Two series of background measurements were made: the first by placing a shadow cone between the neutron source and the detector to evaluate the indirect component of fission events generated and a second by taking the deuterium gas out of the target and bombarding the empty target with deuterons to estimate the amount of neutrons created by other mechanisms than that of reaction (4.9).

The beam was monitored using the charge integrator of the accelerator as well as several BF_3 counters located at different places in the experimental hall. These were calibrated using a high precision Proton Recoil Telescope. The measurements were compared by Ralf Nolte et al. to a scintillator and two calibrated fission chambers, one containing a ^{238}U foil, and another one with a ^{235}U deposit.

4.1.7.2 Results

As mentioned above, the data was saved in list mode files to be able to cut back on the neutrons created by other processes than the direct reaction given in (4.9). To determine a good time gate for the neutrons of interest, the time of flight spectra were simulated by our colleagues at PTB. Figure 4.6(a) shows an acquired spectrum for a foreground run in black and a simulated one in red. The contribution to the left in the red spectra consists of neutrons produced through break-up reactions. By comparing both graphs, this enables us to set a gate on the time-of-flight spectra which only includes neutrons produced by the direct mechanism and thus eliminating the undesirable compound.

For the chosen time gates the monitor normalised energy spectra are extracted for the foreground and background runs as shows figure 4.6(b). After subtraction of the latter ones, we obtain the final energy spectrum, to which we apply an energy threshold as

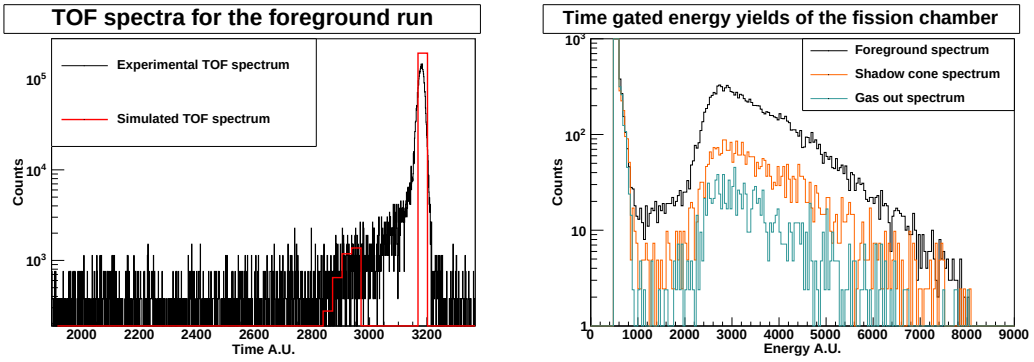

(a) (b)

Figure 4.6: Time of flight spectra for the PTB runs: experimental data in black and simulated spectra in red (a) and energy spectra for foreground and background runs (b).

discussed earlier. The value for this threshold was chosen at the local minimum, corresponding to channel 1500 in this case and the number of counts n_{det} above was integrated to compute the incident neutron flux.

The neutron flux Φ is then given by:

$$\Phi = \frac{n_{det}}{\varsigma \cdot \sigma_f}(1 + a_{air}) \cdot (1 + t_{dead}) \tag{4.10}$$

where ς is the areal density of uranium in the deposit from table 4.2, a_{air} the air attenuation factor of the neutrons before hitting the fission chamber, determined by MCNPX[3] [10] simulations to be (1.010 ± 0.015) %, and t_{dead} the dead time of the acquisition determined to be 0.51%. The precise neutron energy was fixed at $E_n = (8.39 \pm 0.04)$ MeV from the measurements of the scientists at PTB. For this energy, the fission cross section is retrieved from the ENDF/B-VII.0 database, where we found $\sigma_f = (1.793 \pm 0.014)$ b by interpolation.

With these values we determined a fission fragment yield of 10 005 counts above threshold for the UF_4 deposit. Introducing these values into equation (4.10), we obtain a neutron flux per monitor charge of $1.83 \cdot 10^5 \frac{n}{\mu C}$. Comparing this to the reference data obtained by the PTB counters leads to a final experimental efficiency of:

$$\epsilon_{PTB} = (94.4 \pm 2.1)\% \tag{4.11}$$

The uncertainty follows from considering a 1.0% error on the number of detections, 1.0% uncertainty on the air attenuation correction and an additional 1.5% error on the measured reference flux. The determination of the efficiency of the fission chamber is affected by a total error of 2.1% according to the propagation of uncertainty formula. In this error calculation the systematic uncertainties of parameters of the fission chamber, such as the areal density and the fission cross section were neglected, as these are already included in the final flux calculation and the interest here was to determine the uncertainty on the efficiency parameter only.

[3]The MCNPX version used for the attenuation measurements in this work was version 2.6d

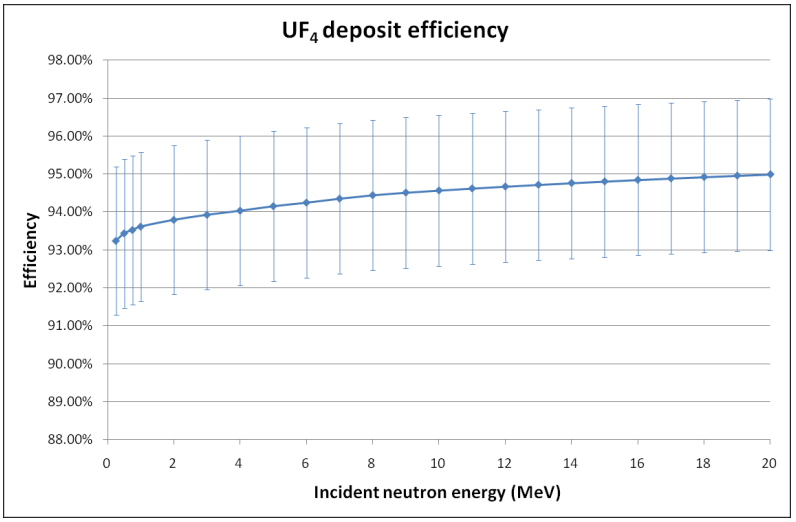

Figure 4.7: Final efficiency values as a function of the incident neutron energy for the UF_4 deposit.

When applying the previously discussed corrections, i.e. the corrections for fission fragment loss in the deposit and a horizontal extrapolation to zero energy in the domain below threshold, the expected efficiency would be:

$$\epsilon_{classical} = (94.4 \pm 2.1)\% \tag{4.12}$$

the error on this value is mainly due to the uncertainty arising from the extrapolation to zero energy below the threshold.

As already mentioned earlier, the U_3O_8 deposit is of poor homogeneity and the correction factors used for the UF_4 deposit can only be applied with extreme caution. Indeed, when applying the same procedure as for the UF_4 foil, the PTB results show an experimental efficiency of $\epsilon_{PTB} = (81.4 \pm 2.1)\%$, whereas the theoretical corrections predict an efficiency of $\epsilon_{classical} = (77.6 \pm 2.3)\%$ for this deposit.

4.1.8 Conclusions

Considering the corrections to be applied to the fission yield above threshold we were able to find a very good agreement between the theoretical considerations and the experimental measurements at PTB for the UF_4 deposit: both results agree almost perfectly. As the PTB measurement is the only one taking into account all effects affecting the efficiency of the fission chamber, such as the loss inside the foil and the loss due to the energy threshold, this measurement is used as a reference for the fission chamber in this work.

In order to take into account the anisotropy of the fission product distribution, the PTB value of $\epsilon = 94.4\%$ determined for an incident neutron energy of 8.39 MeV is used to scale the energy dependant efficiency described in earlier in section 4.1.5. The obtained values for the fission chamber efficiency are shown in figure 4.7. The overall uncertainty of the efficiency equals the one of the PTB experiment and is thus 2.1%.

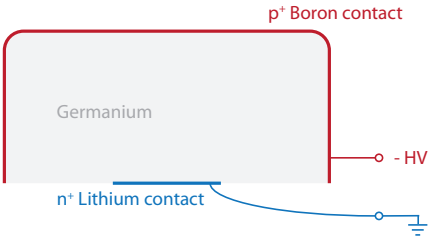

Figure 4.8: Schematical representation of the semi-planar HPGe crystals used in the experiment.

The difference observed for the U_3O_8 deposit between the PTB measurements and the classical approach is of 3.8%, and thus larger than in the case of the UF_4 deposit. This can be explained by the poor uniformity of this deposit, affecting the estimation of events lost inside the foil from a large uncertainty. It can however be observed that the measured values and the classical correction agree within the error bars. Nevertheless this difference motivated us to use only the UF_4 deposit for the flux determinations in this work.

4.2 HPGe detector efficiency

This section treats the efforts made to obtain very precise peak-efficiency values for the different HPGe detectors used. This factor is actually a very important source of error for γ spectroscopy measurements.

4.2.1 Detectors and their properties

The four detectors used in this work are semi-planar n-type HPGe detectors built by the manufacturer Canberra and are referred to as grey, green, red and blue detector. The blue and green semiconductors have a smaller crystal, with a thickness of about 2 cm and a diameter of approximately 3.5 cm, whereas the grey and red detectors have thicknesses of circa 3 cm and diameters of roughly 6 cm. The exact dimensions are listed in table 4.5.

All four counters are featuring bulletized (rounded) front entrances. As shown in figure 4.8, the p^+ contact of the semiconductor, made through implantation of boron ions, is surrounding the entire crystal and induces a quite thin dead zone, while the back part of the crystal holds the n^+ lithium contact and is affected by a larger dead layer due to the implantation of the thicker n^+ contact.

Interacting γ rays in the active part of the semiconducting germanium will lead to the creation of electron/hole pairs, in a proportional number to the energy deposited [1]. To avoid recombination of these charges and to ensure their collection on the electrodes, the region between the two contacts is depleted by applying a sufficiently high voltage. As shows table 4.3 a voltage of the order of 1000 V, depending on the purity of the germanium, is sufficient to fully deplete the crystal, although the electric field can be very weak in some parts of the semiconductor. For this reason the nominal operating voltage is higher, to be sure to collect the charges in an acceptable time interval. Indeed, if the field is too

Detector	Depletion voltage	Nominal voltage
Grey	600 V	2500 V
Red	no information available	5000 V
Green	1750 V	4500 V
Blue	1250 V	3000 V

Table 4.3: Depletion voltages and nominal operating voltages of the four detectors used.

weak the charges may not be collected quick enough to generate a detectable pulse. The operating voltages of the detectors range between 2500 and 5000 V.

4.2.2 Efficiency computing method

The absolute photopeak-efficiency of a germanium detector in the case of extended samples depends on several parameters, which have to be taken into account in the total efficiency calculation. Beside the position of the detector with respect to the γ-ray emitting sample and the energy of the studied γ ray, these parameters also include:

- the shape of the γ-ray emitting sample (in our case this corresponds to the beam diameter of the order of 5 cm)
- the geometry of the crystal inside the detector
- the auto-absorption k_{E_γ} of the γ rays inside the sample

Calibrations realised with a point source only are not sufficient in our case, as the studied sample is not point-like, i.e. the geometrical distributions of the emitted γ rays cannot be calculated at a satisfactory level. Another difficulty is introduced by the absorption of the γ rays inside the sample which is an important factor as the density and thickness of the used samples are rather high.

The best way to consider all these parameters is to measure the efficiency with calibrated sources and to compare these to Monte-Carlo simulations of the detector [11]. The procedure for this method is realised in several steps: First, the geometry of the crystal is determined and entered into a Geant4 [9] simulation code. Then calibrated sources (point-like and extended) are placed at different spots of the sample position. The obtained results are compared to the simulated spectra. The differences in the yields are used to determine the dead layers of the crystal and to calibrate the simulation input. Once the simulation parameters are fixed, the second step consists of simulating the studied sample. For this purpose the geometry of the sample is entered into the simulation code and γ rays of the energies of interest are shot randomly within the sample. The ratio between the number of events in the photo-peak and the number of γ rays simulated is the absolute peak-efficiency of the detector.

4.2.3 Determination of the crystal geometry

The specifications of the detector, including the shape of the germanium crystal, came with the different detectors when they were purchased. These data were first used as an

input for our simulations. As no reliable information on the dead layers of the crystal were provided, the following considerations were made.

4.2.3.1 Estimation of dead layers

In the detectors used there are two different types of dead layers: the one due to the p^+ contact of the semiconductor, which extends all around the crystal, namely its front entrance and the sides, and the one due to the n^+ contact at the back. As these contacts are made differently, the dead regions induced by them are totally independent and of very distinct size.

The front entrance's dead layers will mainly affect weak γ-ray energies, as these interact within the first millimetres of the crystal. Using a calibrated source, one can easily determine the value of this zone by comparing the absorption of photons with different energies.

Indeed, a first estimation can be obtained via the equation:

$$I_\gamma(x) = I_{\gamma_0} e^{-\mu_\gamma x} \tag{4.13}$$

where $I_\gamma(x)$ corresponds to the intensity of the photon beam at distance x, I_{γ_0} is the initial intensity of the photon beam and μ_γ is the attenuation coefficient. Writing this equation for two different intensities, one can express the ratio of two γ rays as:

$$R = \frac{I_{\gamma 1}(x)}{I_{\gamma 2}(x)} = \frac{I_{\gamma 1_0}}{I_{\gamma 2_0}} \frac{e^{-\mu_{\gamma 1} x}}{e^{-\mu_{\gamma 2} x}} \tag{4.14}$$

Assuming that the active part of the crystal fully detects all incident photons not absorbed in the dead layer, the effective thickness of the inactive front part can be expressed as:

$$X = \frac{\ln \frac{R}{I_{\gamma 1_0}/I_{\gamma 2_0}}}{\mu_{\gamma 1} - \mu_{\gamma 2}} \tag{4.15}$$

This dead layer size was computed using the ratio of the 46.60 keV and 121.78 keV γ decays of a calibrated ^{152}Eu point source. As the used source was not collimated, it is important to remark that the above assumption is just an approximation. In fact, depending on the angular distribution, several photons are not entirely absorbed in the crystal. This effect concerns mostly the higher energy photons as their absorption coefficient is lower, and the value found using this approximation thus represents the minimum value which should be expected as dead zone thickness. Nevertheless this estimation should provide the needed starting value to be used for the simulations. The front and side dead layer thickness was projected at 20-25 μm depending on the detector. This depth is used as a starting point in the simulations for the surrounding dead zone of all our detectors.

As this assumption cannot be extended to the higher energy γ rays, the back dead region is determined by fitting the experiment to simulation ratios to obtain the correct values.

Eu "point-like"	Source	^{152}Eu
	Reference	PTB-6.11-191/14.97
	Diameter	2 mm
	Reference Date	1.06.1997
	Activity	$42.9 \cdot 10^3$ $\pm$ $0.3 \cdot 10^3$ Bq
	Half-life	13.51 $\pm$ 0.03 years
Eu "extended"	Source	^{152}Eu
	Reference	PTB-6.11-252/07.2009
	Diameter	50 mm
	Reference Date	1.07.2009
	Activity	$14.87 \cdot 10^3$ $\pm$ $0.23 \cdot 10^3$ Bq
	Half-life	13.51 $\pm$ 0.03 years

Table 4.4: Specifications of the different calibration sources used for the experimental efficiency determination.

4.2.3.2 Simulations with the constructor's input

Using the detector specifications provided by the constructor, a Geant4[4] simulation program was written. The emissions of the major γ-ray decays, in the energy domain between 46 keV and 1.086 MeV of a ^{152}Eu point source, were computed using the Monte Carlo technique, simulating 4 billion events per energy in 4π. In order to obtain unbiased results with these statistics, Geant4 was launched 20 times with 20 different randomised seeds for each simulation. The values obtained from these calculations were then compared to experimental measurements obtained using a calibrated source, whose specifications are given in table 4.4. As the aim was to adjust the simulation parameters to fit the actual data, we consider the experimental data to simulation ratios in the following sections.

The dead zones following the p^+ contact (at the front entrance of the crystal) were initially set to 25 μm as discussed in section 4.2.3.1 and the back dead zone was set to zero in a first step. Figure 4.9 shows a 3D representation of the crystal geometry as computed by Geant4. The ratio between experimental data and simulations for the grey detector are shown in figure 4.10. One can observe that this first simulation ignoring the back dead zones (red curve) only affects the weak energies, while the stronger γ-ray emissions are not simulated correctly. This was to be expected, as the impact of the back dead zone influences mostly the high energy γ rays.

In a second step, the n^+ contact dead region was adjusted to fit the high energy domain. An optimum value for this was found for a dead layer of 1.4 mm (orange graph), for which a rather flat line is obtained. However, these results still differ from the experimental ones by almost 10 %. Further adjustments on the dead layers at the front or the back would lead to only adjusting low or high energies, but not intermediate ones.

The best way to take into account the entire energy domain, i.e. for low, intermediate

[4]All the simulations concerning HPGe detectors in this work have been performed using the version 9.3 release of the Geant4 simulation toolkit

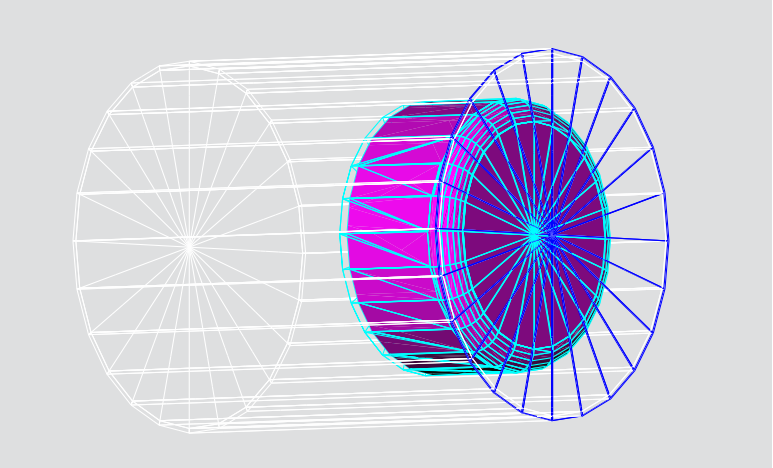

Figure 4.9: 3D representation of the crystal geometry as computed by Geant4 for one of the detectors. The detector cap is in white, with the front entrance window in blue. The active part of the germanium is represented in magenta and the dead zones are in cyan.

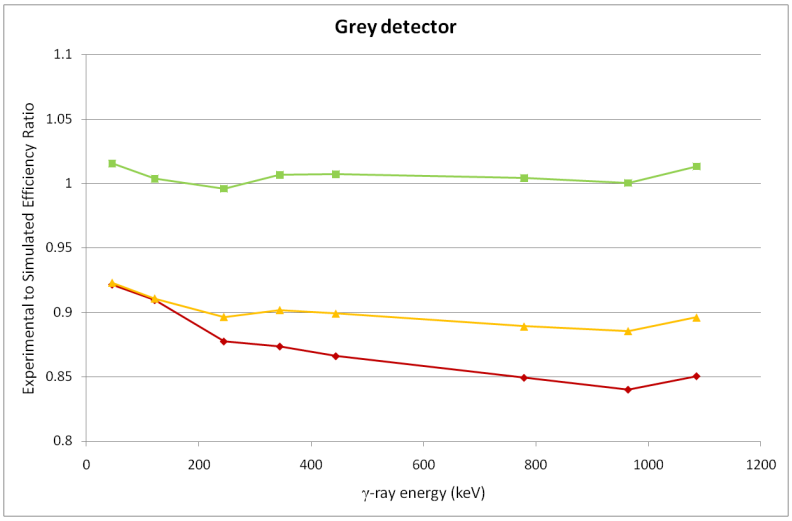

Figure 4.10: Experiment to simulation ratios of the grey detector computed for different dead zone considerations: dead zone of 25 μm at the front and around the crystal (red), an additional dead zone of 1.4 mm at the back (orange) and an additional reduction of the crystal diameter by 2.8 mm (green).

and high energies is to reduce the active crystal volume[5]. The most convenient way to achieve this is to reduce the diameter of the crystal. Unlike the front or back sides, which are mainly subject to weak or strong γ rays respectively, the sides of the crystal are concerned by the whole energy range, although their contribution is a little more vigorous for the high energies. The green curve in figure 4.10 shows the best fit obtained with a reduction of the crystal diameter by 2.8 mm. However, as there is no known physical reason for such a consequent dead zone, further investigations were necessary to justify this approach.

Further problems were observed for the green detector, which has a similar geometry as the blue one. When applying the same dead zones for both detectors, the constructor's specifications lead to an overestimated efficiency of several percent in the case of the green crystal. These issues called for a verification of the constructor data by reviewing the internal detector geometry which was realised through a microfocus computer tomography of the detectors.

4.2.3.3 Microfocus Computer Tomography of the detectors

Disassembling a HPGe detector in order to verify its internal geometry would be very complicated and could damage the detector. A non-destructive way to accomplish precise crystal measurements is to expose the detector to a radiative source. The feasibility of this method was tested by using a strong radioactive source and a film. An exposing time of several hours was sufficient to get a single picture of the internal geometry of the detector. The required time and the quality of this experiment were however not sufficient to be used for precise results.

For a better resolution our 4 detectors were analysed at the *Microfocus Computer Tomography* device of the *Department of Metallurgy and Materials Engineering* (MTM) at the *Katholieke Universiteit Leuven* (KUL).

A polychromatic X-ray source (Philips HOMX 161) operated at a voltage of 125 KV and a current of 0.28 mA filtered by a 2 mm aluminium and a 1 mm copper shield [12] was used for the experiment and is shown in figure 4.11. The data acquisition was realised through a CCD camera (Adimec MX12P) delivering 12 bits grey scale images at a resolution of 1024 x 1024 pixels, resulting in a voxel size of 110 - 150 μm. The detectors were placed on a rotating table and pictures were taken every 0.5°. The data were processed with the AEA Tomohawk software for 3D reconstruction.

With this configuration we were able to visualise the internal geometry of the detector. For the chosen beam energy, the detector cap was transparent, whereas the high density germanium crystal was not penetrated. Figure 4.12 shows the results of this expertise for the green detector. In this picture we can clearly recognise the germanium crystal held by an aluminium structure at the centre, surrounded by the detector cap. Knowing the precise dimensions of the cap, we were able to calibrate the experimental data and to determine the size of the crystal.

[5]Of course one could get the same effect by changing the source to detector distance. This one is however known very precisely and variations within the uncertainty limits could not be sufficient to take into account the excess of events found experimentally

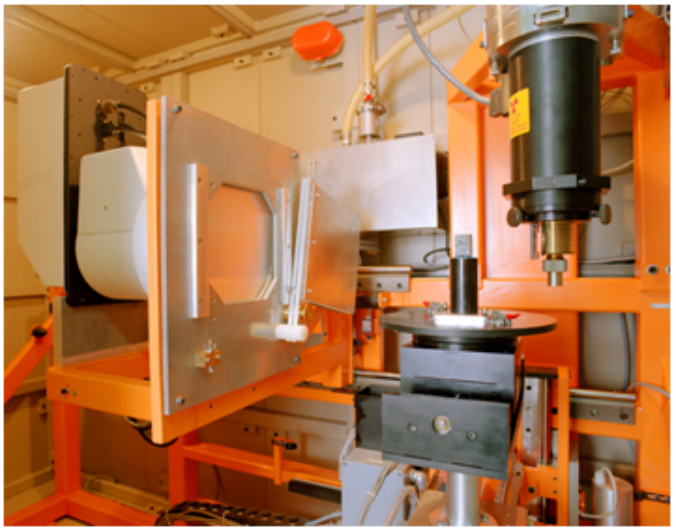

Figure 4.11: Philips HOMX 161 X-ray system used for the computed tomography of the detectors.

The black contours of the germanium crystal are due to the effect of *beam hardening*. This effect occurs in rather dense materials, where the softer X-rays (lower energy) are more strongly absorbed than the hard (higher energy) ones. This causes a loss in data resolution, which is however not significant for our purpose.

The results of this computed tomography are listed in table 4.5, together with the given dimensions and the Geant4 determined geometry. For the small crystals of the green and blue detectors we could prove that the diameter of the crystal was indeed a little smaller as the constructor specified. Moreover, the difficulties encountered in simulating the green detector could be explained by a wrong crystal to detector entrance window distance, which is in fact 3 mm longer than expected. The table shows that the values determined here are in good agreement with the simulation results performed by Geant4.

For the grey detector we also observed a slightly smaller crystal diameter. Nevertheless the results for the two larger crystals (the grey and the red ones) determined by this μ-ct analysis differ from the Geant4 best fit values by several mm on the diameter and a significant dead layer at the back of the crystal.

It could also be observed that the crystals are not always well centred in the detector cap and in certain cases tilted by 1 to 2°. Simulations showed that these parameters do not affect the efficiency results considerably and a correction for this effect was negligible.

4.2.3.4 Further investigations on the geometry

By performing the Microfocus Computer Tomography of the detectors, we were able to obtain a good agreement between the simulated geometries and the measured ones for the two small crystals. The large ones however still seem to be too big to fit the simulated data to the experimental values.

These results convinced the constructor for further investigations on the materials used

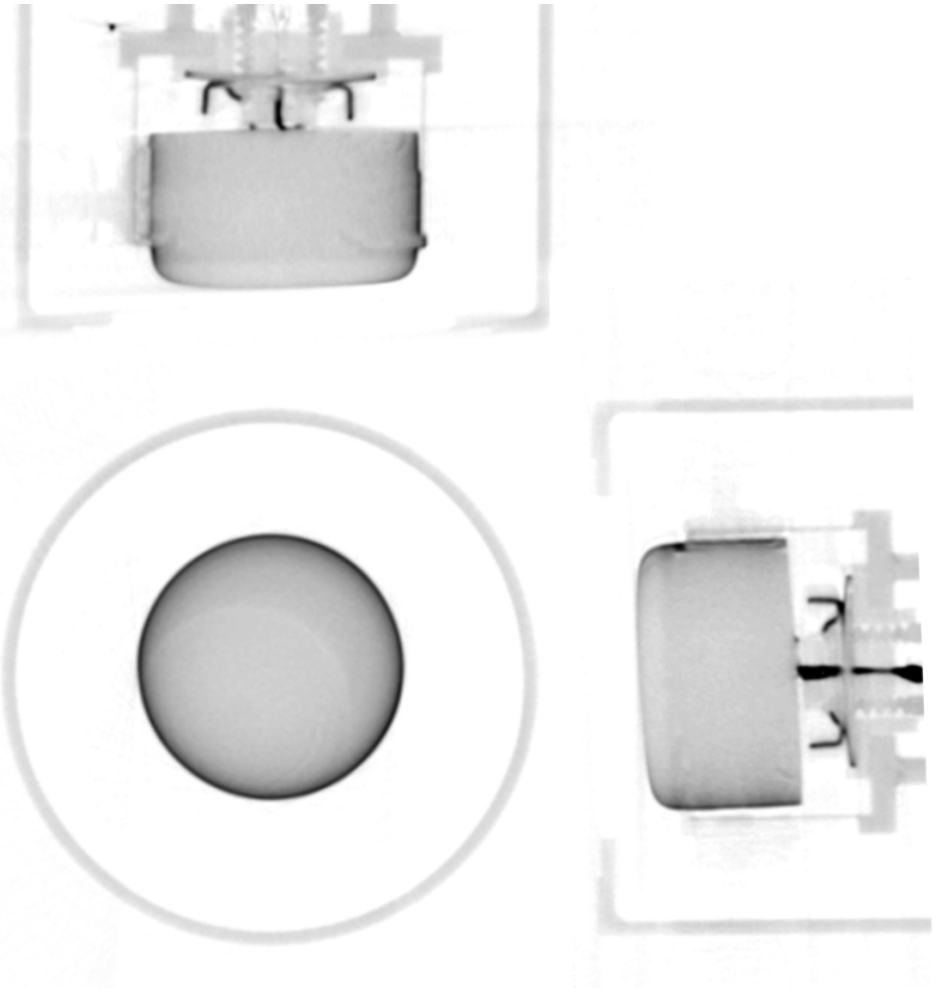

Figure 4.12: μ-ct analysis of the green detector, showing transaxial (bottom left), sagittal (bottom right) and coronal (top) views of the reconstructed data.

Detector	Component	Constructor Data	μ-ct Results	Geant4 best fit
Blue	Crystal Diameter	36.00	35.10	35.05
	Front Distance	5.00	4.50	5.00
	Rounding	3.00	2.80	3.00
	Thickness	19.60	19.60	19.60
	Back dead zone	-	-	0.40
Green	Crystal Diameter	35.50	34.80	34.70
	Front Distance	2.00	5.00	5.00
	Rounding	2.00	3.80	4.00
	Thickness	20.00	20.00	20.00
	Back dead zone	-	-	0.60
Red	Crystal Diameter	59.00	59.00	57.70
	Front Distance	5.00	5.00	5.00
	Rounding	5.00	5.00	5.00
	Thickness	27.50	27.50	27.50
	Back dead zone	-	-	2.30
Grey	Crystal Diameter	59.00	58.00	56.20
	Front Distance	5.00	4.50	5.00
	Rounding	5.00	5.00	5.00
	Thickness	30.00	30.00	30.00
	Back dead zone	-	-	1.40

Table 4.5: Dimensions of the different detector components expressed in mm for the 4 detectors used.

when the counters were built. More precise specifications, taking into account shrinking of the germanium crystal due to processing steps undergone during construction, were obtained. These new dimensions approach the results determined by the computed tomography for the green and blue detectors. Furthermore it was found that the grey crystal is in fact not a real planar detector, but rather a closed-ended coaxial detector. Due to its large size, a small hole was drilled into the germanium to ensure a good charge collection inside the crystal. This effect could not be observed by X-ray tomography, as the energies were too weak to penetrate the germanium. In fact, a γ-ray spectroscopy of the detectors would be necessary to show these bores.

Reducing the diameter of the crystal and removing germanium from the inside of the detector both lead to reducing the active volume and thus explain the differences observed in section 4.2.3.3. When considering the bores in the simulations the Geant4 values approach the determined outer crystal dimensions obtained above: for the grey detector, this hole is specified to be 16 mm deep with a diameter of 7 mm. To this has to be added the dead zone induced by the n^+ contact which is situated inside the bore. Considering a dead region of 1 mm, the final Geant4 best fit outer diameter of the crystal can be increased to 57.20 mm in the simulations, versus 58 mm measured.

For the red crystal however there still remain very large dead zones. A possible explanation for this could be the large size. As already mentioned in section 4.2.1, the detector may be completely depleted, but due to its large size the field in the semiconductor might be very weak in certain regions. The charges created here might not be collected fast enough to detect a pulse, and the regions can be considered as dead.

Concluding on the efforts made to determine a precise geometry we can say that our results on the dead zones are realistic. With these values we can simulate accurate efficiencies.

4.2.4 Efficiency results

The efficiencies were simulated with the best fitted detector geometries and dead zone sizes obtained from the discussions above and measurements were performed using different sources. The final experiment to simulation ratios of our calibration measurements are shown in figures 4.13, 4.14, 4.15 and 4.16. In total 7 measurement series have been performed. A ^{152}Eu point source was placed at the centre position of the sample, then displaced by 12 mm to the right, left, up and down. Two further measurements were realised with a ^{133}Ba point source and an extended ^{152}Eu source of 50 mm diameter at centre positions to check the previous results.

One can observe that the values obtained during the different measurement series all lie within a range of $\pm$ 2% with respect to the simulated values for the intermediate energy range (from 121.78 to 778.90 keV). For the low energy values, mainly the first point at 46 keV, the experimental values are differing a little more from the simulated ones. As these are in the X-ray domain, the influence of the environment is much more important and thus Compton scattering is much more considerable and errors are more easily introduced in the background subtraction procedure. The results for this domain are however sufficient for our needs.

The deviance between experimental and simulation data in the intermediate energy

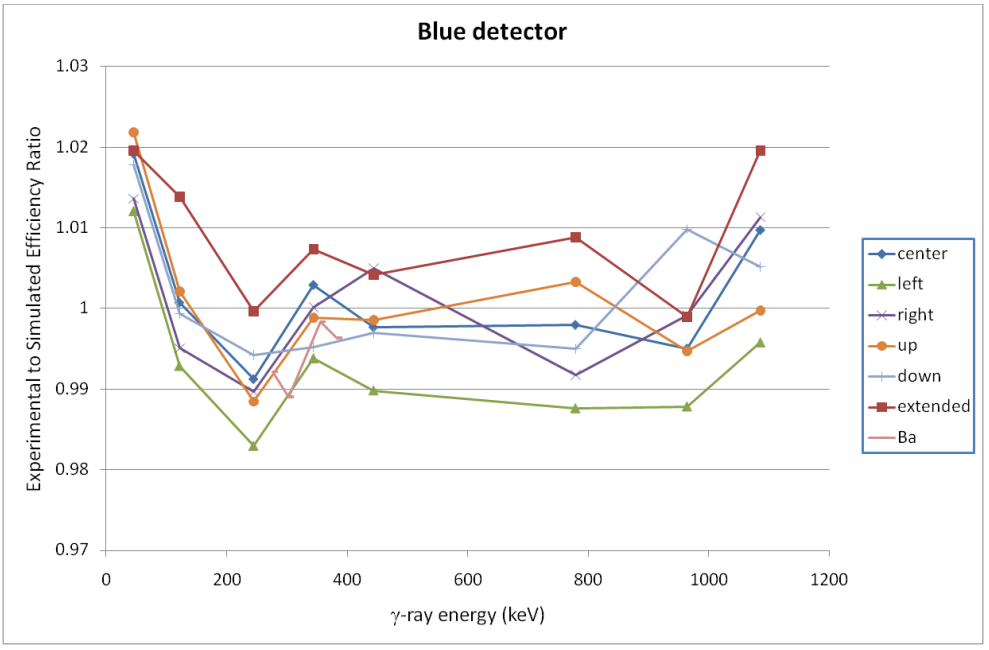

Figure 4.13: Experiment to simulation ratios for the efficiency calibrations for different source positions (see legend) of the blue detector.

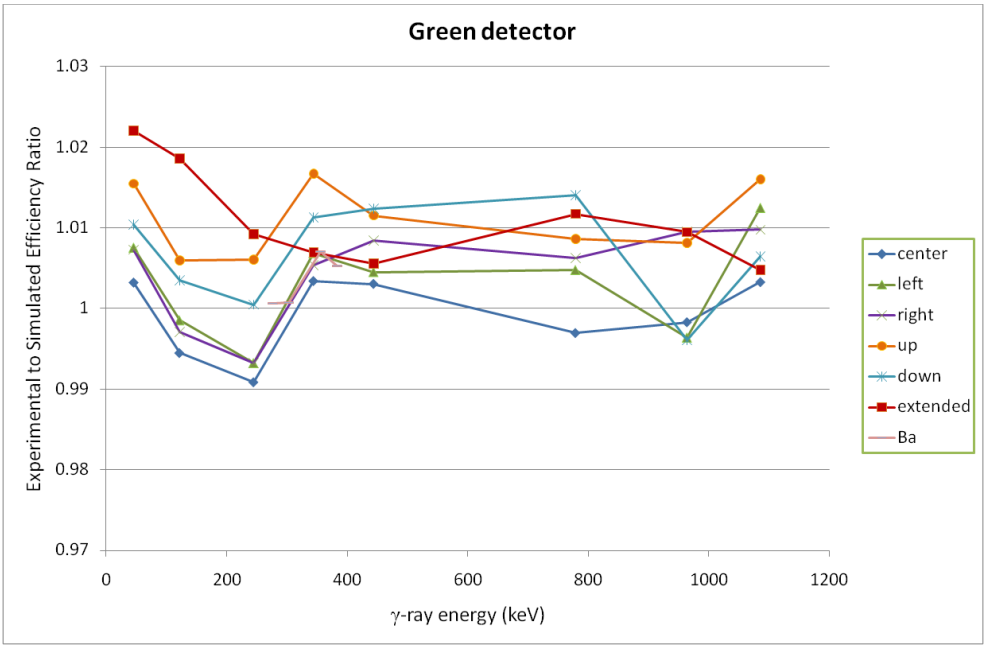

Figure 4.14: Experiment to simulation ratios for the efficiency calibrations for different source positions (see legend) of the green detector.

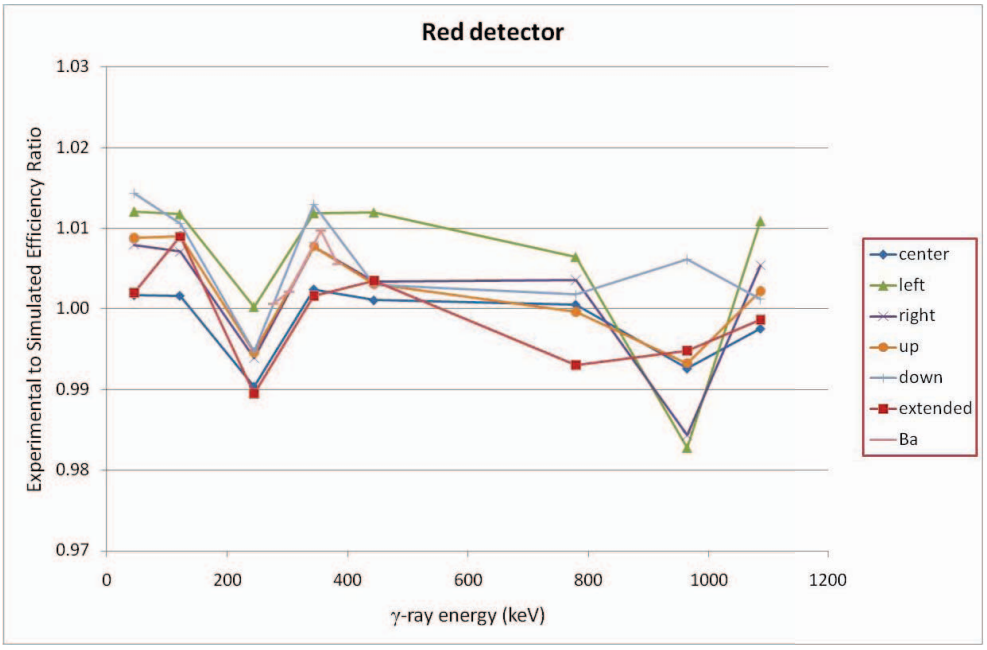

Figure 4.15: Experiment to simulation ratios for the efficiency calibrations for different source positions (see legend) of the red detector.

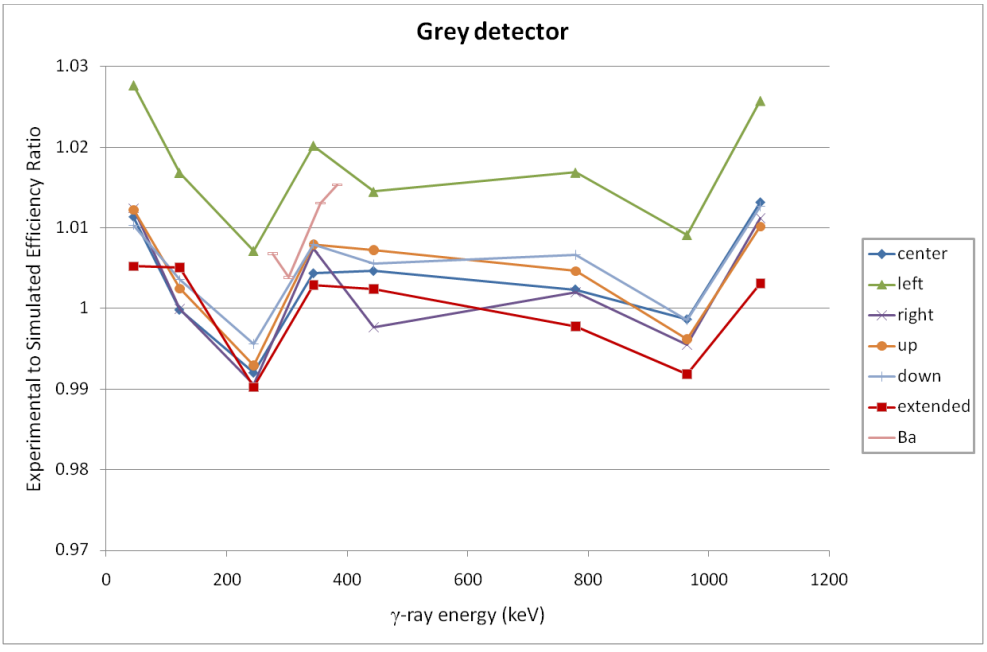

Figure 4.16: Experiment to simulation ratios for the efficiency calibrations for different source positions (see legend) of the grey detector.

domain can be explained by uncertainties on branching ratios and also by the fact that the simulations were only used to determine the peak efficiencies of the decays. The Compton scattering inside the detector was not considered, and might be subject to differences in the given yields of up to 1%. This is in particular the case for the 244.7 keV ray, which is systematically lower experimentally than in the simulated spectra.

The differences between the measured series are mainly due to the position precision of the source. This can be observed best for the green line, corresponding to the "left" position of the source. For the detectors grey and red it is overestimated experimentally, whereas the detectors blue and green are showing an underestimated value. In fact, the grey and red detectors are positioned to the right-hand side (RHS) of the experimental setup, as described in figure 3.5, and the blue and green ones to the left-hand side (LHS). As the experimental values are higher for the RHS placed detectors, this means that the source was placed too much to the right. This is confirmed by the fact that the outer detectors, i.e. the grey and the blue one, see a larger difference. Indeed as they are located at 110° they have a grazing angle to the target plane and a variation of the source position is seen more strongly as for the other detectors. Simulations show that a variation of 1% on this ratio of the grazing angle detectors corresponds to approximately 1 mm displacement.

4.2.5 Precision

The uncertainties on the final simulated efficiencies can be split into two different categories: On one hand there are the errors due to the calibrating source used, on the other hand are the systematic errors caused by the ignorance of certain simulation parameters.

Errors on the calibration source can be calculated using the well known propagation of uncertainty formula given in equation 5.7. The used calibration sources' data are given in table 4.4, their γ ray emission branching ratios in table 4.6. The computed error for the number of emitted rays during the calibration experiment take into account the uncertainties on the activity, the half-life of the considered isotope, the branching ratios of the different γ ray emissions and the statistical error due to the counting. The results are shown in the last column of table 4.6. These uncertainty values are considered the same for all the different experiments, as the same source was used and the experiment times were very similar.

On the other hand are the errors due to the uncertainty of simulation parameters and the positioning of the source. The first one includes the fact that certain parameters were neglected in the simulations, as only the photopeak was simulated. The error caused by the position of the source can be estimated by comparing the differences between the various experimental series. As already pointed out earlier, a displacement of 1 mm corresponds to a variation of 1% of the experiment to simulation ratio. Considering the simulated curves this error is estimated to 3% for energies below 100 keV and 1.5% for energies between 100 keV and 1 MeV. This leads to uncertainties ranging between 2 and 3% on the efficiency values computed. The respective errors on the used values for data analysis are given in appendix A.

E (keV)	Branching ratio p	Error on emitted particles
46.00[a]	14.95 ± 0.47	3.22 %
121.78	28.48 ± 0.13	0.85 %
244.70	7.53 ± 0.04	0.90 %
344.28	26.57 ± 0.11	0.83 %
443.97	3.13 ± 0.01	0.89 %
778.90	12.98 ± 0.06	0.88 %
964.06	14.64 ± 0.06	0.85 %
1085.84	11.87 ± 0.05	0.87 %

Table 4.6: ^{152}Eu branching ratios of the different γ ray emissions studied with their uncertainties [13] and the final uncertainty calculated on the number of particles emitted during the experiment.

[a]The 46 keV energy corresponds to the merged rays of the 45.4 and 46.6 keV decays

4.2.6 Conclusions

Thanks to the performed characterisation measurements, we were able to reproduce the measured efficiencies with the Geant4 simulation software. These simulations can compute efficiencies for the used samples in the (n,xnγ) experiment at precisions better than 3% in the desired energy range. The uncertainty achieved on the efficiencies will enable high precision measurements of cross sections.

Considering the dead zones used for the crystals it is noteworthy to observe that they are larger than specified by the constructor. This fact has already be observed by other independent studies, such as described in [14].

Bibliography

[1] G.F. Knoll, *Radiation detection and measurement*, 3^{rd} edition, John Wiley & Sons, New York, 2000

[2] J.-F. Berger, *La fission: De la phénoménologie à la théorie*, Ecole Joliot-Curie de Physique nucléaire 2006.

[3] V.S. Nikolayev, I.S. Dmitriev, *The equilibrium charge distribution in heavy element ion beams*, Physics Letters **28A**(1968)277.

[4] J.F. Ziegler, M.D. Ziegler, J.P. Biersack, *SRIM - The stopping and range of ions in matter*, Nuclear Instruments and Methods in Physics Research **B268** (2010), 1818-1823.

[5] C. Budtz-Jørgensen, H.-H. Knitter, G. Bortels, *Assaying of targets for nuclear measurements with a gridded ionization chamber*, Nuclear Instruments and Methods in Physics Research **A236** (1985), 630-640.

[6] G.W. Carlson, *The effect of fragment anisotropy on fission chamber efficiency*, Nuclear Instruments and Methods **119** (1974), 97-100.

[7] International Atomic Energy Agency, *Nuclear data standards for nuclear measurements*, Technical Reports Series **No. 227**, Vienna (1983).

[8] A. Plompen, C. Borcea, D. Deleanu, P. Dessagne, M. Kerveno, M. Mosconi, N. Nankov, A. Negret, R. Nolte, C. Rouki, G. Rudolf, M. Stanoiu, J.C. Thiry, *Method developing and testing for inelastic scattering measurements at the GELINA facility*, Proceedings of the International Conference on Nuclear Data for Science and Technology, Apr. 26-30, 2010, Jeju, Korea.

[9] J. Allison et al, *Geant4 - A simulation toolkit*, Nuclear Instruments and Methods in Physics Research **A506** (2003), 250-303.

[10] MCNPX, online: https://mcnpx.lanl.gov/

[11] D. Deleanu, C. Borcea, Ph. Dessagne, M. Kerveno, A. Negret, A.J.M. Plompen, J.C. Thiry, *The gamma efficiency of the GAINS spectrometer*, Nuclear Instruments and Methods in Physics Research Section A, in preparation.

[12] G. Kerckhofs et al., *Validation of x-ray microfocus computed tomography as an imaging tool for porous structures*, Review of Scientific Instruments **79(1)** (2008), 1-9.

[13] Physikalisch-Technische Bundesanstalt, *Empfohlene Radionukliddaten*, Stand 1.07.1993, Braunschweig und Berlin.

[14] J.C. Hardy, V.E. Iacob, M. Sanchez-Vega, R.T. Effinger, P. Lipnik, V.E. Mayes, D.K. Willis, R.G. Helmer, *Precise efficiency calibration of an HPGe detector: source measurements and Monte Carlo calculations with sub-percent precision*, Applied Radiation and Isotopes **56** (2002) 65-69.

Chapter 5

Results and Discussion

This chapter is dedicated to the final results that have been obtained with the work described in the previous chapters. In the first part, the data analysis methods which have been applied to extract the ingredients of interest are presented along with the methods used to compute the uncertainties. One separate section is dedicated to the determination of the neutron flux as this is a very important factor in the calculations. After these introductory paragraphs the results that have been obtained on the ^{235}U and the ^{232}Th isotopes are presented and compared to theoretical predictions.

5.1 Data analysis algorithms

This section presents the different steps in the data analysis which are followed to get from the raw data, acquired with the experimental setup, to the final cross sections. A good understanding of these procedures is mandatory to understand the error sources affecting the final data.

5.1.1 Determination of the number of γ rays in the spectra

As already presented in chapter 3, the data acquired on the germanium counters is stored in list mode files, where the time-of-flight and energy information of each event is kept. The first part of the analysis consists in determining the appropriate time-of-flight window widths to be used as a gate to generate γ energy spectra. Depending on the counting statistics of events of interest, the choice of this gate is a compromise between a sufficient number of counts to reduce the error on the counting and the best time-of-flight and thus neutron energy resolution. Due to the dependence on the counting statistics, the binning of the time spectra is conditioned by the individual γ rays observed as well as by the energy domain studied, and varies from case to case.

Once the binning is chosen, the energy spectra are generated and calibrated using the known radioactivity rays of the selected isotope or, when missing, by a spectra obtained with a calibrated source and the energy rays of interest are identified. An example of such a ray is shown in figure 5.1. The background subtraction is realised through a linear fit. Two windows next to the peak of interest are chosen for which the average background

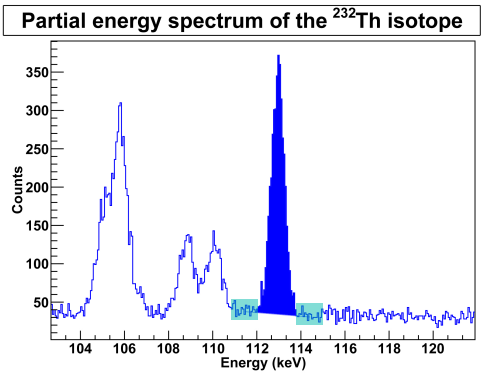

Figure 5.1: Background subtraction example on the 112.75 keV γ ray of the ^{232}Th isotope.

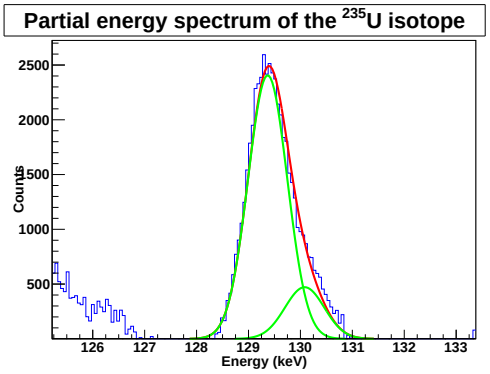

Figure 5.2: Double Gaussian fit example on the 129.30 keV γ ray of the ^{235}U isotope.

is estimated. These both mean values are then used to fit the background locally with a simple linear function. Once this line is determined, the number of counts above is integrated and represents the number of hits detected in the peak n_{det}.

In certain cases the ray of interest may be mixed with another ray, due to the finite detection resolution of the HPGe counters. In these cases a double Gaussian fit is performed on the energy spectra to disentangle the two different rays, after the background has been subtracted. An example of such a procedure is shown in figure 5.2 where the 129.30 keV γ ray identifying an inelastic scattering reaction on ^{235}U is mixed with a background γ ray. The two green curves represent the final fit of the two different Gaussian functions whereas the red curve is the sum of both, describing thus the observed spectrum locally. In this case the integration of the distribution of interest yields the number of hits detected in the peak n_{det}.

The latter number does not represent the final result, as the detection is affected by a large dead time, especially for neutrons close to the γ flash. The dead time monitoring is performed by observing radioactivity rays of the isotope all along the neutron energy domain which are compared to off-beam radioactivity yields. The latter ones are corrected

for acquisition dead time, due to constant background counting. This procedure allows us to define a correction factor λ to be applied on the counted number of events n_{det} to obtain the final detection yield n for each detector (see also section 3.2.5.3):

$$n = \lambda \cdot n_{det} \tag{5.1}$$

5.1.2 γ production and transition cross sections

After the determination of the number of detections and correction for dead time for each detector, the γ production cross sections can be computed for the different angles and the angle differential cross sections in this case are given by:

$$\frac{\mathrm{d}\,\sigma}{\mathrm{d}\,\Omega}(\theta_i) = \frac{1}{4\pi}\frac{n_\gamma(\theta_i)}{N_{targets}\cdot\Phi} \tag{5.2}$$

where θ_i indicates the measured angle, Φ corresponds to the incident neutron flux integrated for the considered neutron energy domain and n_γ is the number of γ rays emitted towards the defined angle. It corresponds thus to the pile-up corrected number of hits n measured as explained in the section above corrected for the detection efficiency ϵ. If there are j detectors observing the same angle, in our case $j = 2$, it corresponds to the sum

$$n_\gamma = \frac{\sum_j n_j}{\sum_j \epsilon_j} \tag{5.3}$$

Of course one could use all the detectors separately, but summing the detectors observing the same angle will be particular useful in the uncertainty calculation following in the next section.

The number of target nuclei $N_{targets}$ can be obtained by:

$$N_{targets} = \frac{\varsigma \cdot \mathcal{N}_\mathcal{A} \cdot p}{M_A} \tag{5.4}$$

where ς is the areal density of atoms in the target, $\mathcal{N}_\mathcal{A}$ the Avogadro number, p the isotopic purity of the sample and M_A the atomic mass of the isotope of interest.

With our detectors positioned at angles of 110° and 149°, we can use the equations (2.12) and (5.2) and express the total angle-integrated γ production cross section as:

$$\sigma = \frac{0.6521\cdot n_\gamma(110°) + 0.3479\cdot n_\gamma(149°)}{N_{targets}\cdot\Phi} \tag{5.5}$$

This one can be conveniently transformed into the *transition cross section* $\sigma_{transition}$, by applying the correction for internal conversion, as presented in section 2.1.4.3:

$$\sigma_{transition} = \sigma\cdot(1+\alpha_{IC}) \tag{5.6}$$

It corresponds to the probability of observing a transition characterised by the emission of a given γ ray.

5.1.3 Error calculus

The uncertainty on the cross section values can be split in two different categories: statistical errors on the event counting and systematic errors on the different ingredients presented above, used to compute the final cross section.

A first error estimation has to be made on the number of γ rays measured n. In fact, this quantity is affected by a pure statistical error on the number of detected events n_{det} and a systematic error on the correction factor λ. The error on the different n_j can be obtained by applying the well-known formula for propagation of uncertainty. Indeed, this formula says that for a multivariable function $\varphi = \varphi(x_1, x_2, ..., x_n)$, the uncertainty on φ is given by:

$$\Delta\varphi = \sqrt{\sum_{i=1}^{n} \left(\frac{\partial\varphi}{\partial x_i} \Delta x_i \right)^2} \tag{5.7}$$

The errors on the n_j can thus be computed as:

$$\left(\frac{\Delta n_j}{n_j} \right)^2 = \left(\frac{\sqrt{n_{det}}}{n_{det}} \right)^2 + \left(\frac{\Delta\lambda}{\lambda} \right)^2 \tag{5.8}$$

In the next step we have to calculate the error on the summation of the different n_j values from the j detectors used. To achieve this we assume that the error is dominated by the counting uncertainty and is thus ruled by a Poisson law, for which the uncertainty is given by the square root of the mean value. For this purpose we define *effective number of events* n_{eff_j} [1, 2] by:

$$\frac{\sqrt{n_{eff_j}}}{n_{eff_j}} = \frac{\Delta n_j}{n_j} \tag{5.9}$$

for each detector j. It is important to note that this effective value does not represent any physical quantity, it is just a fictive number whose relative error has the same behaviour as pure counting errors. The total relative error on the sum of the different detector events is then given by:

$$\frac{\Delta\left(\sum_j n_j\right)}{\sum_j n_j} = \frac{\sqrt{\sum_j n_{eff_j}}}{\sum_j n_{eff_j}} \tag{5.10}$$

The uncertainty on the different detector efficiencies ϵ_j are independent and are hence summed using equation (5.7). This results in a total error on n_γ of:

$$\left(\frac{\Delta n_\gamma}{n_\gamma} \right)^2 = \left(\frac{\Delta\left(\sum_j n_j\right)}{\sum_j n_j} \right)^2 + \left(\frac{\Delta\epsilon}{\epsilon} \right)^2 \tag{5.11}$$

where $\Delta\epsilon$ is given by:

$$\Delta\epsilon = \sqrt{\sum_j (\Delta\epsilon_j)^2} \tag{5.12}$$

The error on the remaining ingredients are all systematic errors and follow Gaussian statistics. The final error on the γ ray production cross section is therefore obtained by applying again formula (5.7):

$$\frac{\Delta\sigma}{\sigma} = \sqrt{\left(\frac{\Delta n_\gamma(110°)}{n_\gamma(110°)}\right)^2 + \left(\frac{\Delta n_\gamma(149°)}{n_\gamma(149°)}\right)^2 + \left(\frac{\Delta N_{targets}}{N_{targets}}\right)^2 + \left(\frac{\Delta\Phi}{\Phi}\right)^2} \tag{5.13}$$

5.2 Incident neutron flux determination

A very important factor in the cross section evaluation is the determination of the incident neutron flux. As already mentioned in chapter 3 and elaborated in chapter 4, this is done with a fission chamber, mounted upstream of the sample of interest in the experimental setup. The flux is measured continuously with every measurement campaign, in order to be able to calculate the exact neutron fluence for each experimental run and to take into account possible power variations of the accelerator.

Similarly as for the HPGe detectors the acquired data is gated on the time-of-flight spectrum in order to obtain an energy dependent flux. For these bins, the amplitude spectra are integrated above threshold to obtain the number of detections. As the neutron flux is not supposed to have much structure, these gates can be chosen large enough to obtain a high number of events and thus reduce the statistical error. As the flight distance to the fission chamber is different from the distance of the sample, we compute the differential neutron flux $\frac{\mathrm{d}\Phi}{\mathrm{d}E}$. This quantity is then integrated over the energy gates chosen on the γ spectra to obtain the exact flux for the chosen gating.

The overall incident neutron flux Φ is given by

$$\Phi = \frac{n_{det}}{\varsigma\sigma_f\epsilon} \tag{5.14}$$

where:

Φ	integrated neutron flux (no dimensions)
n_{det}	number of detections above threshold
ς	areal density of uranium atoms in the deposit (see table 4.2) (in cm^{-2})
σ_f	fission cross section ^{235}U(n,f) (in cm^2), ENDF/B-VII.0
ϵ	fission chamber efficiency as determined in chapter 4

As the flux is determined for each separate experimental run, we work with the time integrated neutron flux. For this reason the flux computed here is dimensionless, and simply corresponds to the number of incident neutrons per run. Figure 5.3 shows a typical differential neutron flux measured at the flight cabin FP16/30 at GELINA.

After the calculation of this neutron flux, one more correction has to be considered. In fact, the flux is measured 1.56 m before the sample is hit. The neutrons counted in the fission chamber will suffer from attenuation in the remaining part of the fission chamber, but mostly in the air before the sample. To take these effects into account, MCNPX[1] simulations were performed and a mean attenuation of 1.8% was computed on

[1]The MCNPX version used for the attenuation measurements in this work was version 2.6d

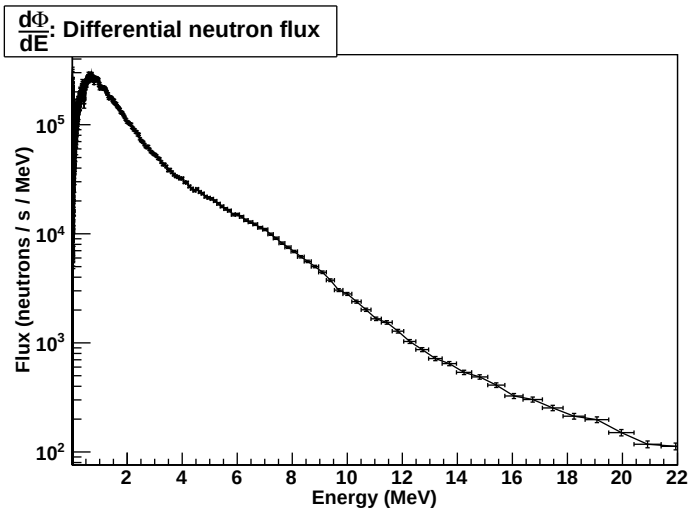

Figure 5.3: Differential neutron flux measured at FP16/30 at GELINA.

the neutron flux depending on the energy. The measured neutron flux has thus to be diminished by 1.8% to take into account the effective neutron yield hitting the sample.

Considering the uncertainties on the different ingredients of 0.3% on the areal density of nuclei in the deposit, 2.1% on the fission chamber efficiency, up to 1% on the fission cross section given by ENDF/B-VII.0, 1.5% on the air attenuation coefficient and less than 1% on the counting statistics, the error on the flux computed for the experiment using formula 5.7 is 2.9% in the high energy domain, where the fission cross section has the highest uncertainty, and goes down to 2.3% in the 1-2 MeV neutron energy region, where the error on the fission cross section is 0.5% and the statistics very high as the flux is highest here.

5.3 The ^{235}U isotope

In the following section the results of the measurement campaign on the ^{235}U isotope which has been performed at GELINA are presented. The data discussed here have been acquired in an experiment with a run time of 1248 hours. In the upcoming paragraphs the results of the neutron inelastic scattering and (n,2n) reaction measurements are presented after a brief introduction into the technical specifications of the used sample.

The γ strength functions predicted by the TALYS code for the ^{235}U isotope were computed by Pascal Romain [7] from the *Commissariat à l'énergie atomique (CEA), Bruyères-le-Châtel, France*. The CEA developed a significant database of parameters fitting all the decay channels of the fissile ^{235}U in order to be able to simulate the reaction cross section yields of interest.

^{235}U sample	Purity	93.18%	
	Atomic mass	235.043923 g/mol	
	Total mass	37.43 g	± 0.01 g
	Surface	113.173 cm^2	
	Thickness	0.211 mm	± 0.006 mm (Stdev)
	Density	15.67 g/cm^3	
	Areal Density	0.330 g/cm^2	± 0.009 g/cm^2

Table 5.1: Specifications of the ^{235}U sample used for the experiments.

5.3.1 Source specifications

As already mentioned in chapter 3, the sample used for the experiment must be rather thin to avoid γ ray auto-absorption inside the foil. For this reason we choose a circular sample of a diameter of 120 mm. As the beam diameter is only 55 mm, the outer part of the source has been shielded with lead to avoid too important counting rates caused by the natural radioactivity of uranium. The thickness of the sample is 0.211 mm with an uncertainty of 0.006 mm. The error on the thickness corresponds to the standard deviation obtained on a set of 18 measurements at different spots of the deposit. Further specifications are given in table 5.1.

5.3.2 Integral energy spectrum

The energy spectra that were acquired with the ^{235}U sample are shown in appendix B, where time gates were chosen for radioactivity, for neutrons from 1 to 6 MeV representing the inelastic scattering domain and a window for neutrons of 8.5 to 16 MeV which corresponds to the domain of (n,2n) reactions. The energy rays witnessing inelastic scattering are shown in green, the ones coming from (n,2n) reactions are displayed in red.

It is noteworthy to mention here that the spectrum observed contains a very large number of weak γ yields, which are due to the decay of fission products created through (n,f) reactions. As they are very numerous it was not possible to identify all of them clearly. Nevertheless some were identified and are listed together with the other energy rays of interest in table B.1. The spectra shown stop at a γ energy of 380 keV, as the counting statistics are getting low beyond this point, and a precise cross section extraction gets impossible. Indeed, the small HPGe crystals used in this experiment do not have a sufficient efficiency at these high energy values to obtain high counting rates.

The dead time correction coefficient λ was obtained thanks to the 185.7 keV γ ray of the ^{231}Th isotope created after an α emission from ^{235}U.

5.3.3 ^{235}U neutron inelastic scattering cross sections

Inelastic scattering reactions leave the target nucleus in an excited state if the neutron energy is higher than the reaction threshold. The deexciting of the nucleus to its ground state (GS) is realised by a γ ray emission characteristic of the studied nucleus. Figure 5.4(a) shows the low energy levels of the ^{235}U isotope, including the GS band as

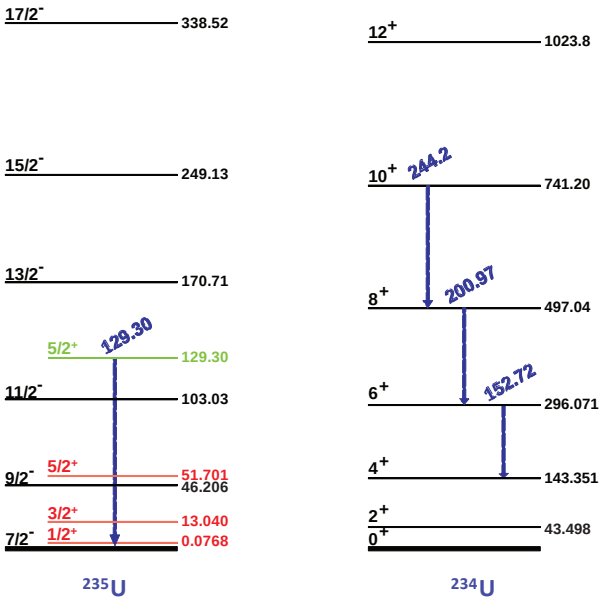

(a) (b)

Figure 5.4: Partial level scheme of ^{235}U showing the GS band in black, and two other bands in green and red (left) and of the ^{234}U GS band (right). The studied transitions are shown in blue. All the energies are expressed in keV.

well as two rotational bands. This section studies the γ decays which we were able to observe with our experimental setup. As the energy spectra in figure B.1 show, there are several rays observable which are due to (n,n') reactions, but unfortunately the spectra are strongly contaminated by γ radiation emitted by the fission products and by the background activity of the sample, so that finally the 129.30 keV decay between the $\frac{5}{2}^+$ and $\frac{7}{2}^-$ states was the only γ ray that could be analysed.

5.3.3.1 $\frac{5}{2}^+ \rightarrow \frac{7}{2}^-$ (GS) transition in ^{235}U

The decay of the $\frac{5}{2}^+$ state with energy 129.30 keV to the $\frac{7}{2}^-$ ground state is realised through the emission of a γ ray of 129.30 keV. As the transition goes to the ground state the energy threshold of the transition equals the energy of the emitted γ ray. The multipolarity of the transition can be computed as described in section 2.1.4.1 and is thus an electric dipole (E1) transition. The internal conversion coefficient for this type of γ ray in ^{235}U at this energy is $\alpha_{IC} = 0.275$.

The γ ray of 129.30 keV in the energy spectra is mixed with another ray located around energy 130.2 keV. The latter one is present in the entire neutron domain and is probably emitted by a fission product after a neutron induced fission reaction. Possible candidates for this ray include the 130.20 keV γ decay of ^{99}Zr or the 130.24 keV γ decay of ^{134}Cs. To disentangle both rays a double Gaussian fit has been applied as explained

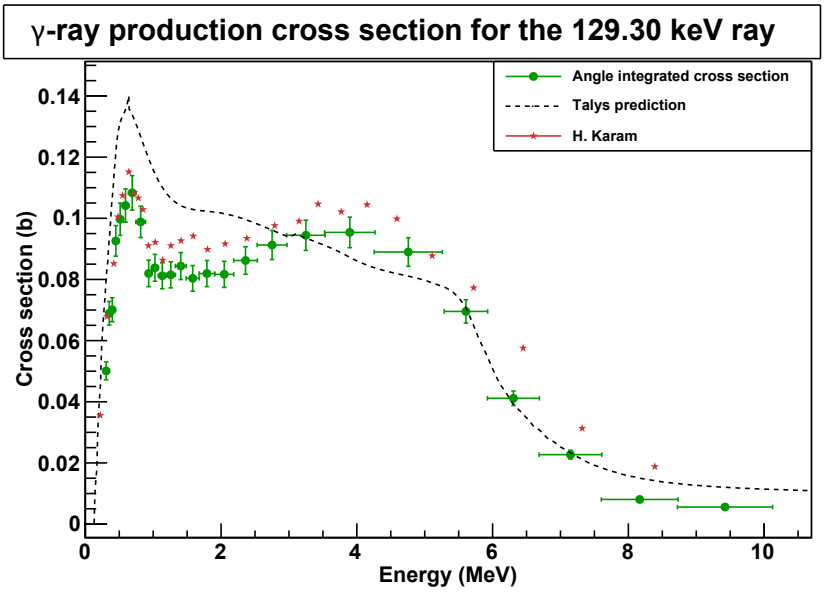

Figure 5.5: Total γ production cross section of the 129.30 keV transition from states $\frac{5}{2}^+ \rightarrow \frac{7}{2}^-$ due to a ^{235}U(n,n')^{235}U reaction compared to TALYS predictions.

in the data extraction algorithms section. After this procedure a total yield of 178340 counts is determined for the four detectors in the total integrated energy spectrum. These statistics allowed us to chose a binning of 26 different gates to evaluate the cross sections, thus leading to an evaluation at 26 different energy values. The analysis results of the total angle integrated cross section are shown in figure 5.5, the yields of the single detectors is represented in figure C.1 and the extracted data point values are listed in table C.1.

From the threshold to the peak of the direct excitation of the $\frac{5}{2}^+$ state around 1 MeV the shape of the measured cross section agrees with the TALYS predictions, although a general amplitude difference of almost 25% can be observed. After this direct excitation compound the shapes of both curves diverge. While the TALYS code predicts a decrease of the γ production cross section, our measurements show an increasing hump before both curves describe the same final descending part. The results of these measurements agree within 8% with measurements that have been performed by H. Karam et al. [8] during a first campaign. The difference observed can be explained by the fact that the γ detection efficiencies used by H. Karam et al. were not calculated so precisely than these in this work, as internal structure data of the detectors were missing at that time. Indeed, a comparison between both values shows that the new ones are 8% higher, thus leading to an 8% lower cross section.

The uncertainties of the experiment are below 6% for energies smaller than 7 MeV and increase up to 12% for the three high energy points, since the statistics are becoming weaker as the cross section is getting lower. This corresponds to the best precision obtained on the measurement of the 129.30 keV γ decay of an inelastic scattering cross section and is a significant improvement compared to a first measurement campaign performed by

H. Karam et al.

5.3.4 ^{235}U(n,2n) reaction cross sections

After a (n,2n) reaction on ^{235}U, the residual ^{234}U nucleus is produced and for energies above the threshold of this reaction the resulting ^{234}U is left in an excited state. The nucleus will decay to its ground state (GS) through the emission of characteristic γ rays. A partial level scheme of the ground state band showing its different energy levels is shown in figure 5.4(b). In this section the γ decays between the states 10^+ to 4^+ with energies of 152.72, 200.97 and 244.2 keV are extracted and studied.

5.3.4.1 $6^+ \rightarrow 4^+$ transition in ^{234}U

The decay between the states 6^+ (E = 296.07 keV) to 4^+ (E = 143.35 keV) in ^{234}U is realised through a γ ray emission of 152.72 keV. The threshold of this reaction corresponds to the neutron separation energy of ^{235}U and the required residual energy to leave the ^{234}U nucleus in the 6^+ excited state. For this ray the energy threshold is 5.62 MeV. The multipolarity of the γ ray is E2 and it has an internal conversion coefficient of $\alpha_{IC} = 2.14$.

Summing the four detectors, a total counting of 28071 is obtained, which allowed to select 13 neutron energy intervals to evaluate the reaction cross section. The final total cross section for this transition is displayed in figure 5.6 together with the TALYS code predictions and other measurements performed by A. Hutcheson et al. [5] and D.P. McNabb et al. [6]. The separate detector output is shown in figure C.2 and the final data points are given in table C.2.

On one hand, the differences from the work of H. Karam et al. can be explained similarly as those for the 129.30 keV γ ray analysed above. The efficiencies of the HPGe detectors used in that work were roughly 15% lower than the new optimised ones, yielding thus a higher cross section. Taking this into account, the results of both works agree very well.

On the other hand, one can observe that the results found by our measurements are by a factor 2.2 lower than the results predicted by TALYS. Furthermore the TALYS code seems in a rather good agreement with the measured points of A. Hutcheson et al. and D.P. McNabb et al. It is however noteworthy to mention that the data of D.P. McNabb et al. have been scaled by an unknown correction factor according to [6], indicating that his results must be considered with extreme caution. When comparing our data points to the scaled TALYS γ production cross section, we can observe an excellent agreement in the shape of both curves, despite the fact that the theoretical predictions descend a little later than the experimental points.

After all, the results obtained in this work agree with the ones of H. Karam et al., considering the efficiency difference. The fact that these both campaigns for which the experimental setup was changed partially and where different ^{235}U samples were used speaks in favour of our measurements. Together with the experimental determination of the fission chamber efficiency as well as the simulations of the HPGe efficiencies in this work and the exclusion of different systematic error sources by H. Karam et al. such as acquisition dead time and flux variances the results seem very reliable.

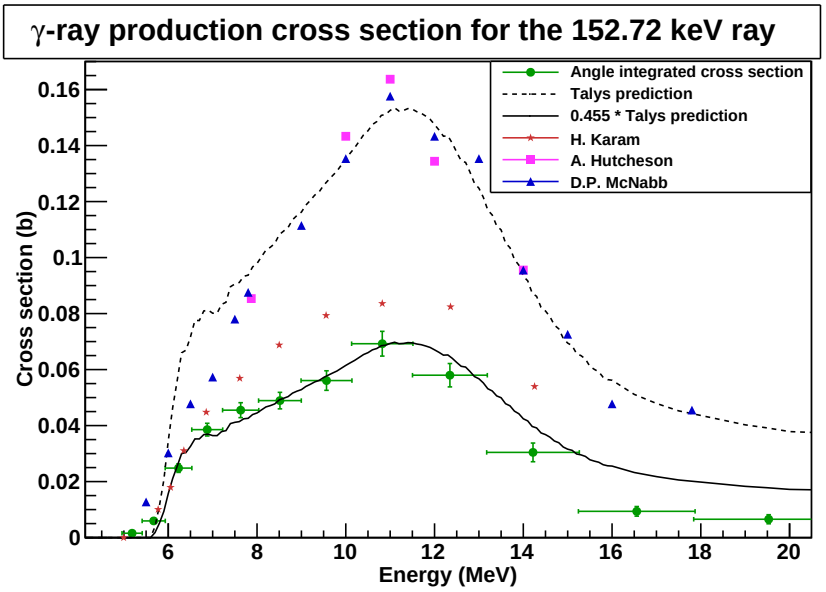

Figure 5.6: Total γ production cross section of the 152.72 keV transition from states $6^+ \rightarrow 4^+$ due to a ^{235}U(n,2n)^{234}U reaction compared to TALYS predictions and other experimental measurements.

The uncertainties corresponding to the evaluated data are below 7% in the energy domain between 6 and 12 MeV. Near the threshold and the descending part of the cross section they are however higher, caused by the lack of statistics in these ranges.

5.3.4.2 $8^+ \rightarrow 6^+$ transition in ^{234}U

The transition between the two energy levels 8^+ at 497.04 keV and 6^+ at 296.07 keV in the ^{234}U isotope can be observed by the detection of a γ ray of 200.97 keV. The reaction threshold for this (n,2n) reaction followed by a 200.97 keV γ decay is 5.82 MeV. The multipolarity of the transition is E2 and its internal conversion coefficient is $\alpha_{IC} = 0.734$.

The 200.97 keV γ ray is mixed with the 202.11 keV ^{235}U radioactivity ray in the energy spectra. For the grey and green detectors it was possible to distinguish both rays due to higher count rates and a good resolution of these detectors. For the red detector the resolution was however not sufficient and the counting statistics of the blue detector were too weak to obtain reliable results in disentangling both contributions. The analysis of this transition is therefore based on the green and grey detectors only, for which a counting of 13071 was obtained enabling an evaluation of the cross section at 11 energy points. The angle integrated cross section is shown in figure 5.7, the attached data points are tabulated in table C.3 and the two angle dependent yields are drawn in figure C.3.

Except the measurement of H. Karam et al., this ray has never been observed experimentally as the experiment of A. Hutcheson et al. was not able to disentangle the 200.97 and 202.11 keV rays. For this transition the cross section yields of H. Karam et al. are located below the newly determined ones. For this energy the detection efficiency used by

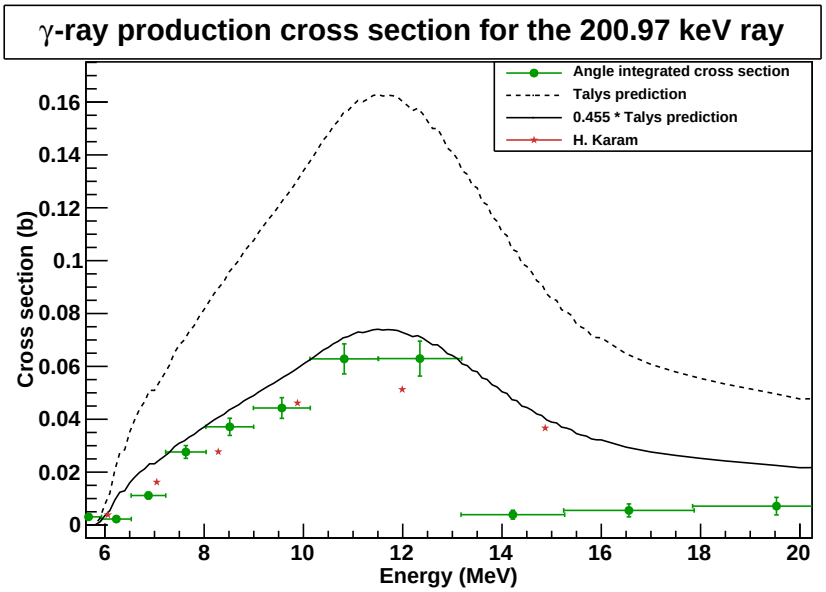

Figure 5.7: Total γ production cross section of the 200.97 keV transition from states $8^+ \rightarrow 6^+$ due to a ^{235}U(n,2n)^{234}U reaction compared to TALYS predictions and prior measurements.

H. Karam et al. is very close to the ones obtained in this work. The reason why his γ production cross section is a little weaker is related to the lower statistics of his measurements and hence the larger error committed on the Gaussian fitting of the two combined energy rays.

We can also observe that the shape of the cross section is very close to the one predicted by TALYS, although its amplitude is again approximately by a factor 2.2 lower, similarly than the 152.72 keV transition cross section.

Analogously as for the previous transition, the errors are below 7% in the energy domain from 6 to 12 MeV, and higher in the low and high energy regions, where the counting is reduced due to the weaker transition probability.

5.3.4.3 $10^+ \rightarrow 8^+$ transition in ^{234}U

The emission of a 244.2 keV γ ray witnesses a decay from the 10^+ to 8^+ state of energies 741.20 and 497.04 keV respectively in ^{234}U. The threshold for such a γ ray to be observable after an (n,2n) reaction is 6.06 MeV. This transition is an electric transition of second order (E2) and its internal conversion coefficient is $\alpha_{IC} = 0.367$.

A total number of 10049 counts was obtained for this energy ray on the green and grey detectors. While this energy peak could be integrated straightforwardly without Gaussian fit, the statistics of the red and blue detector were too low to deliver acceptable results. The cross section has been evaluated at 10 neutron energy points as shown for the total angle integrated cross section in figure 5.8 and the angle dependent one in figure C.4. The data values are listed in table C.4.

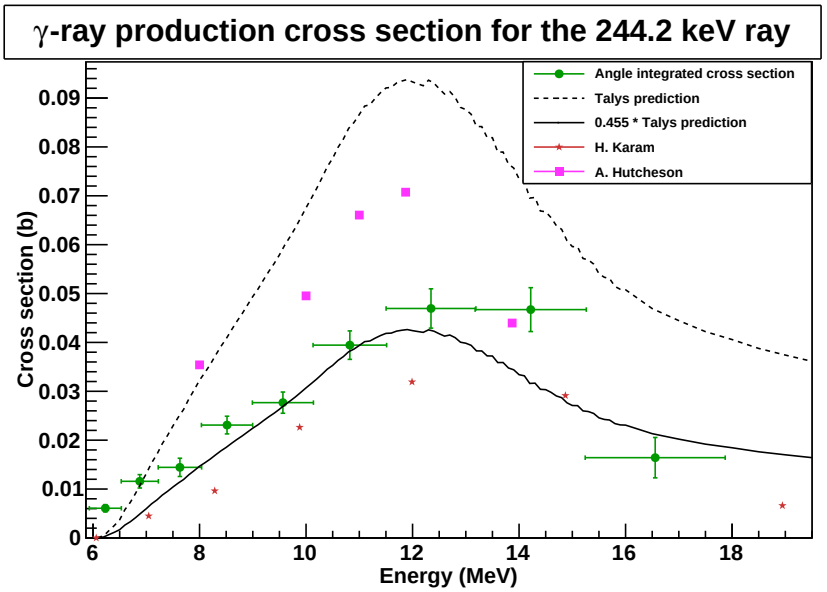

Figure 5.8: Total γ production cross section of the 244.2 keV transition from states $10^+ \rightarrow 8^+$ due to a ^{235}U(n,2n)^{234}U reaction compared to TALYS predictions and other experimental measurements.

While an analogue difference between the prior work of H. Karam et al. and these new measurements can be observed and explained by the same arguments than earlier, our new measurements follow the TALYS prediction curve corrected by the same factor 2.2 as for the previous measurements. The difference between the measurement of A. Hutcheson et al. [5] and our data has decreased from a factor of nearly 2.2 observed for the 152.72 keV γ ray to a factor 1.5 for this energy ray.

This cross section has been determined with very low counting statistics. For this reason its precision does not drop below 11% in the maximum amplitude region of the excitation curve and it reaches values of 37.7% for the point at 16.6 MeV. This is entirely caused by the low statistics of the detection. In order to obtain better precisions for this transition and other ones of higher energy, larger runtimes for the experiment must be considered.

5.4 The ^{232}Th isotope

This section treats the measurement campaign which has been made at GELINA to probe (n,xnγ) reactions on ^{232}Th. Despite a low neutron flux above 15 MeV, we were able to extract cross sections of reactions up to (n,3n). All the data analysed below has been acquired within an experimental run time of 375 hours. Different γ ray decays which have never been measured before were observed during this experiment. After a brief presentation of the technical specifications of the used sample and the energy spectra that have been obtained, the results of this campaign are presented in the following sections

^{232}Th sample	Purity	99.5%	
	Atomic mass	232.038050 g/mol	
	Total mass	11.9939 g	± 0.0001 g
	Surface	36.463 cm^2	
	Thickness	0.302 mm	± 0.004 mm (Stdev)
	Density	10.894 g/cm^3	
	Areal Density	0.329 g/cm^2	± 0.004 g/cm^2

Table 5.2: Specifications of the ^{232}Th sample used for the experiments.

and discussed along with theoretical predictions.

The theoretical γ production cross sections were computed by the TALYS code. The calculations for the ^{232}Th cross sections were performed by Arjan Koning from the *Nuclear Research and Consultancy Group (NRG), Petten, The Netherlands*, one of the authors of the code, as a special parameterisation was needed for this isotope which is not included in TALYS by default.

5.4.1 Source specifications

Alike the ^{235}U sample, the ^{232}Th deposit must be thin enough to avoid γ ray auto-absorption inside the foil. For the ^{232}Th measurement campaign, we choose a rectangular sample of dimensions 60x60 mm, large enough to be completely exposed to the beam and of thickness 0.302 mm. The exact specifications are given in table 5.2.

5.4.2 Integral energy spectrum

The energy spectra obtained with our experimental setup are presented in appendix B. Similarly as for the ^{235}U sample, time gates are shown for radioactivity, inelastic scattering and (n,2n) neutron energy ranges. The (n,n') caused γ rays are shown in green, the (n,2n) in red and the (n,3n) in blue. The radioactivity rays are presented in grey.

As for the ^{235}U isotope the spectra are presented up to a γ energy of around 400 keV, after which the HPGe detection efficiency is decreasing since the crystals are very small, making a proper cross section extraction at the desired accuracy impossible for the statistics acquired during the experimental run. The ^{232}Th spectrum is however much cleaner than the ^{235}U, making an identification of the energy rays easier. The rays pointed out in the spectra of figure B.4 are listed in table B.2.

The correction for dead time was realised using the 238.6 keV γ ray caused by the decay of ^{212}Bi.

5.4.3 ^{232}Th neutron inelastic scattering cross sections

Inelastic neutron scattering on ^{232}Th leads to the transfer of a certain amount of the neutron kinetic energy to the nucleus. To dispose of this energy, the residual nucleus emits γ rays until the ground state is reached. The emitted γ rays are characteristic for each nucleus and allow hence to identify a reaction. Figure 5.9(a) shows the lowest level energies

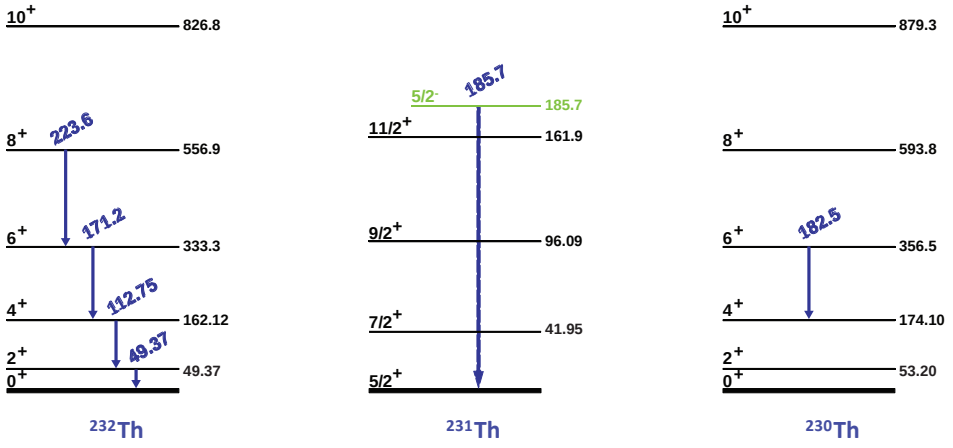

Figure 5.9: Partial level scheme of ^{232}Th showing the GS band in black (left), of ^{231}Th showing the GS band in black and an additional band in green (centre) and of ^{230}Th showing the lowest energy levels of the GS band in black (right). The studied transitions are shown in blue. All the energies are expressed in keV.

of ^{232}Th. In this section we have studied all the γ rays emitted between the state 8^+ and the 0^+ ground state with energies of 49.37, 112.75, 171.2 and 223.6 keV. For energies above these values the statistics were not sufficient to obtain any reliable results.

5.4.3.1 $4^+ \rightarrow 2^+$ transition in ^{232}Th

The transition between the states 4^+ of energy 162.12 keV and 2^+ of energy 49.37 keV in the ^{232}Th isotope gives birth to a $162.12 - 49.37 = 112.75$ keV γ ray of multipolarity E2. The neutron energy threshold for this transition corresponds to the energy needed to excite the 4^+ state and hence equals 162.12 keV. The internal conversion factor computed for this transition in thorium is $\alpha_{IC} = 6.68$.

The total number of effective counts that have been observed on the four detectors is 62180. In order to control the precision on the statistical error a neutron energy binning of 26 gates has been chosen for which the cross section was evaluated. The calculation has been realised according to the algorithms described earlier. The results of these calculations are shown in figure 5.10, the different yields for the four detectors are shown in figure C.5 and the values of the different data points are listed in table C.5.

Next to the threshold one can observe a very good agreement between the measured results and the TALYS code predictions. Although the experimental points underestimate the cross section in the 2 to 3 MeV neutron energy domain, the region between 3 and 6 MeV is in good conformity. For the descending part of the excitation curve we can nevertheless observe a systematic difference between the experimental and theoretical values. The differences seen here have already been observed in other experiments, such as ^{232}Th(n,5n)^{228}Th cross section measurements performed with a different experiment at

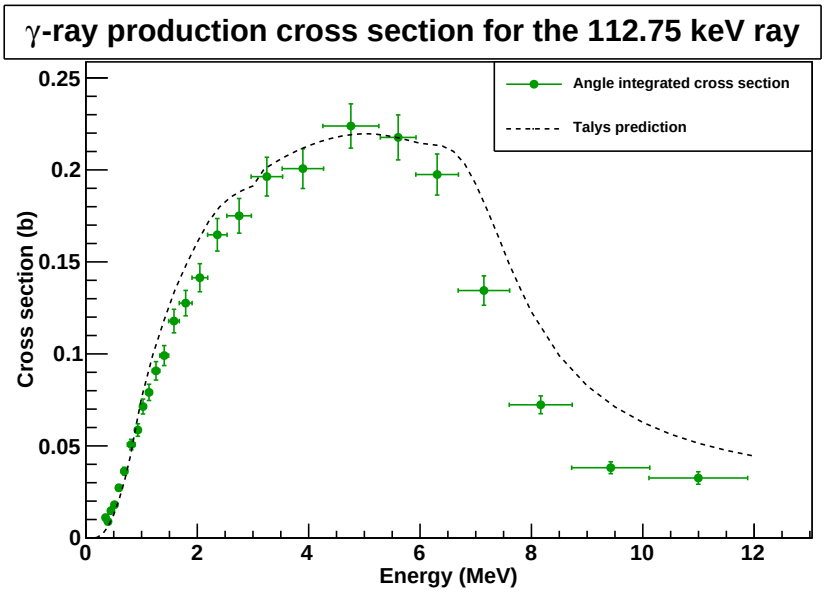

Figure 5.10: Total γ production cross section of the 112.75 keV transition from states $4^+ \rightarrow 2^+$ due to a ^{232}Th(n,n')^{232}Th reaction compared to TALYS predictions.

the CYCLONE facility in Louvain-la-Neuve [9]. This result is thus very important and of interest for the TALYS parameterisation optimisation.

The uncertainties on the cross section values range from around 8 to 12% in the high energy domain (above 9 MeV) and the low energy domain (below 500 keV), due to the weak values of the cross section which is reflected by very low counting and thus a rather large error on the statistics. The errors between these domains are in the order of 6% with a minimum of 5.3% which reflects the best result one can obtain considering the errors due to this experimental setup and the uncertainties on the efficiency values of the fission chamber as well as the germanium detectors.

5.4.3.2 $6^+ \rightarrow 4^+$ transition in ^{232}Th

This transition is characterised by the emission of a γ ray of 171.2 keV between the states 6^+ and 4^+ of the ground state band of energies 333.3 keV and 162.1 keV respectively and also corresponds to a multipolarity of order E2. The threshold for the ray is given by the 6^+ level energy and is thus equal to 333.3 keV. At this energy an E2 transition in ^{232}Th has an internal conversion coefficient of $\alpha_{IC} = 1.19$.

For this transition the experiment was able to produce 59201 effective counts summing the four detectors. The total time-of-flight spectrum has been binned into 24 different slices for the cross section calculation. The total cross section results are shown in figure 5.11, the angular dependent results are shown for each detector in figure C.6 and the values of the different data points are listed in table C.6.

For this transition we can make analogous observations as for the 112.75 keV transition.

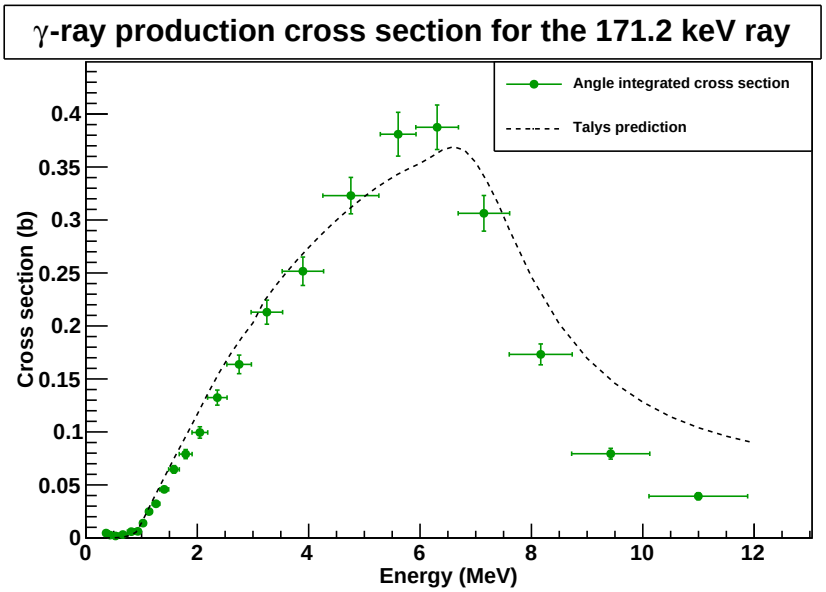

Figure 5.11: Total γ production cross section of the 171.2 keV transition from states $6^+ \rightarrow 4^+$ due to a ^{232}Th(n,n')^{232}Th reaction compared to TALYS predictions.

The agreement in the low energy domain between the theoretical TALYS predictions and the measured values is very satisfying, whereas the descending part suffers from the same difference as the previous γ ray.

Overall the uncertainties range also from 8 to 12.1% in the low and high energy domain where low statistics are occurring, while the main energy range between 1 and 9 MeV is affected by error in the order of 5 to 6.5%.

5.4.3.3 $8^+ \rightarrow 6^+$ transition in ^{232}Th

The γ decay between the two excitation states 8^+ and 6^+ of energies 556.9 and 333.3 keV is characterised by the emission of a 223.6 γ ray of type E2. The neutron energy threshold for this excitation function is 556.9 keV. For this transition the internal conversion coefficient is $\alpha_{IC} = 0.442$.

During the experimental run time 26104 counts were accumulated on the four detectors of the setup. This counting statistics allowed a binning of 19 gates, thus giving 19 data points for the cross section to be evaluated. The numerical values of the determined data points are given in table C.7, the points evaluated for each detector are shown in figure C.7 and the final cross section obtained is given in figure 5.12.

Similarly as for the previous transitions we can observe a rather good agreement between the experimental values and the TALYS code predictions, whereas the excitation function is descending faster for the measured points in the high energy domain.

As the counting number for this ray was a little lower than the previous ones the error rises to 18% in the low energy domain with the chosen binning. In the intermediate energy

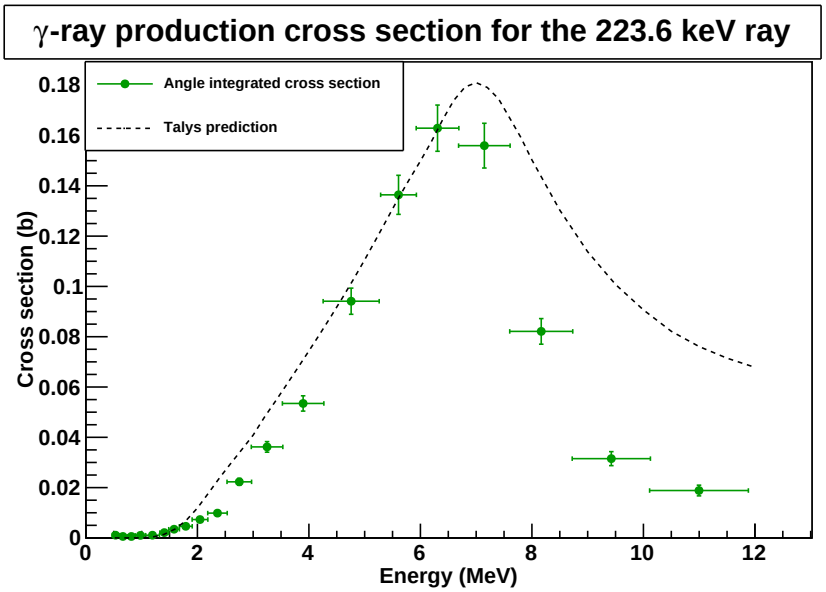

Figure 5.12: Total γ production cross section of the 223.6 keV transition from states $8^+ \rightarrow 6^+$ due to a ^{232}Th(n,n')^{232}Th reaction compared to TALYS predictions.

range however we reach errors as low as 5.5% alike the 112.75 and 171.2 keV transitions.

5.4.3.4 $2^+ \rightarrow 0^+$(GS) transition in ^{232}Th

The transition of the 2^+ level of energy 49.37 keV to ground state is made through the emission of a 49.37 keV γ ray, whose energy corresponds to the threshold of the reaction. As the other previous transitions it is also of order E2. For this very weak energy however, the internal conversion coefficient is very strong: $\alpha_{IC} = 327$.

The measurements yield a total number of counts in this energy ray of 772 counts for which we chose 10 gates to evaluate the cross section. The graphical representation of the total yield is shown in figure 5.13, the different detector output in figure C.8 and the data point values are listed in table C.8.

Although this is the last transition in the chain of the decay, fed by the other levels analysed above, the measured counts are very low as its internal conversion coefficient is very high and thus only one of 327 decays is actually realised through the emission of a γ ray. For this reason the error on the statistical counting values is rather high. Furthermore the energy of this ray is very low, and the detector efficiencies in this domain are affected by a high uncertainty. These two reasons lead to a high error on the total cross section yields, ranging from 20 to 27%.

Due to these large uncertainties, it is difficult to comment the comparison between experimental and theoretical points one by one. It is noteworthy to mention that in general a rather fair agreement can be observed, as most of the points error bars overlap with the TALYS predictions.

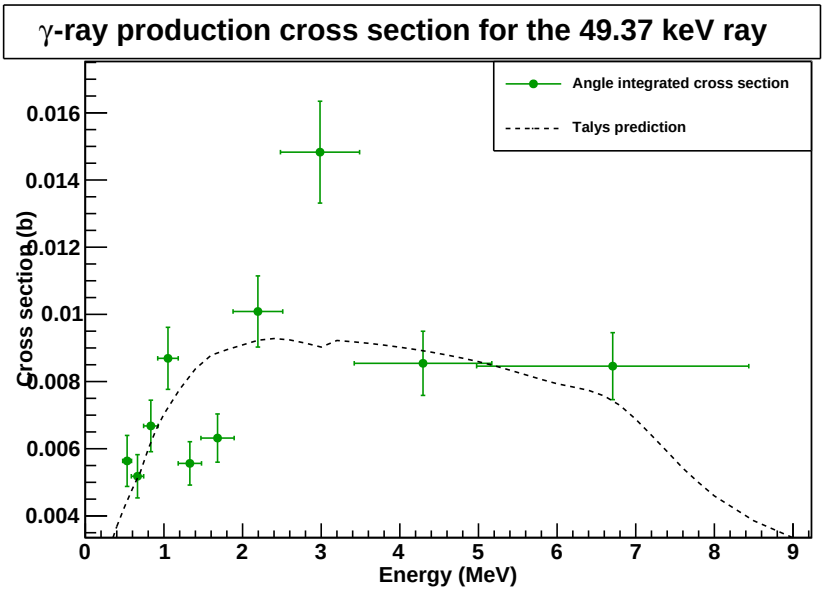

Figure 5.13: Total γ production cross section of the 49.37 keV transition from states $2^+ \rightarrow 0^+$ due to a ^{232}Th(n,n')^{232}Th reaction compared to TALYS predictions.

5.4.4 ^{232}Th(n,2n) reaction cross sections

A (n,2n) reaction on the ^{232}Th isotope leads to the creation of a ^{231}Th nucleus after the ejection of one neutron. The latter produced isotope may be left in an excited state. The disposal of the energy surplus will take effect through the emission of one or more γ rays. Figure 5.9(b) shows the lower energy levels of the ^{231}Th GS band as well as the next lowest energy of a rotational band. In this section we will present the analysis of the 185.7 keV decay transition.

5.4.4.1 $\frac{5}{2}^- \rightarrow \frac{5}{2}^+$ (GS) transition in ^{231}Th

The decay studied here is realised between the $\frac{5}{2}^-$ state at energy 185.7 keV of one of the ^{231}Th rotational bands to the $\frac{5}{2}^+$ GS. The emitted γ ray has thus an energy of 185.7 keV and has the multipolarity E1. The threshold of this reaction is 6.65 MeV. The internal conversion coefficient of this γ decay which corresponds to an electric dipole transition is $\alpha_{IC} = 0.112$.

On the four detectors of our experimental setup, we were able to notice 13908 counts. This counting rate was sufficiently high to compute the γ production cross section at 12 neutron energies. The final cross section that was determined is shown in figure 5.14, the values are given in table C.9 and the separate detector yields are represented in figure C.9.

Figure 5.14 shows also the theoretical calculations obtained with TALYS for this γ production cross section. In this case we observe that the measured points are 2.58 times higher than predicted. Similarly as for the other transitions the total counting lead to a

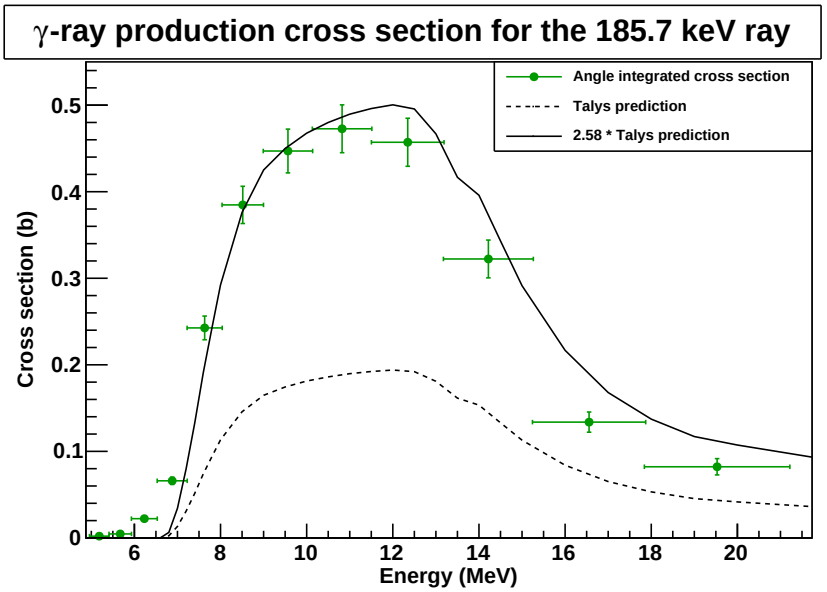

Figure 5.14: Total γ production cross section of the 185.7 keV transition from states $\frac{5}{2}^- \rightarrow \frac{5}{2}^+$ due to a ^{232}Th(n,2n)^{231}Th reaction.

precision in the order of 5-6% in the mid energy range.

5.4.5 ^{232}Th(n,3n) reaction cross sections

After a (n,3n) reaction on ^{232}Th, a ^{230}Th isotope is born. If the energy of the incident neutron is higher than the threshold energy needed to extract 2 neutrons from the initial nucleus, the formed ^{230}Th is created in an excited state. Decay will occur by γ emission, specific to the studied nucleus. For ^{230}Th the low level energies are given in figure 5.9(c). The only one that could be extracted to obtain information on ^{232}Th(n,3n) reactions is the 182.5 keV γ ray studied below.

5.4.5.1 $6^+ \rightarrow 4^+$ transition in ^{230}Th

The transition between the 6^+ and 4^+ states of the ^{230}Th GS band of energies 356.5 and 174.10 keV is realised by the emission of a γ ray of energy 182.5 keV. The incident neutron energy required for such a reaction to be possible is 11.97 MeV. This transition has multipolarity E2 and the internal conversion coefficient is given by $\alpha_{IC} = 0.927$.

Summing the set of four detectors 5861 counts were available to evaluate the total γ production cross section, shown in figure 5.15, the individual detector analysis, yielding angle dependant cross sections are shown in figure C.10 and the obtained data values as given in table C.10.

For this transition the obtained values are roughly 0.72 times lower than those predicted by TALYS. This deviance must however be considered with care, as the statistics in this energy region are very low, and the experiment has not been designed for such high

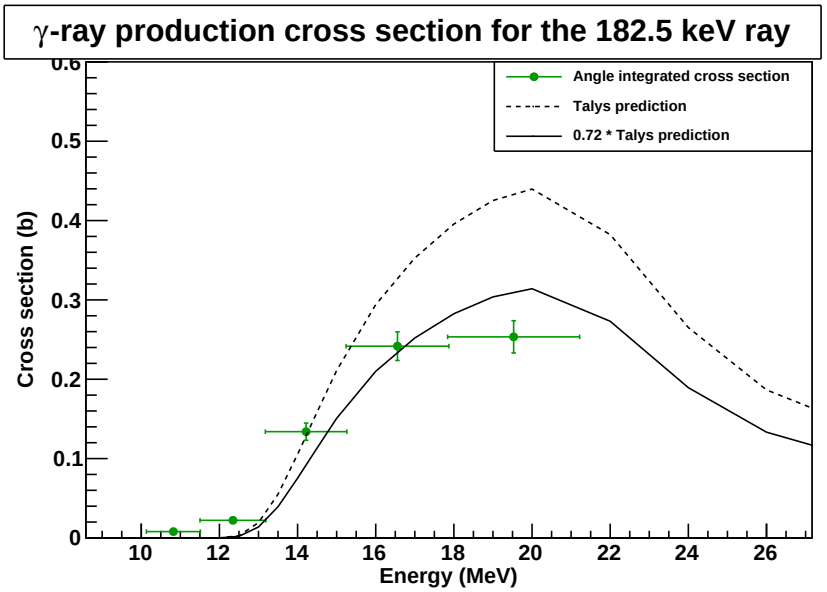

Figure 5.15: Total γ production cross section of the 182.5 keV transition from states $6^+ \rightarrow 4^+$ due to a ^{232}Th(n,3n)^{230}Th reaction.

neutron energies. It is to observe that the incident neutron flux is not sufficiently high at the GELINA facility for such high energies, where (n,3n) reactions start. Therefore we could only evaluate 5 points in the first part of the excitation curve. For these reasons the uncertainties are also higher than for the other transitions, not undercutting 7%.

5.5 Discussions

After the extraction of the cross sections of both, the ^{235}U and the ^{232}Th, isotopes we can conclude that differences can be observed between the measured values and the theoretical predictions computed by TALYS. In general we can see a rather good agreement for the inelastic reaction cross sections up to 8 MeV, whereas the results differ from the model calculations above 8 MeV and thus for the (n,2n) and (n,3n) cross sections.

This can be due to several reasons, where the most important cause can be explained by the fact that the low energy reactions (below 8 MeV) are dominated by the well-modelled compound nucleus reaction mechanism, whereas the region above this energy is strongly affected by the pre-equilibrium mechanism. Indeed, the model calculations performed by TALYS for the latter mechanism use the semi-classical *Exciton model*, for which no spin distributions are considered on the microscopic scale [10], which can cause such discrepancies for different γ production cross sections.

Other reasons explaining the differences of the measured cross sections compared to the theoretical ones are that for the studied isotopes, the (n,f) reaction channel is in competition with the (n,xn) channel, and therefore needs to be fitted properly. If this is not guaranteed, errors will be introduced into the (n,xn) reaction type prediction. This

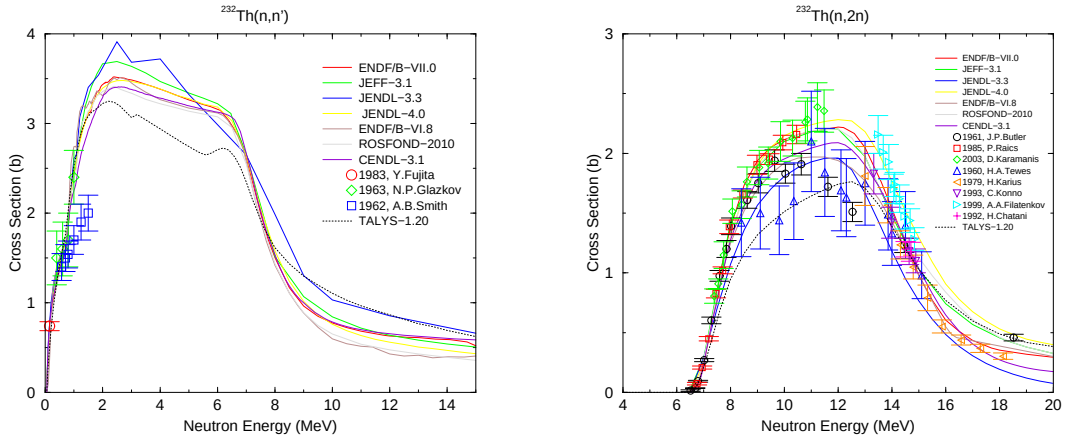

(a) (b)

Figure 5.16: Total ^{232}Th(n,n') cross section (a) and total ^{232}Th(n,2n) cross section (b) computed by TALYS and compared to evaluated database values.

effect can explain the differences observed for the 129.30 keV γ ray of the ^{235}U isotope following from inelastic scattering.

It is also noteworthy to observe that branching ratios of the different excitation levels are of very high importance for the amplitudes of the measured γ production cross sections, and level density parameters can lead to variations in the descending parts of the excitation curves. All these parameters are connected and are thus crucial to obtain correct results.

While an accurate knowledge of the latter parameters is mandatory to properly fit the total (n,xn) reactions, the fact of neglecting spin distributions at a microscopic scale rather plays on the different γ production cross sections only. Figure 5.16 shows the total (n,n') and (n,2n) reaction cross sections on ^{232}Th predicted by TALYS. Here one can already observe a systematic difference between TALYS and measured values, resulting in a deviance of the cross sections obtained in this work. It is however not high enough to explain a factor of 2.58 observed for the ^{232}Th(n,2n) reaction, for which the spin distributions have to be taken into account.

This work has shown the need for further investigations on the parametrisation of TALYS, and the results obtained can be used to obtain better values for its databases.

Bibliography

[1] F.S. Crawford, *Method of effective counts for combining experimental results*, Nuclear Instruments and Methods **33** (1965), 332-334.

[2] G. Zech, *Comparing statistical data to Monte Carlo simulation - Parameter fitting and unfolding*, DESY-Report 95-113 (1995).

[3] N. Fotiades, G.D. Johns, R.O. Nelson, M.B. Chadwick, M. Devlin, M.S. Wilburn, P.G. Young, J.A. Becker, D.E. Archer, L.A. Bernstein et al., *Measurements and calculations of $^{238}U(n,xn\gamma)$ partial γ ray cross sections*, Physical Review **C69** 024601 (2004).

[4] A. Hutcheson, C. Angell, J.A. Becker, A.S. Crowell, D. Dashdorj, B. Fallin, N. Fotiades, C.R. Howell, H.J. Karwowski, T. Kawano, J.H. Kelley, E. Kwan, R.A. Macri, R.O. Nelson, R.S. Pedroni, A.P. Tonchev, W. Tornow, *Cross sections for $^{238}U(n,n'\gamma)$ and $^{238}U(n,2n\gamma)$ reactions at incident neutron energies between 5 and 14 MeV*, Physical Review **C80** 014603 (2009).

[5] A. Hutcheson, *Neutron-Induced Partial Gamma-Ray Cross-Section Measurements on Uranium*, Ph.D. thesis, Department of Physics in the Graduate School of Duke University, 2008.

[6] D.P. Mcnabb et al., *Neutron-induced partial gamma-ray cross-section measurements with GEANIE at LANSCE/WNR*, Conference: Symp. on Capt. Gamma Ray Spectroscopy, Santa Fe, NM, (1999) p.384.

[7] P. Romain, private communication.

[8] H.C. Karam, *Mise au point de la mesure de sections efficaces de réations (n,xn) par spectroscopie γ prompte sur des cibles très radioactives*, Ph.D. thesis, Université de Strasbourg, 2009.

[9] M. Kerveno et al., *Measurement of $^{232}Th(n,5n\gamma)$ cross sections from 29 to 42 MeV*, Proceedings of the International Conference on Nuclear Data for Science and Technology, April 22-27, 2007, Nice, France, EDP Sciences, 2008, p. 1019-1022.

[10] A.J. Koning, private communication.

Chapter 6

Prospects: Development of a segmented detector

As we can conclude from the analysis of the data acquired with the existing setup, a good counting rate is mandatory for a precise extraction of reaction cross sections from the experimental data. For highly radioactive samples, these problems grow even more important as a very large dead time is creating a loss of counting statistics.

To reduce the acquisition dead time for strongly radioactive materials, the conception of a multi-HPGe detector composed of several segments to be used with the experimental setup described in chapter 3 was studied. This chapter presents the development studies performed on the design of this new type of detector and discusses the different aspects affecting the detectors geometry.

6.1 Motivation

The presence of radioactive samples can drastically increase the background on the HPGe detectors. As the size of the germanium crystal increases, the background becomes more and more important. When working with very highly radioactive samples, this background is not negligible and has a severe impact on the detection dead time.

Reducing the size of the radioactive sample or increasing the distance between the sample and the detector would cut back on the counting rate but would, at the same time, lead to a loss in efficiency for the detections of interest. The only acceptable solution to avoid dead time due to a high counting rate is the use of several smaller detectors instead of a single large crystal. Due to the structural dimensions of the detectors this is not so straightforward as they have to be placed at well defined positions.

An ideal solution to this problem can be obtained by using a large germanium crystal which is divided into several pixels, each being able to be used independently. As a physical division of the crystal would induce more difficulties on dead layers, the segmentation is best obtained by simply pixelizing one of the detector electrodes. Each of its segments will then detect interactions in a given array of the detector.

The previous measurement campaigns have shown a counting rate of up to 2 kHz, obtained for highly radioactive samples such as ^{235}U. This rate can be dealt with without

any difficulty, whereas the counting rate on an identically sized ^{233}U sample exceeds 40 kHz, and strongly affects the data acquisition dead time. To be able to treat such samples, a pixelisation of at least 16 segments should be considered.

6.2 Detector Physics and signal shape simulations

In HPGe detectors, incident γ rays interact with the semiconducting germanium and create electron/hole pairs in a proportional number to the energy of the interacting γ ray. By applying a sufficiently high voltage between the detector electrodes, these pairs can be collected, and thus create a signal on the detector electrodes which is proportional to the deposited energy [1].

The movement of the electron/hole pairs however, creates an induced charge which is detectable in the entire crystal. For segmented detectors, this means that deposition of energy in one cell segment creates a so-called *mirror charge* sensible on the neighbouring cells [2]. These signals are purely due to an induction effect and only occur during charge collection, i.e. during the rise time of the original signal.

Even though these mirror charges are in general much smaller than the amplitude of the signal itself, they can affect a possible interaction taking place at the same time in the neighbouring cell. Considering a simultaneous detection of a 40 keV in one cell and 400 keV in the next cell, a mirror signal of an amplitude 10 times weaker than the signal generated from the latter one will have the same amplitude as the 40 keV signal detected in the neighbour cell. Such interferences lead to resolution degradation and are subject to false detection triggering.

For these reasons, the segmentation of the detector must be optimised in a way to minimise the effect of mirror charges as much as possible, in order to maintain a proper detection resolution.

The determination of the best configuration of the segmented detector requires the possible segmentation options to be studied precisely. For this purpose the MGS (Multi Geometry Simulation) code [3], developed at IPHC, was used to compute the different signal shapes during collection time in all the detector cells for interactions taking place at different spots in the crystal.

The MGS code models the crystal using a fixed grid geometry. It computes the electric field inside the germanium and determines the track of the electrons and holes created by the energy deposition of an incident γ ray using the *Shockley-Ramo* theorem. As the signal amplitude varies proportionally to the amount of energy deposited, a unitary charge deposition is considered. In the original MGS code the maximum signal amplitude is normalised to $54.13 \cdot 10^{-3}$ (A.U.).

In the performed simulations a crystal of 40 mm height and width and a depth of 20 mm was chosen. The applied electric potential difference between the anode and the cathode was set to 3500 V, which is sufficient to obtain a complete depletion. The minimum computation grid size with cubes of 0.5 mm was used. The segmentation effect on one of the electrodes was studied using different configurations: 4x4 pixels, 5x5 pixels and 6x6 pixels, with touching and spaced electrode options.

Figure 6.1 shows the signal amplitudes (in arbitrary units) of a 6x6 touching pixel

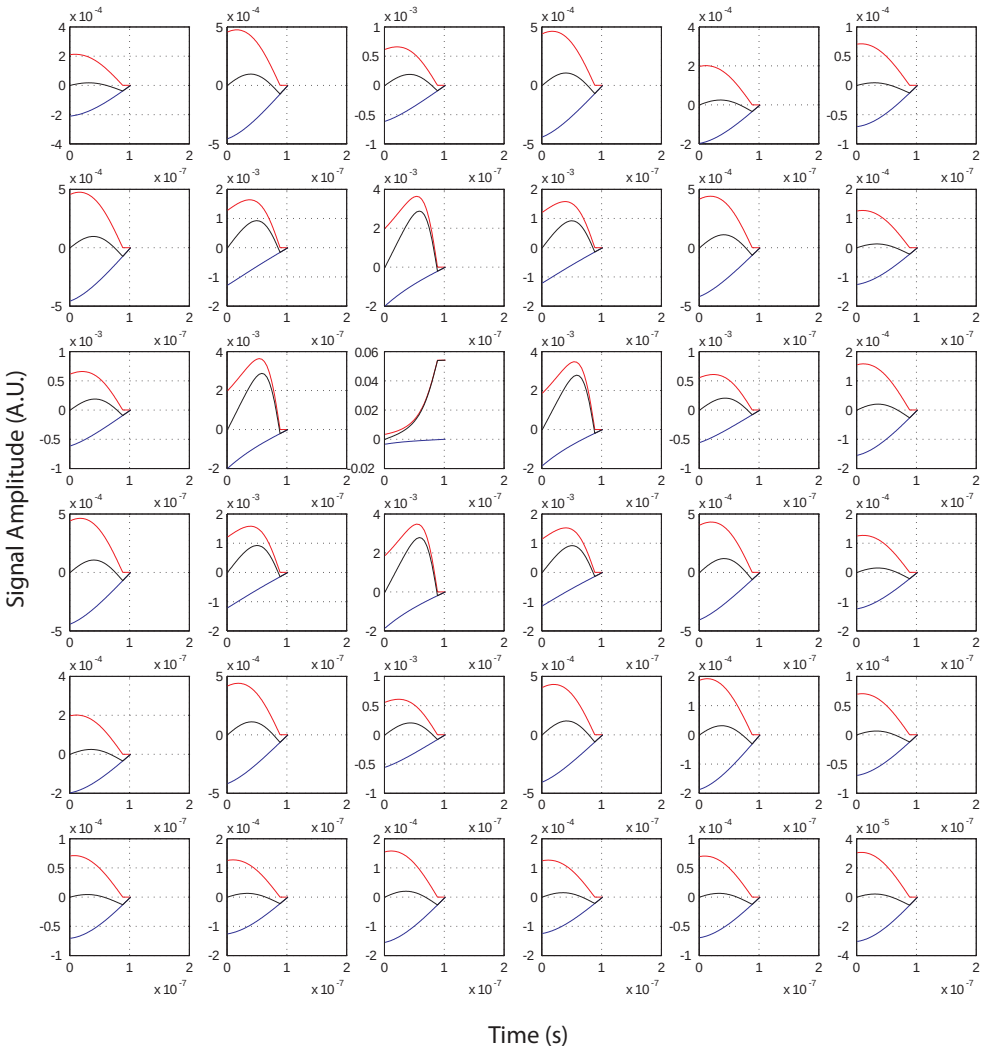

Figure 6.1: Pulses observed for each segment in a 6x6 touching pixel detector configuration with a centred energy deposition in front of pixel 15. The red lines represent the contribution of the electrons, the blue ones that of the holes and the total pulse shape, corresponding to the sum of both contributions, is in black.

configuration as a function of time (in s). The red lines represent the contribution of the electrons, the blue ones that of the holes and the total pulse shape, corresponding to the sum of both contributions, is in black. In this scenario, the interaction took place in front of the 15^{th} pixel[1]. After the collection of the electrons and holes, the maximum signal amplitude is reached, which corresponds to the charge left on the preamplifier. In the surrounding cells one can clearly observe the presence of temporary signals during the rise time of the original pulse, in agreement with the discussions in section 6.2.

6.3 Study of the different segmentation options

This section treats different pixelisation aspects and their effect on the amplitude of the mirror charges.

6.3.1 Pixelisation

For this work we have studied all possible square segmentation scenarios. As mentioned in section 6.1, the rasterisation should not be smaller than 4x4 to take into account the dead time loss, whereas physical limits on the size of pixels maximise the segmentation to 6x6 pixels. In this section the different pixels are touching and the interaction of the γ ray takes always place in the middle of the crystal, i.e. at an equidistant point between the cathode and the anode.

Figure 6.2 shows the pulses computed for *centred* energy depositions i.e. a deposition facing the centre of the nearest electrode segment. The mirror charges observed for first neighbouring cells (i.e. the left, right, up and down cells) range from $1.914 \cdot 10^{-3}$ for a 4x4 pixel detector over $2.557 \cdot 10^{-3}$ for a 5x5 pixel one to $2.874 \cdot 10^{-3}$ for the 6x6 pixel configuration.

In this example, one can observe that the mirror charges grow larger when the number of pixels is increased and their size thus decreased. As the mirror charges are however a capacitive effect, the segments getting smaller and smaller from one configuration to the other, one could have expected the opposite behaviour. In fact this is not the case, because centred energy depositions were studied. For a larger pixel, its centre is farther away from the neighbour pixel, and the observed mirror charge is diminished.

In reality however the energy deposition is not taking place at privileged places of the crystal, as the interactions are completely random. When simulating an energy deposition at a fixed distance to the neighbour pixel, one can observe a better mirror charge to signal ratio for smaller pixels, as the mirror charge amplitude depends on the size of the pixel. These arguments speak in favour of a higher pixelisation.

6.3.2 Segment spacing

To minimise the effects of mirror charges, we examined the possibility of separating the different segments from each other. This scenario is illustrated in figure 6.3 for the 4x4 pixel configuration, for which a spacing of 0.5 mm was chosen.

[1] Pixels are numbered from left to right, line by line, starting at the upper left pixel

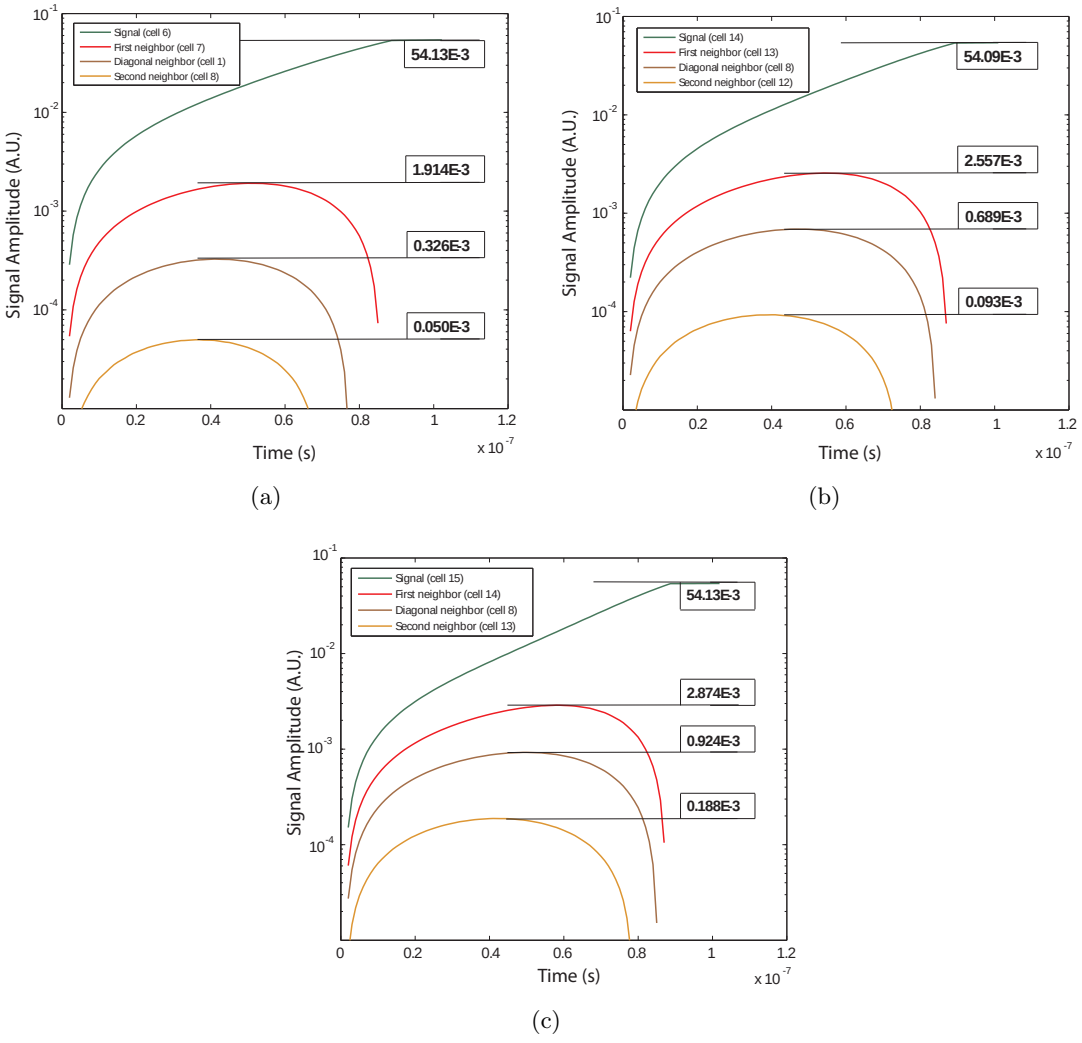

Figure 6.2: Pulses computed for the signal (green) and the mirror charges of the next neighbours (left, right, up and down) (red), the second nearest neighbours (diagonal) (brown) and the third next neighbours (second to the left, right, up and down) (orange) for a 4x4 (a), 5x5 (b) and 6x6 (c) pixel configuration.

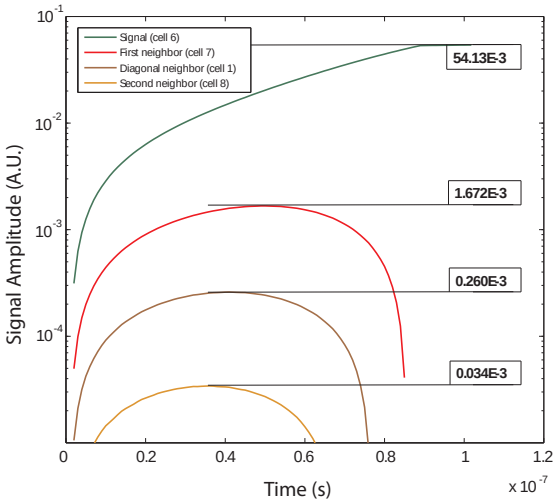

Figure 6.3: Pulses computed for the signal (green) and the mirror charges of the next neighbours (left, right, up and down) (red), the second nearest neighbours (diagonal) (brown) and the third next neighbours (second to the left, right, up and down) (orange) for 4x4 pixels, spaced by 0.5 mm.

This configuration gives rise to first neighbour mirror charges of $1.672 \cdot 10^{-3}$ versus the comparable non separated pixel case $1.914 \cdot 10^{-3}$ (figure 6.2(a)). So, indeed the mirror charges are dropped by 12.64%, as the different segments are smaller here.

6.3.3 Border interactions

Up to now, all the interactions were considered as *centred* energy depositions i.e. a deposition facing the centre of the nearest electrode segment. When computing the γ ray interaction facing the junction of 4 touching segments, the risk of charge splitting can be observed, as shown in figure 6.4.

In this case the charge is split almost evenly onto 4 different segments. The signal pulse height varies between $12.78 \cdot 10^{-3}$ and $14.30 \cdot 10^{-3}$. This effect will make it very difficult to distinguish between single events which were split, simultaneous detections in neighboured cells and mirror charges. In fact, observing the pulse heights in figure 6.4, one can not affirm being victim of charge splitting, it would as likely be possible to see these pulses when 4 simultaneous interactions occurred. It will be impossible to develop reliable *add-back* algorithms.

For spaced segments however this effect did not occur. When simulating border interactions for slightly spaced pixels, the charge was always attracted by one single electrode contact. Although in this case we could observe higher mirror charges for the direct neighbours of the touched pixel, which is natural as the distance to those pixels is much smaller, the effect of charge splitting could not be observed. In fact, the non-polarised region between two segments deviates the electrons or holes towards the electrode, avoiding the charge to be collected on several pixels at the same time.

The effect of spacing the segments too much will however lead to dead regions at the

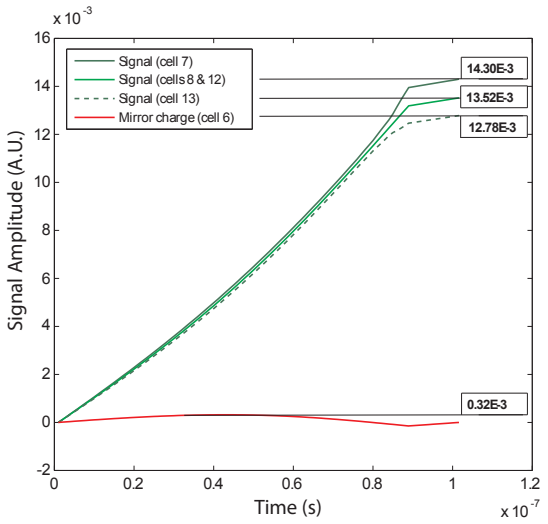

Figure 6.4: Pulses computed in a 5x5 touching pixel detector configuration for the signal parts (variations of green) and a neighbour (red).

back of the crystal. An optimum spacing was found for 0.5 mm.

6.3.4 Interaction depth

The γ ray energies which shall be observed with this detector include energies in the order of 100 keV. Considering photon attenuation, one can compute the attenuation length λ of an incident γ ray inside the germanium crystal, corresponding to the inverse of the mass attenuation coefficient μ:

$$\lambda = \frac{1}{\mu} \tag{6.1}$$

for a γ ray of energy 100 keV in germanium, $\mu = 2.93\ \mathrm{cm}^{-1}$, and $\lambda = 0.34$ cm. This means that most of the interactions in this energy domain take place in the first millimetres of the crystal. Therefore it is important to study the effect of energy depositions next to the crystal borders to determine which front of the crystal shall be polarised and segmented.

Depending on the depth of the interaction in the crystal, either the contribution of the electrons or the one of the holes dominates the final shape of the signal. This effect is shown in figure 6.5. When simulating an interaction closer to the anode (figure 6.5(b)), the total signal depends stronger on the electron movement and approaches the red curve, whereas interactions closer to the cathode (figure 6.5(c)) follow the blue curves as their signal is overruled by the hole movements.

One can observe that the absolute values of the amplitude of the mirror charges is

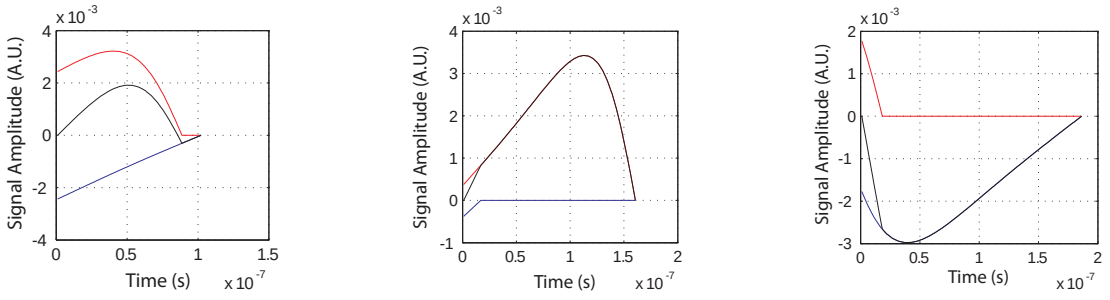

Figure 6.5: Mirror charges for an energy deposition equidistant to the anode and cathode (a), next to the anode (b), next to the cathode (c).

larger when the interaction takes place close to the borders of the crystal rather than in its centre. The difference between the absolute values of the pulses of an interaction next to the cathode or anode is however below 10 %. This is not significantly high enough to privilege one of the scenarios.

6.3.5 Conclusions

The performed simulations lead to the conclusion that the mirror charges are always present, although their magnitude strongly depends on the chosen geometry. In fact, the mirror charge amplitudes depend mainly on the chosen size of the pixels. The larger they are, the more they suffer from this capacitive effect of induced charges. This speaks in favour of choosing the highest pixelisation possible, namely 6x6 segments.

Spacing the segments leads to a further reduction of their surface size without introducing additional dead zones. Actually, the opposite is true. Introducing a gap between the segments prevents from charge splitting, which is much desirable. These two arguments clearly privilege the spaced segment option.

As the behaviour of the mirror charges is not significantly affected whether the interaction takes place near the anode or cathode, it is not important which front of the detector should be polarised or segmented.

The above considerations lead us to the conclusion that the best segmentation option is a pixelisation of 6x6 with slightly spaced pixels. For this configuration, one should not expect mirror charge magnitudes above 10 % of the original pulse height in the case of centred energy depositions. This should not induce any difficulties in the signal treatment.

Practically, figure 6.6 shows a superposition scenario of a signal of amplitude A and a mirror charge created in the neighbour cell by an incident γ ray of amplitude $10 \cdot A$ (figure 6.6(a)) and $20 \cdot A$ (figure 6.6(b)) respectively. The green curves represent the real signal detection, the red ones the mirror charge created by an interaction in a surrounding cell and the black one the sum of both pulses.

In this particular scenario, the superposition of signals and mirror charges ranging over one order of magnitude should not be a problem, as the rise time pulse is always

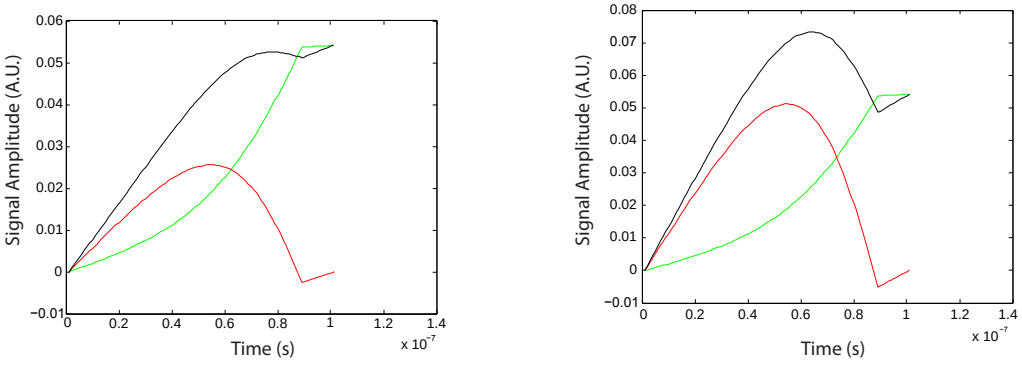

(a) (b)

Figure 6.6: Superposition scenario for a signal with mirror charge of a signal 10 times higher (left) and 20 times higher (right) than the original signal in the case of a 6x6 pixel detector. The signal is shown in green, the mirror charge in red and the superposition of both in black.

smaller than the final charge. A factor 20 between both yet results in a rising part of the pulse higher than the final charge. Our choice of the geometry should restrict these superposition cases.

6.4 Geometrical constraints

Another issue of such a large detector is caused by the structural dimensions. Indeed, 36 independent pixels need 36 preamplifiers. As the detector has to be able to occupy a position at a grazing angle to the beam direction and at the same time approach the target the most closely possible, special care has to be taken on the external design of the counter. For this reason a unique conception was made, installing the preamplifiers at a certain distance from the crystal enabling the latter one to approach the sample to a maximum.

A schematical drawing of the detector cap, provided by the constructor Canberra, is shown in figure 6.7. This design corresponds to the best compromise between crystal to sample distance and crystal to preamplifier distance. It was conceived for an angle of 150° in the experimental setup and is able to approach the target to 12.5 cm.

6.5 Conclusions

This conception study lead to the purchase of a 36 pixel HPGe detector with the detector constructor Canberra. The crystal size is fixed to 40 mm length and height with a depth of 20 mm. This project was realised in the context of the Agence Nationale pour la Recherche (ANR) funding project DISPALEND.

The new detector will be delivered by the end of summer 2010. After experimental tests it will be ready for use at the experimental setup at GELINA.

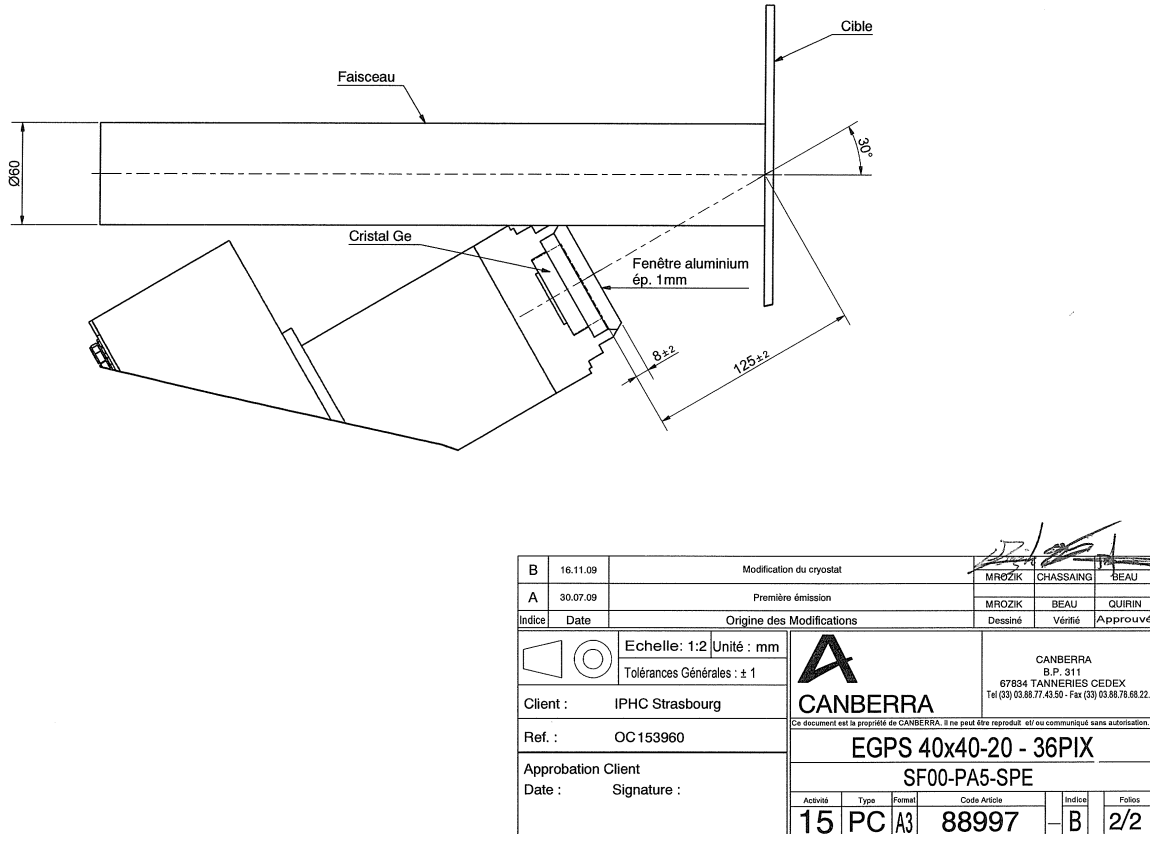

Figure 6.7: Drawing of the detector cap for the new segmented HPGe detector.

Bibliography

[1] G.F. Knoll, *Radiation detection and measurement*, 3^{rd} edition, John Wiley & Sons, New York, 2000

[2] Z. He, *Review of the Shockley-Ramo theorem and its applications in semiconductor gamma-ray detectors*, Nuclear Instruments and Methods in Physics Research **A463** (2001), 250-267.

[3] P. Medina, C. Santos, D. Villaumé, *A simple method for the characterization of HPGe detectors*, Instrumentation and Measurement Technology conference, May 2004.

Chapter 7

Conclusions

In previous works of the collaboration the method of measuring (n,xnγ) reactions at the GELINA facility at IRMM, Belgium has already been tested. A first measurement campaign took place at a flight distance of 200 m, where cross sections on ^{206,207,208}Pb were probed and a second one at a flight distance of 30 m with measurements of inelastic scattering and (n,2n) reactions on ^{nat}Pb, ^{nat}W and ^{235}U. The results of these measurement series were very promising, although an important difference was found on the ^{235}U(n,2n) reaction cross sections with respect to theoretical predictions and other works.

Another issue of these previous experiments was the precision of the evaluated reaction cross sections. Indeed it was not possible to yield uncertainties lower than 10% on the acquired data, which was not satisfactory. As already mentioned in the first chapter of this work, uncertainties on the measured cross sections of the order of 5% or less are required on several isotopes of interest for the development of new nuclear reactors.

The aim of this work was thus to analyse all the different components used in the experimental setup to reduce the error to a minimum and to verify the previous data on ^{235}U with a new sample. This was achieved through an extensive analysis of the detection efficiencies of the used counters and the construction of a new experimental setup, with a better shielding for background and detection noises. With this newly designed setup, we were able to accomplish the desired accuracy goal and to measure (n,xnγ) reaction cross sections on ^{232}Th and to remeasure the ^{235}U reaction cross sections.

With these efforts, better results on the ^{235}U isotope have been obtained. Some systematic errors introduced in the foregoing campaign could be eliminated and a precision of 5% on the main energy rays was achieved. Despite these corrections of the previous data, the new results lead to the same conclusion considering a deviation to other works and theoretical predictions. For the inelastic scattering reaction and a subsequent emission of a 129.30 keV γ ray, differences in the order of 25% were found and for the (n,2n) reactions an almost continuous factor of 0.45 could be observed for the three decay energies (152.72, 200.97 and 244.2 keV) analysed with respect to predictions of the TALYS code. Differences between our measurements and the ones of A. Hutcheson et al. and D.P. McNabb et al. were also found, but the information on the details of their analysis were not sufficient to be investigated further.

Besides the ^{235}U isotope, a second measurement campaign was realised on the ^{232}Th

isotope, for which (n,n'γ), (n,2nγ) and (n,3nγ) cross sections could be measured. For the inelastic scattering, our results agree very well with the TALYS predictions, although the code's computed cross sections descend slower than the measured ones. Similarly as for the ^{235}U isotope, the (n,n'γ) reaction cross sections could be determined at a precision of 5%. For the (n,2nγ) and (n,3nγ) cross sections the uncertainty was a little larger, as the incident neutron flux was lower in this energy domain, leading to a higher error on counting statistics. The (n,2nγ) reaction cross sections measured are 2.6 times higher and for the (n,3nγ) reactions a factor 0.72 could be observed between our experiments and the TALYS predictions.

The results of these both measurement series can be used to work out a better parameterisation of the TALYS code. The amplitude difference on the ^{235}U(n,2n), ^{232}Th(n,2n) and ^{232}Th(n,3n) cross sections could be caused by the fact of neglecting the spin distributions in the pre-equilibrium model calculation of TALYS. False branching ratios of the different decay channels in the ^{235}U, missing precision on the nuclear level densities as well as a bad parameterisation of the neutron induced fission cross section can lead to further differences. With our measurements these parameters can be optimised and improve the reliability of the code.

The work on the improvement of the precision permits the experimental setup to probe (n,xnγ) reactions at accuracies of 5% presuming long enough experimental runs, reducing the counting uncertainties to below 1%. This setup can now be used to measure reactions as the inelastic scattering on ^{238}U for which a high priority is requested.

A next step in the measurement are (n,xnγ) reaction cross sections on enriched isotopes of tungsten (^{182}W, ^{183}W, ^{184}W and ^{186}W), for which the comparison to theoretical codes is easier as they are not fissionable and hence do not need the fission decay channel to be taken into account.

Another goal is the determination of (n,xnγ) reaction cross sections of very highly radioactive isotopes, such as ^{233}U. In order to prepare these measurements, a new segmented detector was conceived in this work, to reduce dead time caused by the strong radioactivity of these isotopes. This detector will complete the current experimental setup and allow the measurement of new reaction cross sections unknown at this stage.

Appendix A

Values used to compute the cross sections

A.1 HPGe detector efficiencies

Below are represented the tables with the efficiency values used for the four different HPGe detectors of the experimental setup to evaluate the reaction cross sections. These values include the detection probability for each semiconductor as well as the auto-absorption coefficient inside the used sample.

The uncertainty for the energies below 100 keV used was 6%, for energies above it was 3% as discussed in section 4.2.5.

A.1.1 Efficiency values for the ^{235}U isotope

γ energy (keV)	Grey detector	Green detector	Red detector	Blue detector
129.30	$1.444 \cdot 10^{-3}$	$1.425 \cdot 10^{-3}$	$1.808 \cdot 10^{-3}$	$8.248 \cdot 10^{-4}$
152.72	$1.836 \cdot 10^{-3}$	$1.479 \cdot 10^{-3}$	$1.974 \cdot 10^{-3}$	$9.855 \cdot 10^{-4}$
200.97	$2.179 \cdot 10^{-3}$	$1.267 \cdot 10^{-3}$	$1.855 \cdot 10^{-3}$	$1.038 \cdot 10^{-3}$
244.2	$2.086 \cdot 10^{-3}$	$1.026 \cdot 10^{-3}$	$1.491 \cdot 10^{-3}$	$9.297 \cdot 10^{-4}$

Table A.1: HPGe detector efficiency values for the ^{235}U isotope.

A.1.2 Efficiency values for the ^{232}Th isotope

γ energy (keV)	Grey detector	Green detector	Red detector	Blue detector
49.37	$5.750 \cdot 10^{-4}$	$7.600 \cdot 10^{-4}$	$8.400 \cdot 10^{-4}$	$3.800 \cdot 10^{-4}$
112.75	$1.166 \cdot 10^{-3}$	$1.302 \cdot 10^{-3}$	$1.603 \cdot 10^{-3}$	$6.845 \cdot 10^{-4}$
171.2	$2.123 \cdot 10^{-3}$	$1.447 \cdot 10^{-3}$	$2.025 \cdot 10^{-3}$	$1.074 \cdot 10^{-3}$
182.5	$2.219 \cdot 10^{-3}$	$1.389 \cdot 10^{-3}$	$1.987 \cdot 10^{-3}$	$1.081 \cdot 10^{-3}$
185.7	$2.234 \cdot 10^{-3}$	$1.371 \cdot 10^{-3}$	$1.973 \cdot 10^{-3}$	$1.080 \cdot 10^{-3}$
223.6	$2.237 \cdot 10^{-3}$	$1.145 \cdot 10^{-3}$	$1.758 \cdot 10^{-3}$	$1.007 \cdot 10^{-3}$

Table A.2: HPGe detector efficiency values for the ^{232}Th isotope.

Appendix B

Integral energy spectra

B.1 Raw spectra acquired with the ^{235}U sample

B.2 Raw spectra acquired with the ^{232}Th sample

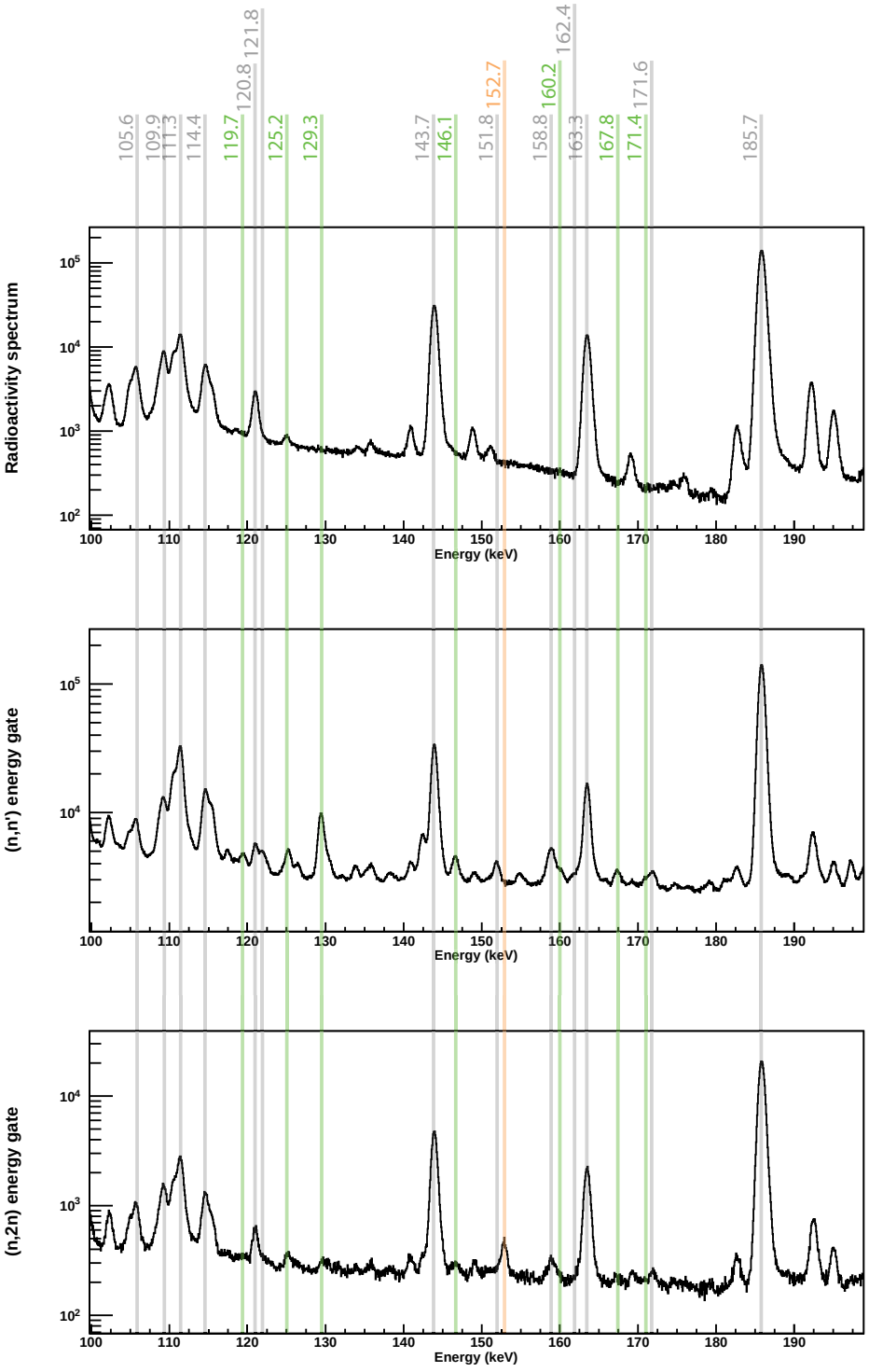

Figure B.1: Raw γ-energy spectrum acquired on the ^{235}U sample. The (n,n') rays are shown in green, (n,2n) rays in red, radioactivity and identified fission product rays are in grey.

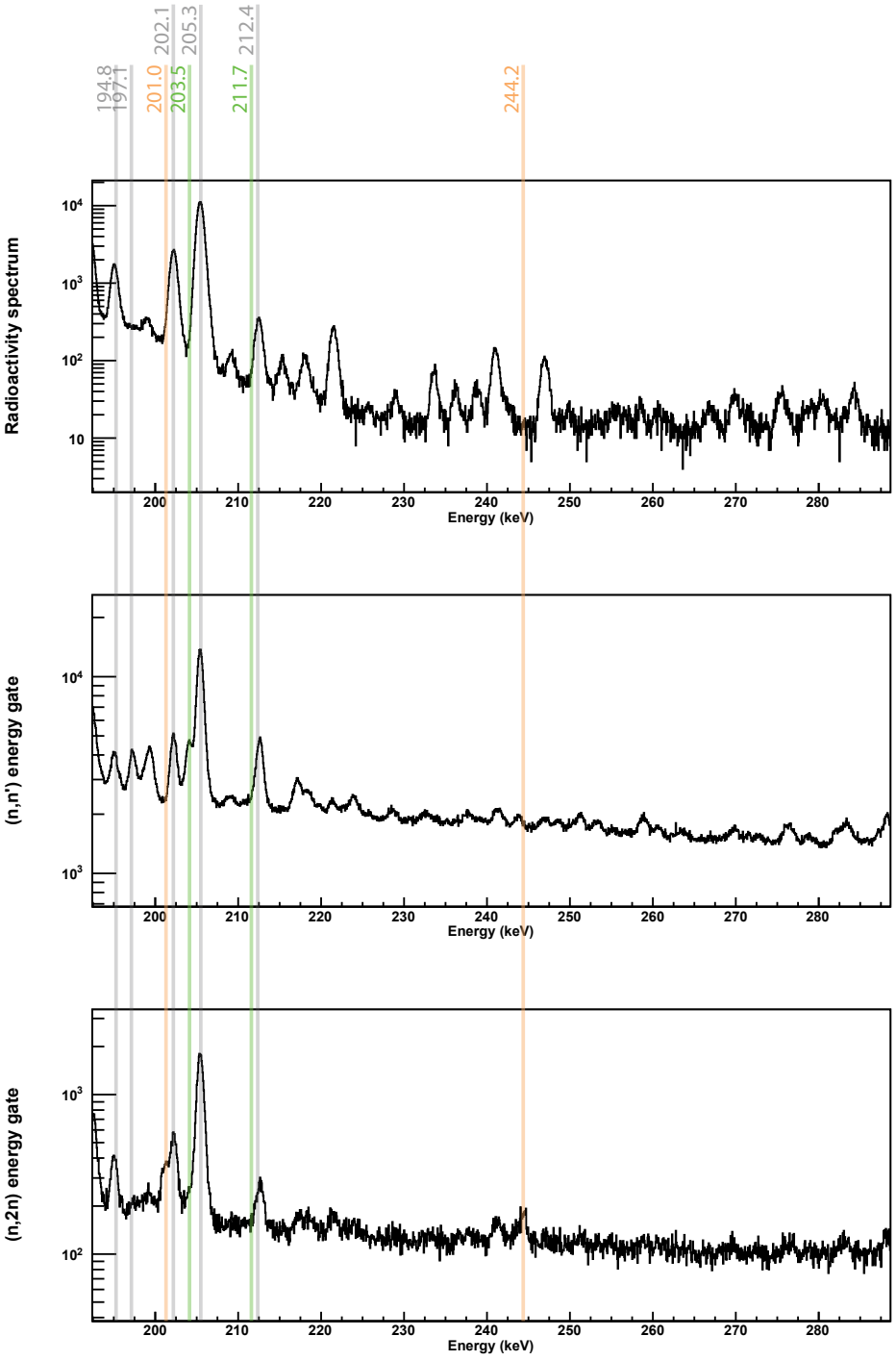

Figure B.2: Figure B.1 continued.

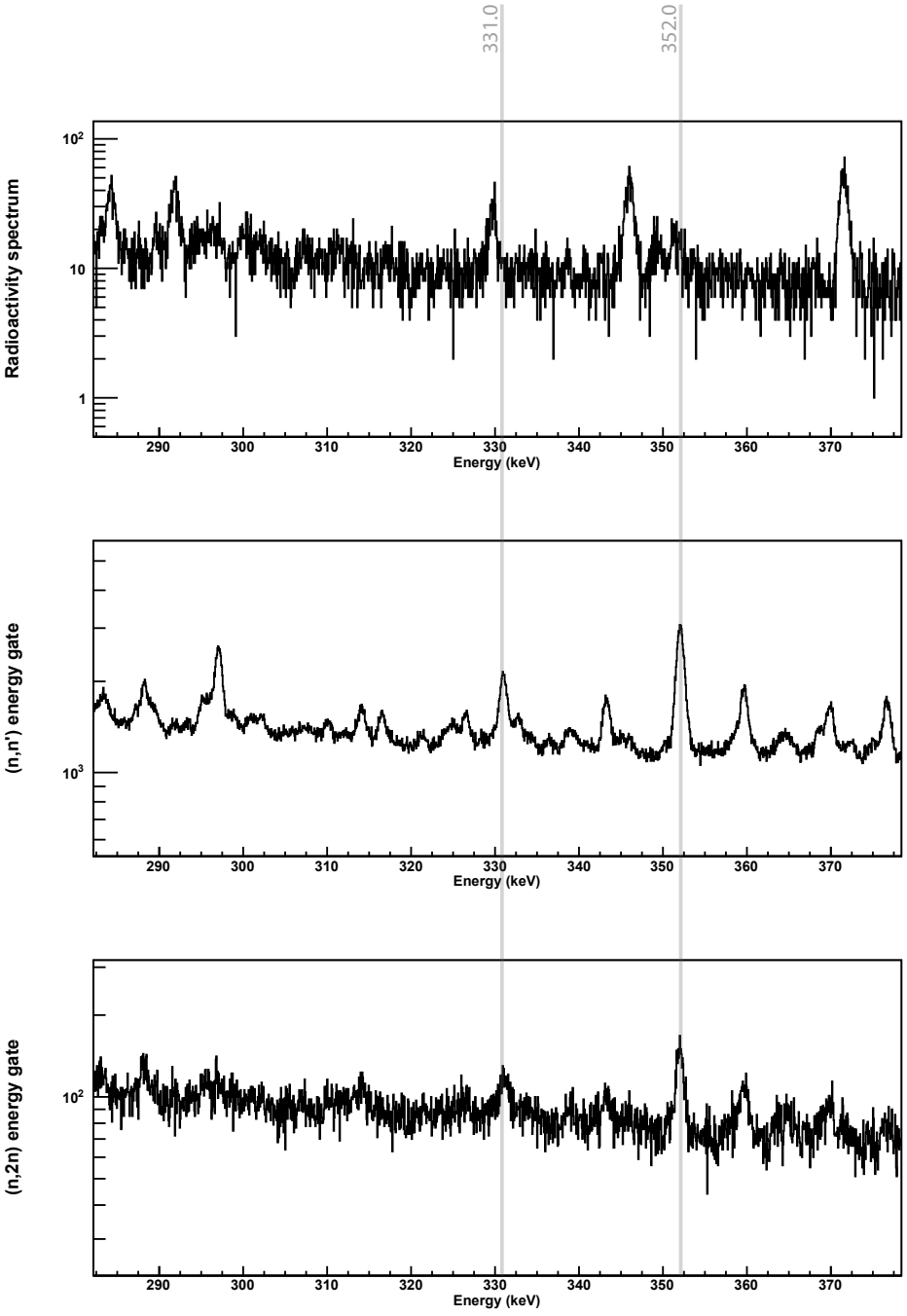

Figure B.3: Figure B.2 continued.

E_γ (keV)	Isotope	Initial state	Final state	reaction type
105.6	^{235}U	-	-	radioactivity
109.9	^{19}F	$1/2^-$ (E = 109.9)	$1/2^+$ (GS)	(n,γ)
111.3	U	$K_{\beta 1}$	-	X-ray
114.4	U	$K_{\beta 2}$	-	X-ray
119.7	^{235}U	$7/2^+$ (E = 171.4)	$5/2^+$ (E = 51.7)	(n,n'γ)
121.8	^{99}Zr	$3/2^+$ (E = 121.8)	$1/2^+$ (GS)	(n,f)
125.2	^{235}U	$7/2^+$ (E = 171.4)	$9/2^-$ (E = 46.2)	(n,n'γ)
129.3	^{235}U	$5/2^+$ (E = 129.3)	$7/2^-$ (GS)	(n,n'γ)
143.7	^{235}U	-	-	radioactivity
146.1	^{235}U	$15/2^-$ (E = 249.1)	$11/2^-$ (E = 103.0)	(n,n'γ)
151.8	^{102}Zr	2^+ (E = 151.8)	0^+ (GS)	(n,f)
152.7	^{234}U	6^+ (E = 296.1)	4^+ (E = 143.4)	(n,2nγ)
158.8	^{238}U	6^+ (E = 307.2)	4^+ (E = 148.4)	(n,n'γ)
160.2	^{235}U	$15/2^+$ (E = 357.3)	$13/2^+$ (E = 294.7)	(n,n'γ)
160.3	^{236}U	6^+ (E = 309.8)	4^+ (E = 149.5)	(n,γ)
162.4	^{99}Tc	$3/2^-$ (E = 671.5)	$3/2^-$ (E = 509.1)	(n,f)
163.3	^{235}U	-	-	radioactivity
167.8	^{235}U	$17/2^-$ (E = 338.5)	$13/2^-$ (E = 170.7)	(n,n'γ)
171.4	^{235}U	$7/2^+$ (E = 171.4)	$7/2^-$ (GS)	(n,n'γ)
171.6	^{145}La	$9/2^+$ (E = 237.9)	$7/2^+$ (E = 65.9)	(n,f)
185.7	^{231}Th	$5/2^-$ (E = 185.7)	$5/2^+$ (GS)	α-decay
197.1	^{19}F	$5/2^+$ (E = 197.1)	$1/2^+$ (GS)	(n,γ)
201.0	^{234}U	8^+ (E = 497.0)	6^+ (E = 296.0)	(n,2nγ)
202.1	^{235}U	-	-	radioactivity
203.5	^{235}U	$5/2^+$ (E = 332.8)	$5/2^+$ (E = 129.3)	(n,n'γ)
203.9	^{75}Ge	$5/2^-$ (E = 457.0)	$3/2^-$ (E = 253.1)	(n,n'γ)
205.3	^{235}U	-	-	radioactivity
211.7	^{235}U	$21/2^-$ (E = 550.4)	$17/2^-$ (E = 338.7)	(n,n'γ)
212.4	^{236}U	8^+ (E = 522.3)	6^+ (E = 309.8)	(n,γ)
244.2	^{234}U	10^+ (E = 741.2)	8^+ (E = 497.0)	(n,2nγ)
331.0	^{140}Cs	(E = 345.0)	(E = 14.0)	(n,f)

Table B.1: Identified γ energies of the ^{235}U energy spectra.

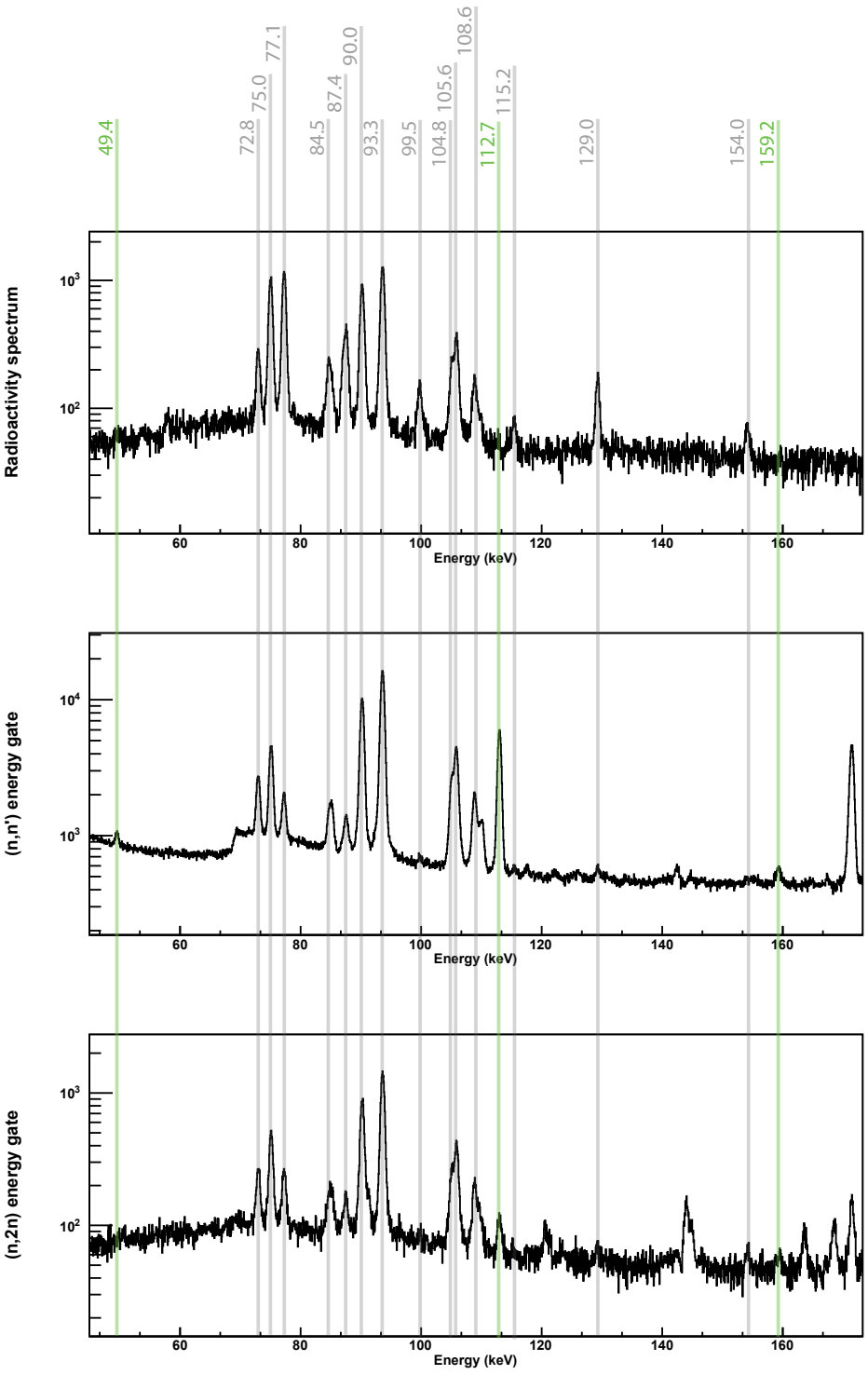

Figure B.4: Raw γ-energy spectrum acquired on the ^{232}Th sample. The (n,n') rays are shown in green, (n,2n) rays in red, (n,3n) in blue and radioactivity rays are in grey.

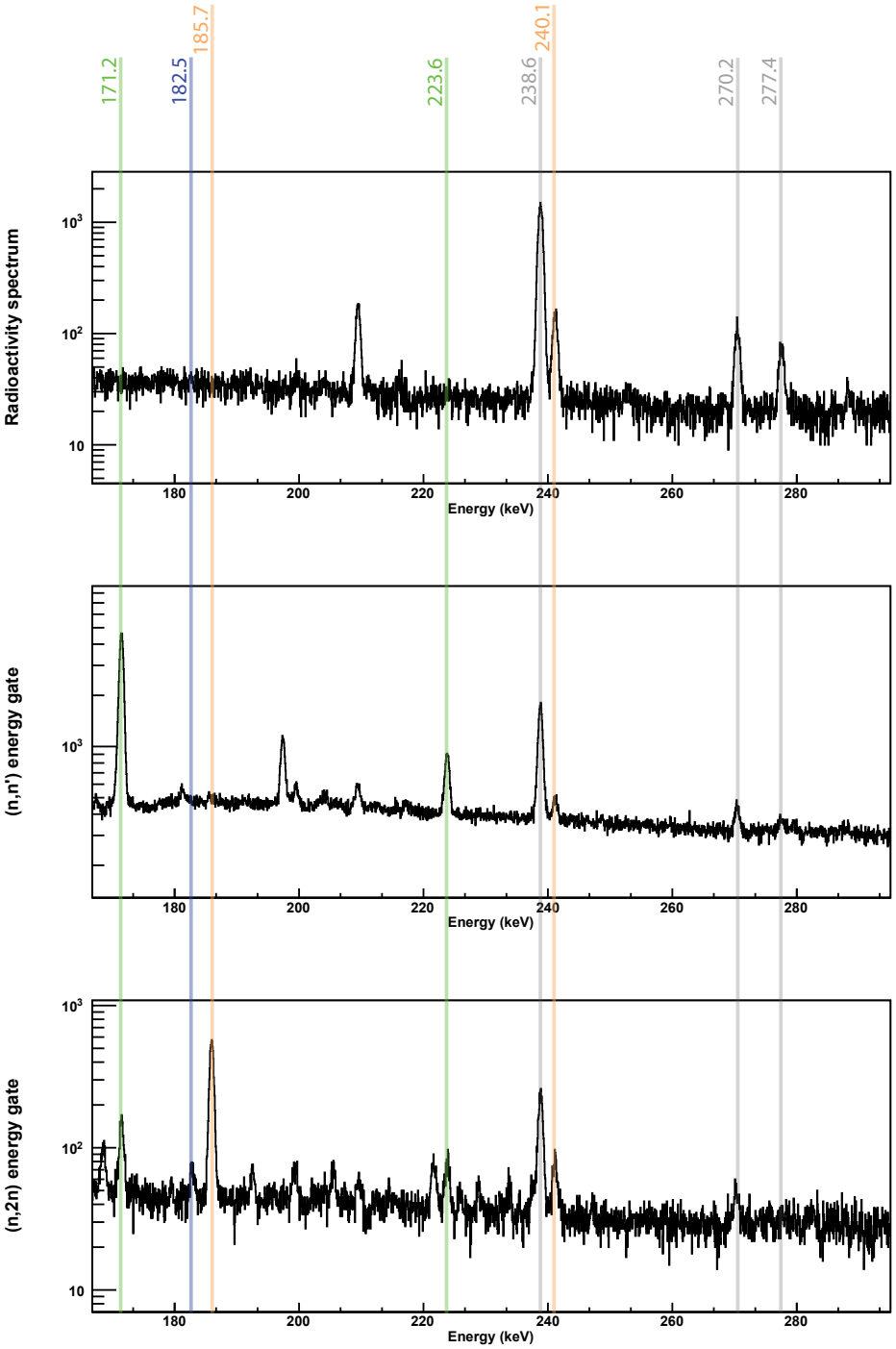

Figure B.5: Figure B.4 continued.

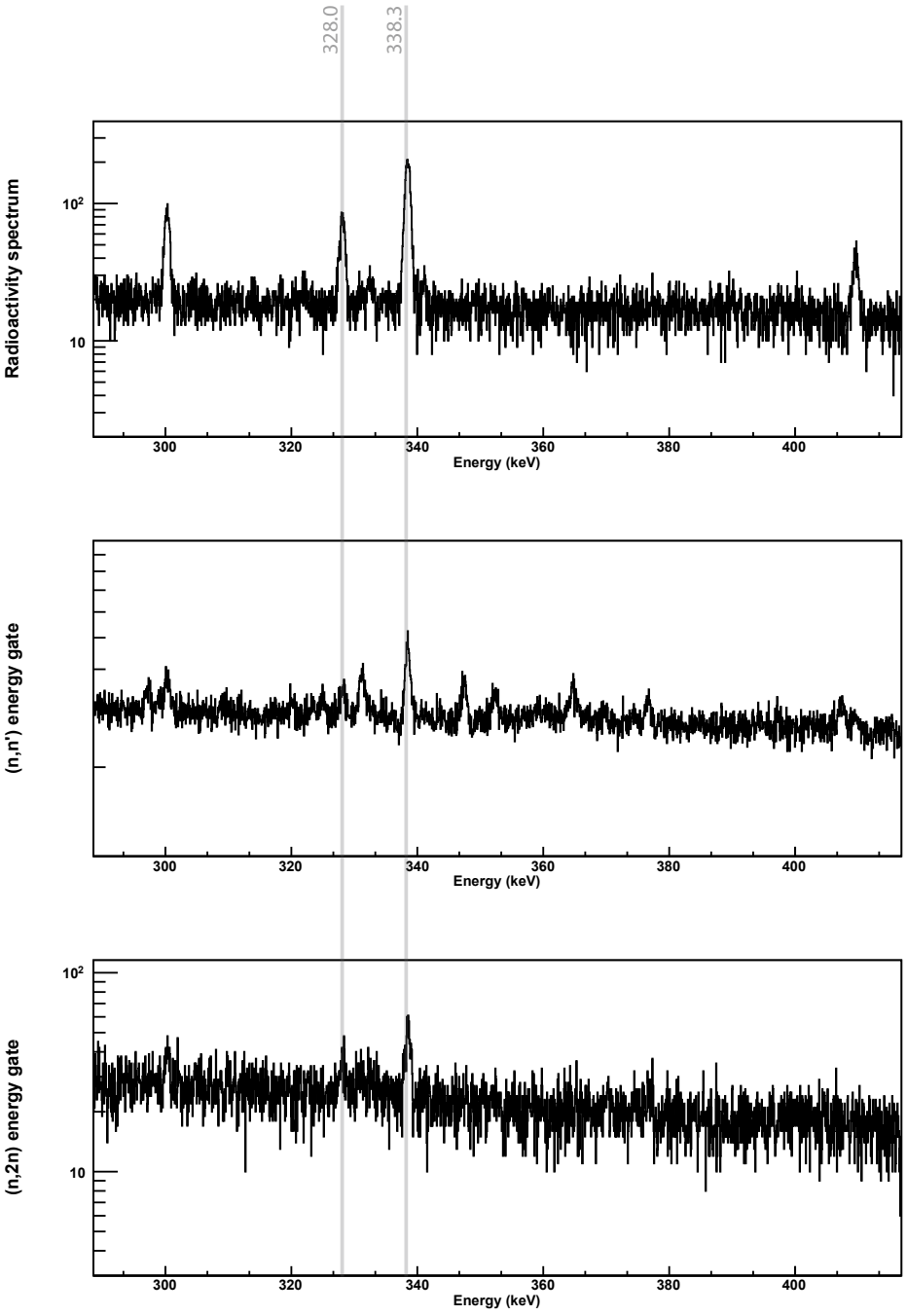

Figure B.6: Figure B.5 continued.

E_γ (keV)	Isotope	Initial state	Final state	reaction type
49.4	^{232}Th	2^+ (E = 49.4)	0^+ (GS)	(n,n'γ)
72.8	Pb	$K_{\alpha 2}$	-	X-ray
75.0	Pb	$K_{\alpha 1}$	-	X-ray
77.1	Bi	$K_{\alpha 1}$	-	X-ray
84.5	Pb	$K_{\beta 1}$	-	X-ray
87.4	Pb	$K_{\beta 2}$	-	X-ray
90.0	Th	$K_{\alpha 2}$	-	X-ray
93.3	Th	$K_{\alpha 1}$	-	X-ray
99.5	^{228}Th	-	-	radioactivity
104.8	Th	$K_{\beta 3}$	-	X-ray
105.6	Th	$K_{\beta 1}$	-	X-ray
108.6	Th	$K_{\beta 2}$	-	X-ray
112.7	^{232}Th	4^+ (E = 162.1)	2^+ (49.4)	(n,n'γ)
115.2	^{212}Bi	-	-	radioactivity
129.0	^{228}Th	-	-	radioactivity
154.0	^{228}Th	-	-	radioactivity
159.2	^{232}Th	7^- (E = 1042.9)	5^- (883.8)	(n,n'γ)
171.2	^{232}Th	6^+ (E = 333.3)	4^+ (162.1)	(n,n'γ)
182.5	^{230}Th	6^+ (E = 356.5)	4^+ (174.1)	(n,3nγ)
185.7	^{231}Th	$5/2^-$ (E = 185.7)	$5/2^+$ (GS)	(n,2nγ)
223.6	^{232}Th	8^+ (E = 556.9)	6^+ (333.3)	(n,n'γ)
238.6	^{212}Bi	-	-	radioactivity
240.1	^{231}Th	$5/2^+$ (E = 240.1)	$5/2^+$ (GS)	(n,2nγ)
270.2	^{228}Th	-	-	radioactivity
277.4	^{208}Pb	-	-	radioactivity
328.0	^{228}Th	-	-	radioactivity
338.3	^{228}Th	-	-	radioactivity

Table B.2: Identified γ energies of the ^{232}Th energy spectra.

Appendix C

Evaluated Data

In this appendix the different data points which have been measured in this work and discussed in chapter 5 are listed.

C.1 Data points measured on the ^{235}U isotope

C.1.1 Cross section of the 129.30 keV γ transition

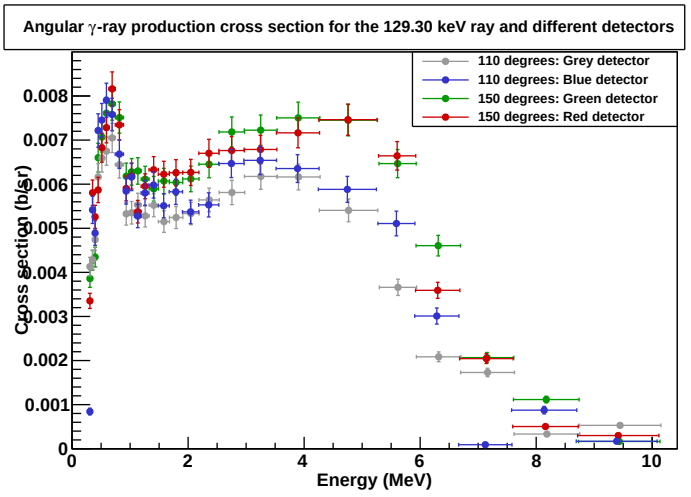

Figure C.1: Angular γ production cross section of the 129.30 keV transition from states $\frac{5}{2}^+ \rightarrow \frac{7}{2}^-$ due to a ^{235}U(n,n')^{235}U reaction obtained for the four different detectors.

E_n (MeV)	σ (mb)	ΔE_n (MeV)	$\Delta\sigma$ (mb)	$\frac{\Delta\sigma}{\sigma}$ (%)
9.423	5.58	0.701	0.66	11.8
8.167	8.06	0.565	0.68	8.5
7.146	22.71	0.462	1.45	6.4
6.306	41.13	0.382	2.35	5.7
5.607	69.53	0.320	3.81	5.4
4.757	88.97	0.502	4.66	5.2
3.896	95.38	0.372	4.99	5.2
3.249	94.44	0.282	4.93	5.2
2.751	91.27	0.220	4.76	5.2
2.359	86.19	0.174	4.49	5.2
2.046	81.66	0.141	4.26	5.2
1.791	81.92	0.115	4.27	5.2
1.581	80.36	0.095	4.19	5.2
1.406	84.38	0.080	4.40	5.2
1.258	81.51	0.067	4.26	5.2
1.133	81.21	0.058	4.25	5.2
1.025	83.81	0.049	4.40	5.2
0.932	81.97	0.043	4.33	5.2
0.815	98.80	0.071	5.12	5.1
0.690	108.31	0.055	5.62	5.1
0.592	104.15	0.043	5.44	5.2
0.513	99.68	0.035	5.28	5.2
0.449	92.61	0.029	4.99	5.3
0.396	70.09	0.024	3.90	5.5
0.352	68.94	0.020	3.87	5.6
0.307	50.09	0.024	2.90	5.8

Table C.1: Values measured for the 129.30 keV γ transition from states $\frac{5}{2}^+ \rightarrow \frac{7}{2}^-$ due to a ^{235}U(n,n')^{235}U reaction.

C.1.2 Cross section of the 152.72 keV γ transition

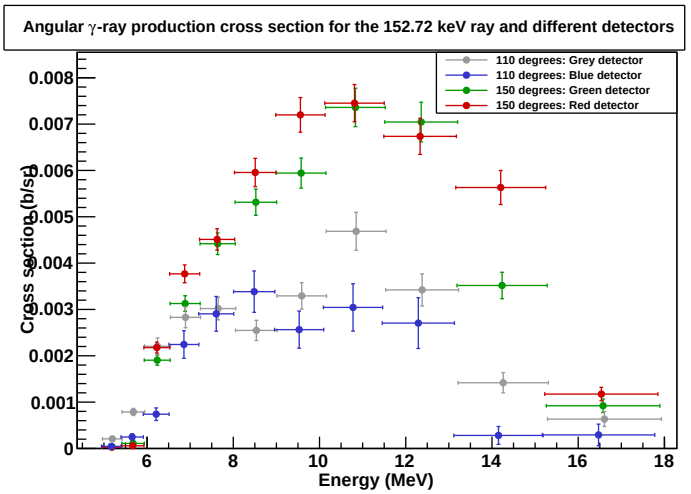

Figure C.2: Angular γ production cross section of the 152.72 keV transition from states $6^+ \rightarrow 4^+$ due to a ^{235}U(n,2n)^{234}U reaction obtained for the four different detectors.

E_n (MeV)	σ (mb)	ΔE_n (MeV)	$\Delta\sigma$ (mb)	$\frac{\Delta\sigma}{\sigma}$ (%)
23.392	9.86	2.223	2.80	28.4
19.528	6.54	1.689	1.62	24.7
16.556	9.37	1.314	1.71	18.3
14.218	30.42	1.043	3.33	10.9
12.346	57.98	0.843	4.17	7.1
10.822	69.23	0.690	4.41	6.3
9.565	56.08	0.573	3.49	6.2
8.516	48.92	0.481	2.94	6.0
7.631	45.50	0.407	2.66	5.8
6.877	38.55	0.348	2.26	5.8
6.231	24.81	0.300	1.54	6.2
5.671	5.95	0.260	0.72	12.2
5.184	1.55	0.227	0.29	18.9

Table C.2: Values measured for the 152.72 keV γ transition from states $6^+ \rightarrow 4^+$ due to a ^{235}U(n,2n)^{234}U reaction.

C.1.3 Cross section of the 200.97 keV γ transition

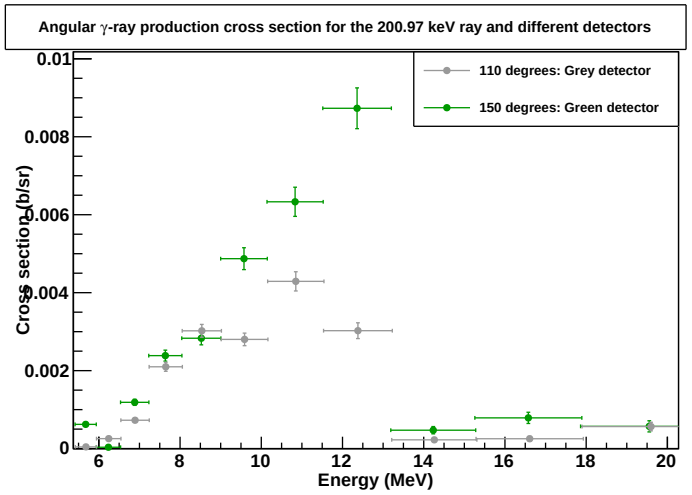

Figure C.3: Angular γ production cross section of the 200.97 keV transition from states $8^+ \rightarrow 6^+$ due to a ^{235}U(n,2n)^{234}U reaction obtained for the two different detectors.

E_n (MeV)	σ (mb)	ΔE_n (MeV)	$\Delta\sigma$ (mb)	$\frac{\Delta\sigma}{\sigma}$ (%)
19.528	7.13	1.689	2.21	31.1
16.556	5.52	1.314	1.63	29.5
14.218	3.90	1.043	1.12	28.7
12.346	62.95	0.843	4.41	7.0
10.822	62.83	0.690	3.78	6.0
9.565	44.25	0.573	2.61	5.9
8.516	37.13	0.481	2.17	5.8
7.631	27.62	0.407	1.61	5.8
6.877	11.15	0.348	0.82	7.3
6.231	2.25	0.300	0.61	27.4
5.671	3.08	0.260	0.57	18.5

Table C.3: Values measured for the 200.97 keV γ transition from states $8^+ \rightarrow 6^+$ due to a ^{235}U(n,2n)^{234}U reaction.

C.1.4 Cross section of the 244.2 keV γ transition

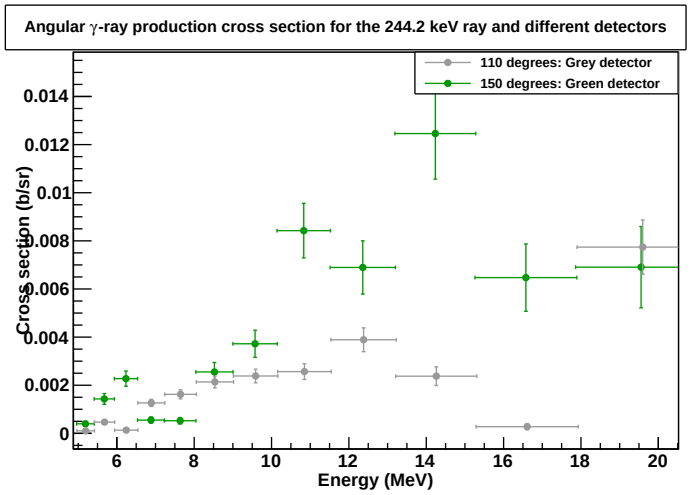

Figure C.4: Angular γ production cross section of the 244.2 keV transition from states $10^+ \rightarrow 8^+$ due to a ^{235}U(n,2n)^{234}U reaction obtained for the two different detectors.

E_n (MeV)	σ (mb)	ΔE_n (MeV)	$\Delta\sigma$ (mb)	$\frac{\Delta\sigma}{\sigma}$ (%)
16.556	16.41	1.314	6.19	37.7
14.218	46.71	1.043	6.73	14.4
12.346	46.94	0.843	6.03	12.8
10.822	39.44	0.690	4.36	11.0
9.565	27.67	0.573	3.25	11.7
8.516	23.08	0.481	2.71	11.7
7.631	14.43	0.407	2.80	19.4
6.877	11.58	0.348	2.05	17.7
6.231	6.06	0.300	1.10	18.1
5.671	6.95	0.260	0.94	13.5

Table C.4: Values measured for the 244.2 keV γ transition from states $10^+ \rightarrow 8^+$ due to a ^{235}U(n,2n)^{234}U reaction.

C.2 Data points measured on the ^{232}Th isotope

C.2.1 Cross section of the 112.75 keV γ transition

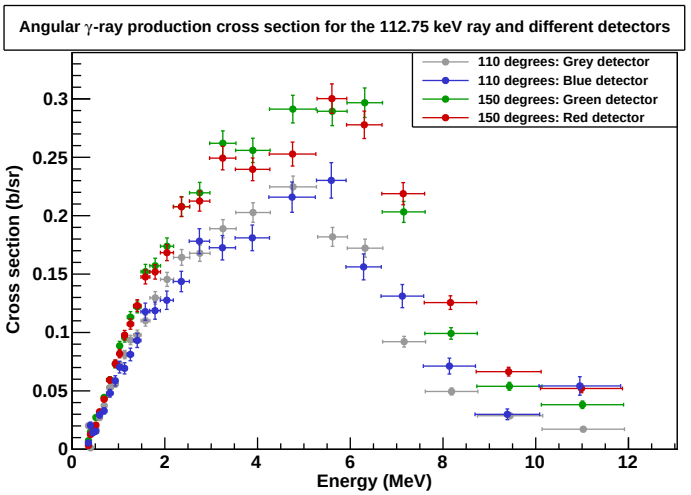

Figure C.5: Angular γ production cross section of the 112.75 keV transition from states $4^+ \rightarrow 2^+$ due to a ^{232}Th(n,n')^{232}Th reaction obtained for the four different detectors.

C.2.2 Cross section of the 171.2 keV γ transition

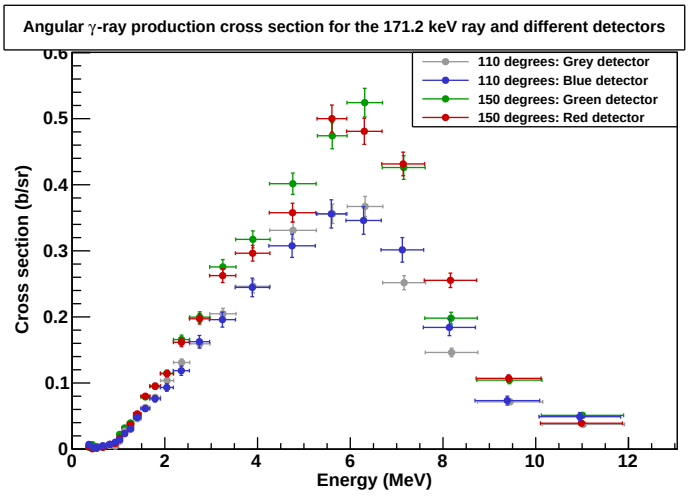

Figure C.6: Angular γ production cross section of the 171.2 keV transition from states $6^+ \rightarrow 4^+$ due to a ^{232}Th(n,n')^{232}Th reaction obtained for the four different detectors.

E_n (MeV)	σ (mb)	ΔE_n (MeV)	$\Delta\sigma$ (mb)	$\frac{\Delta\sigma}{\sigma}$ (%)
10.996	32.5	0.885	3.3	10.4
9.423	38.1	0.701	3.2	8.4
8.167	72.3	0.565	4.8	6.6
7.146	134.4	0.462	8.0	5.9
6.306	197.4	0.382	11.1	5.6
5.607	217.6	0.320	12.2	5.6
4.757	223.8	0.502	12.0	5.3
3.896	200.6	0.372	10.7	5.3
3.249	196.3	0.282	10.5	5.3
2.751	175.0	0.220	9.4	5.3
2.359	164.7	0.174	8.8	5.3
2.046	141.4	0.141	7.6	5.3
1.791	127.6	0.115	6.9	5.4
1.581	117.8	0.095	6.4	5.4
1.406	99.1	0.080	5.4	5.4
1.258	90.7	0.067	5.0	5.5
1.133	79.0	0.058	4.4	5.5
1.025	71.3	0.049	4.0	5.6
0.932	58.6	0.043	3.4	5.8
0.815	50.7	0.071	2.8	5.6
0.690	36.2	0.055	2.1	5.8
0.592	27.2	0.043	1.7	6.2
0.513	18.0	0.035	1.3	7.2
0.449	14.7	0.029	1.2	8.4
0.396	8.8	0.024	1.0	11.8
0.352	11.0	0.020	1.2	11.6

Table C.5: Values measured for the 112.75 keV γ transition from states $4^+ \rightarrow 2^+$ due to a ^{232}Th(n,n')^{232}Th reaction.

E_n (MeV)	σ (mb)	ΔE_n (MeV)	$\Delta\sigma$ (mb)	$\frac{\Delta\sigma}{\sigma}$ (%)
10.996	39.3	0.885	3.2	8.3
9.423	79.4	0.701	5.0	6.4
8.167	173.1	0.565	9.8	5.6
7.146	306.3	0.462	16.8	5.4
6.306	387.4	0.382	21.0	5.4
5.607	380.9	0.320	20.6	5.4
4.757	322.9	0.502	17.1	5.3
3.896	251.6	0.372	13.4	5.3
3.249	213.0	0.282	11.3	5.3
2.751	163.7	0.220	8.7	5.3
2.359	132.4	0.174	7.1	5.3
2.046	99.4	0.141	5.3	5.4
1.791	79.0	0.115	4.3	5.4
1.581	64.6	0.095	3.5	5.4
1.406	45.7	0.080	2.5	5.6
1.258	32.2	0.067	1.8	5.7
1.133	24.8	0.058	1.4	5.9
1.025	13.9	0.049	0.9	6.6
0.932	6.2	0.043	0.5	8.1
0.815	5.9	0.071	0.4	7.1
0.663	3.1	0.078	0.2	8.0
0.531	1.8	0.056	0.2	11.1
0.435	2.6	0.041	0.3	12.1
0.363	4.5	0.031	0.5	11.1

Table C.6: Values measured for the 171.2 keV γ transition from states $6^+ \rightarrow 4^+$ due to a ^{232}Th(n,n')^{232}Th reaction.

C.2.3 Cross section of the 223.6 keV γ transition

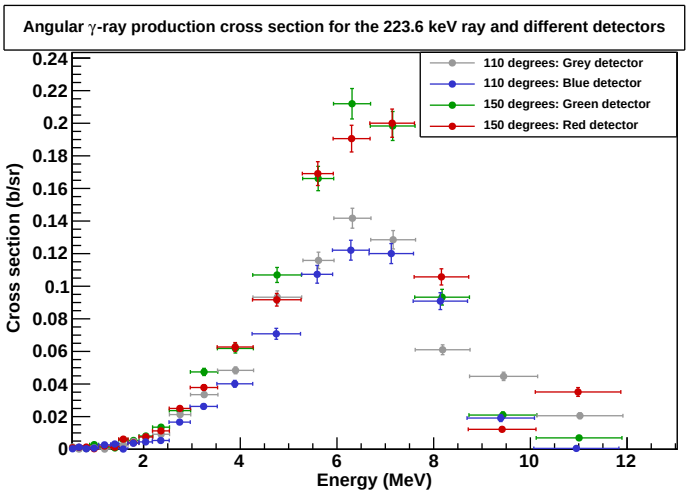

Figure C.7: Angular γ production cross section of the 223.6 keV transition from states $8^+ \rightarrow 6^+$ due to a ^{232}Th(n,n')^{232}Th reaction obtained for the four different detectors.

C.2.4 Cross section of the 49.37 keV γ transition

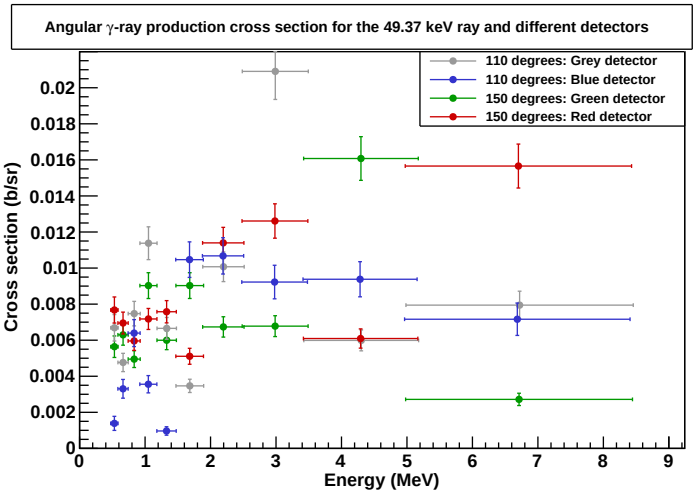

Figure C.8: Angular γ production cross section of the 49.37 keV transition from states $2^+ \rightarrow 0^+$ due to a ^{232}Th(n,n')^{232}Th reaction obtained for the four different detectors.

E_n (MeV)	σ (mb)	ΔE_n (MeV)	$\Delta\sigma$ (mb)	$\frac{\Delta\sigma}{\sigma}$ (%)
10.996	18.84	0.885	2.12	11.2
9.423	31.51	0.701	2.78	8.8
8.167	82.11	0.565	5.09	6.2
7.146	155.97	0.462	8.89	5.7
6.306	162.92	0.382	9.19	5.6
5.607	136.41	0.320	7.76	5.6
4.757	94.11	0.502	5.20	5.5
3.896	53.46	0.372	3.04	5.6
3.249	36.18	0.282	2.10	5.8
2.751	22.29	0.220	1.36	6.1
2.359	9.86	0.174	0.68	6.9
2.046	7.30	0.141	0.53	7.3
1.791	4.61	0.115	0.38	8.3
1.581	3.45	0.095	0.33	9.5
1.406	2.11	0.080	0.27	12.9
1.193	1.08	0.126	0.13	12.3
0.977	1.00	0.093	0.12	12.6
0.815	0.57	0.071	0.10	18.1
0.663	0.58	0.078	0.09	16.8

Table C.7: Values measured for the 223.6 keV γ transition from states $8^+ \rightarrow 6^+$ due to a ^{232}Th(n,n')^{232}Th reaction.

E_n (MeV)	σ (mb)	ΔE_n (MeV)	$\Delta\sigma$ (mb)	$\frac{\Delta\sigma}{\sigma}$ (%)
6.707	8.45	1.730	1.99	23.5
4.294	8.54	0.874	1.91	22.3
2.984	14.82	0.503	3.03	20.4
2.194	10.08	0.315	2.11	21.0
1.681	6.31	0.211	1.43	22.7
1.329	5.56	0.148	1.29	23.1
1.051	8.69	0.130	1.84	21.2
0.833	6.67	0.091	1.53	22.9
0.663	5.17	0.078	1.28	24.8
0.531	5.63	0.056	1.51	26.9

Table C.8: Values measured for the 49.37 keV γ transition from states $2^+ \rightarrow 0^+$ due to a ^{232}Th(n,n')^{232}Th reaction.

C.2.5 Cross section of the 185.7 keV γ transition

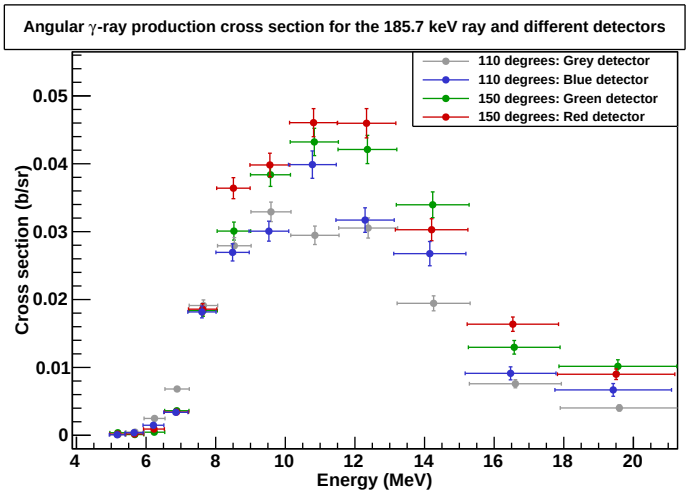

Figure C.9: Angular γ production cross section of the 185.7 keV transition from states $\frac{5}{2}^- \rightarrow \frac{5}{2}^+$ due to a ^{232}Th(n,2n)^{231}Th reaction obtained for the four different detectors.

E_n (MeV)	σ (mb)	ΔE_n (MeV)	$\Delta\sigma$ (mb)	$\frac{\Delta\sigma}{\sigma}$ (%)
19.528	82.19	1.689	9.41	11.4
16.556	133.79	1.314	11.65	8.7
14.218	322.29	1.043	21.83	6.7
12.346	457.12	0.843	27.75	6.0
10.822	472.71	0.690	27.62	5.8
9.565	447.01	0.573	25.29	5.6
8.516	384.76	0.481	21.50	5.5
7.631	242.63	0.407	13.67	5.6
6.877	65.98	0.348	4.19	6.3
6.231	22.24	0.300	1.92	8.6
5.671	4.60	0.260	0.69	14.9
5.184	2.02	0.227	0.37	18.5

Table C.9: Values measured for the 185.7 keV γ transition from states $\frac{5}{2}^- \rightarrow \frac{5}{2}^+$ due to a ^{232}Th(n,2n)^{231}Th reaction.

C.2.6 Cross section of the 182.5 keV γ transition

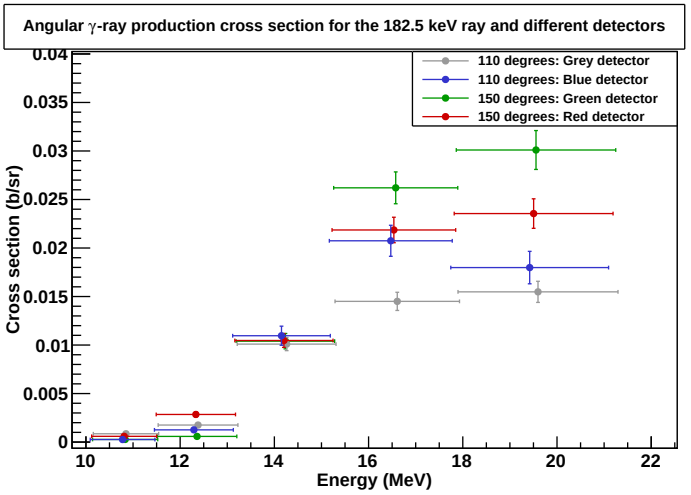

Figure C.10: Angular γ production cross section of the 182.5 keV transition from states $6^+ \rightarrow 4^+$ due to a ^{232}Th(n,3n)^{230}Th reaction obtained for the four different detectors.

E_n (MeV)	σ (mb)	ΔE_n (MeV)	$\Delta\sigma$ (mb)	$\frac{\Delta\sigma}{\sigma}$ (%)
19.528	253.42	1.689	20.34	8.0
16.556	241.66	1.314	18.06	7.4
14.218	133.92	1.043	10.86	8.1
12.346	22.16	0.843	2.86	12.9
10.822	7.94	0.690	1.39	17.5

Table C.10: Values measured for the 182.5 keV γ transition from states $6^+ \rightarrow 4^+$ due to a ^{232}Th(n,3n)^{230}Th reaction.

Abstract

The design of Generation IV nuclear reactors and the research of new fuel cycles require knowledge of the cross sections of different nuclear reactions. The research in this work is focused on cross section measurements of (n,xnγ) reactions occurring in these new reactors. The aim is to measure unknown cross sections and to reduce the uncertainty on current data relative to reactions and isotopes present in transmutation or regeneration processes.

The presented work consists of studying ^{232}Th(n,xnγ) and ^{235}U(n,xnγ) reactions in the fast neutron energy domain (up to 20 MeV) with the best precision possible. The experiments are performed at GELINA which delivers a pulsed, white neutron beam at IRMM, Belgium. The time characteristics of the beam enable us to measure neutron energies with the time-of-flight (TOF) technique. The neutron induced reactions (in this case inelastic scattering, (n,2n) and (n,3n) reactions) are identified by online prompt γ spectroscopy with an experimental setup including four HPGe detectors. A double layered fission chamber is used to monitor the incident neutron flux. The obtained results are presented and a comparison between the measured cross sections and the TALYS code predictions will be discussed.

In order to achieve a very high precision on the reaction cross sections, an extensive work has been realised on the detection efficiencies of the counters used in the experiment. These quantities were in fact the largest sources of uncertainty in foregoing campaigns. After important efforts including high precision measurements together with Geant4 simulations, the efficiency of the fission chambers as well as of the HPGe detectors could be determined with accuracies below 3 %, accomplishing the final goal of a cross section determination with a precision of 5 %.

This work is a further step in the preparation of the measurement of ^{233}U(n,xnγ) reactions, which are completely unknown at this stage although of very high importance in the ^{232}Th regeneration process. For this reason, a new, segmented HPGe detector was conceived, which will complete the current experimental setup.